

The water-oxidizing manganese complex
of oxygenic photosynthesis:
Structural models based on
X-ray absorption spectroscopy

Freie Universität



Berlin

Am Fachbereich Physik der Freien Universität Berlin
vorgelegte Dissertation von Alexander Peter Grundmeier
Berlin 2012

The water-oxidizing manganese complex of oxygenic photosynthesis:
Structural models based on X-ray absorption spectroscopy

Alexander P. Grundmeier

The water-oxidizing manganese complex
of oxygenic photosynthesis:

Structural models based on
X-ray absorption spectroscopy

Inauguraldissertation

zur Erlangung des Grades eines
Doktors der Naturwissenschaften

am Fachbereich Physik
der Freien Universität Berlin

vorgelegt von

Alexander Peter Grundmeier

Berlin 2012

Erstgutachter: Prof. Dr. Holger Dau

Zweitgutachter: Prof. Dr. Wolfgang Kuch

Tag der Disputation: 28.11.2011

Contents

Subject and goals	1
1. Introduction	3
1.1. Photosystem II and the manganese complex	3
1.1.1. Photosynthesis	3
1.1.2. Photosystem II	4
1.1.3. The manganese complex of PSII	5
1.2. X-ray absorption spectroscopy	6
1.2.1. Introduction	7
1.2.2. The EXAFS region of XAS spectra	8
1.2.3. XAS measurements and EXAFS data evaluation	11
1.2.4. Linear dichroism effect	14
2. Structural models of the Mn complex – Present status	17
2.1. Early models based on EXAFS and EPR results	18
2.2. Protein crystallography and OEC structure	19
2.3. Radiation damage	23
2.4. Combining XAS and XRD data	25
2.4.1. Models of Yano and coworkers	25
2.4.2. Models of Sproviero and coworkers	28
2.4.3. Model of Dau and coworkers	31
2.4.4. Conclusions	31
3. Improved distance resolution by extended-range EXAFS	33
3.1. Preparation of samples	33
3.1.1. Preparation of PSII membrane particles	33
3.1.2. Preparation of partially oriented samples	33
3.2. Experimental setup and data collection	34
3.3. Extended-range EXAFS and data evaluation	34
3.4. Results	37
3.5. Summary	39
4. Modeling the Mn complex	41
4.1. Experimental data used for model evaluation	41

Contents

4.2. Calculation of EXAFS spectra	42
4.3. Considered models of the OEC	45
4.4. Optimization of structural models	45
5. Evaluation of OEC models	51
5.1. Calculation and evaluation of spectra	51
5.2. Models A-I, A-II, A-IIa, and A-III	53
5.3. Models B-I and B-II	53
5.4. Models E-A and E-B	57
5.5. Models C-I, C-II, C-III, C-IV, D, and F	58
5.6. Influence of ligating amino acids on EXAFS	62
5.7. Summary and conclusions	65
6. Implications and future directions	69
6.1. Mechanistic implications	69
6.2. Future perspectives and outlook	72
References	75
A. Appendix	91
A.1. Average angle to unit cell axes for PSII crystal	91
A.2. Calculation of amplitude and phase functions using FEFF	92
A.2.1. General principle	92
A.2.2. Actual procedure	93
A.2.3. Phase/amplitude functions used	93
A.3. Formal oxidation states derived from Mn-O bond lengths	96
A.4. Program for calculation of EXAFS spectra	97
A.4.1. Description of features	98
A.4.2. Format of restraints	101
A.4.3. List of used libraries	104
A.5. Used molecular visualization programs	105
B. Atom coordinates of models	107
B.1. Model C-I	107
B.2. Model C-II	109
B.3. Model C-III	111
B.4. Model C-IV	113
B.5. Model D	115
B.6. Model F	117

Authored and co-authored publications	121
Peer-reviewed articles	121
Other articles	122
Abstract	123
Kurzfassung	125
Danksagung	127

Subject and goals

The oxygen of the atmosphere stems mostly from photosynthesis, which occurs in cyanobacteria, algae, and higher plants. Essential for this process is a protein complex named photosystem II (PSII). In the oxygen-evolving complex (OEC) of PSII, the energy of sunlight is used to oxidize water to molecular oxygen and generate protons. This OEC is a protein-cofactor complex with an inorganic core consisting of a cluster of four Mn atoms and one Ca atom and is therefore often called Mn_4CaO_5 complex, Mn_4Ca complex, or simply manganese (Mn) complex. The Mn atoms are connected by mono- μ -oxo, di- μ -oxo, and/or hydroxo bridges.

Definitive structural models of the manganese complex are essential for gaining a full understanding of the mechanism of photosynthetic water oxidation. Therefore, several experimental methods have been used to investigate this complex and resolve its structure and function: Electron paramagnetic resonance (EPR) and electron nuclear double-resonance (ENDOR) spectroscopy, Fourier transform infrared (FTIR) spectroscopy, fluorescence measurements, time-resolved mass spectrometry (MS), X-ray diffraction (XRD), and X-ray absorption spectroscopy (XAS), especially EXAFS (extended X-ray absorption fine structure). Despite these intensive efforts, the exact configuration of the OEC is yet not clear.

The scientific goals of this thesis have been:

- To use EXAFS up to an especially high energy range (“extended-range” EXAFS) for obtaining more definitive structural information (published in Dau et al. [2008] and Grundmeier et al. [2008a]).
- To calculate EXAFS spectra (for partially oriented as well as crystallized samples) for models of the manganese complex currently proposed in literature and compare these simulations to experimental results (published in Grundmeier and Dau [2012]).
- To develop new models for the manganese complex based on EXAFS and XRD results (published in Grundmeier and Dau [2012]).

The thesis is structured as follows:

In the first chapter, an introduction is given. Photosynthesis, photosystem II, and its manganese complex are described. Furthermore, the most important method for this thesis is presented: X-ray absorption spectroscopy. Especially, the linear dichroism effect will be explained.

Subject and goals

The second chapter concentrates on the present state of research regarding the structure of the manganese complex, but also gives a brief summary of the developments in last decade. Three recent models of the Mn complex [Yano et al., 2006; Sproviero et al., 2008b; Dau et al., 2008] will be discussed.

In the third chapter, the extended-range EXAFS method is explained and spectra measured for photosystem II are presented and discussed.

Chapter four describes, how the EXAFS spectra shown in this thesis were calculated and how the new models of the Mn complex were designed.

In the subsequent fifth chapter, EXAFS spectra are calculated for recently in literature published models of the Mn complex and new models are developed. The models are discussed in respect to experimental EXAFS spectra as well as XRD data.

Chapter six deals with the mechanistic implications of the results for the water oxidation process and discusses potential future developments on this field.

In addition to these works on the manganese complex, the author of this thesis was involved in other projects and XAS measurements at the synchrotron radiation sources DESY, BESSY, and ESRF, which will not be discussed in this thesis:

- Measurement of EXAFS spectra on vanadium-bromine complexes modeling a vanadium bromoperoxidase [Grundmeier et al., 2008b].
- Analysis of the binding of Zn and Cu ions to peptides (important for amyloid formation in Alzheimer's disease) using XANES spectra [Grundmeier et al., 2008b].
- Observations of the redox reactions of the Mn complex in the S-cycle under high O₂ partial pressure by rapid-scan and time-resolved XANES measurements [Haumann et al., 2008].
- EXAFS measurements on Mn model compounds mimicking the Mn complex [Grundmeier et al., 2006].
- Several other XAS measurements at various metal edges [Haumann et al., 2006; Barra et al., 2006; Grundmeier et al., 2008b; Risch et al., 2008; Sanganas et al., 2008; Voevodskaya et al., 2009].

1. Introduction

1.1. Photosystem II and the manganese complex

Plants, algae, and cyanobacteria use sunlight to convert carbon dioxide and water into carbohydrate and oxygen. This process is known as (*oxygenic*) *photosynthesis*. Photosynthesis is one of the key reactions in nature due to the fact that most of the biomass as well as oxygen in the atmosphere were generated by this process. It is also of special interest as a model for future technological systems or biomimetic compounds for the production of ‘solar fuels’ [Gust and Moore, 1989; Sun et al., 2000; Lewis and Nocera, 2006; Herrero et al., 2008; Lubitz et al., 2008; Rutherford and Moore, 2008; Hammarström and Hammes-Schiffer, 2009].

The protein complex photosystem II (PSII), including the oxygen evolving complex (OEC), is a crucial part of the complicated chain of reactions and compounds which are involved in this process [Blankenship, 2002]. In the following sections, an introduction to these important systems is given.

1.1.1. Photosynthesis

Oxygenic photosynthesis takes place in higher plants, green algae, and cyanobacteria. Water and carbon dioxide are used to produce carbohydrate and molecular oxygen. For this process, energy is absorbed in form of light using pigment molecules (mostly chlorophylls and carotenoids).

The photosynthetic process is divided in light-dependent reactions, which utilize light and store the energy in form of ATP and NADPH, and light-independent reactions like the *Calvin cycle* where organic compounds are produced. In the following, we will focus on the light-dependent reactions (see Fig. 1.1).

The light-dependent reactions of photosynthesis take place in the membrane of *thylakoids*, compartments inside chloroplasts (organelles within plants and green algae) and cyanobacteria [Ort and Yocum, 1996; Blankenship, 2002]. The thylakoid membrane consists mainly of lipids and proteins. *Light-harvesting protein complexes* (Lhc) with 200 to 300 pigment molecules located within the thylakoid membrane collect photons. The energy of the photons is transported by resonance energy transfer to two other protein complexes inside the membrane connected to such light-harvesting complexes: *photosystem I* (PSI) and *photosystem II* (PSII; see further below). These two complexes use this energy to generate an electrochemical potential across the thy-

1. Introduction

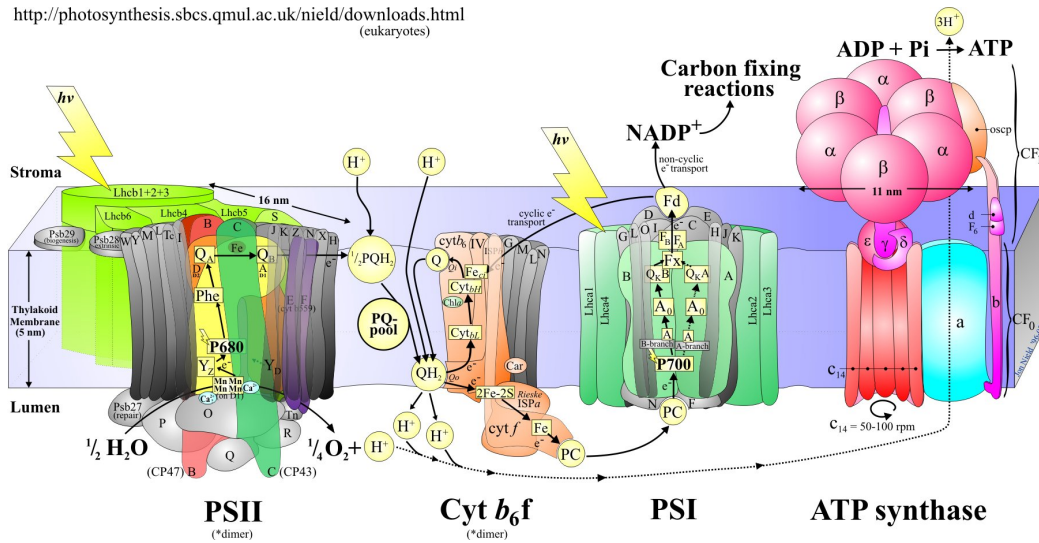


Figure 1.1.:

Schematic model of the in the photosynthetic light-dependent reactions involved compounds. Photosystem II (PSII) is the first structure in the electron transport chain after photons have been absorbed by the light-harvesting complexes (Lhc). For detailed explanations, see <http://www.photosynthesis.sbcs.qmul.ac.uk/nield/downloads.html>. Figure also from this website.

lakoid membrane, which is used to generate NADPH and, with help of an additional enzyme, ATP (Fig. 1.1). In this process, PSII uses water as an electron donor and molecular oxygen and protons are released.

1.1.2. Photosystem II

Photosystem II (PSII) is a dimeric protein complex located in the thylakoid membrane of plants, green algae, and cyanobacteria (Fig. 1.2). It is the only known protein complex that can oxidize water. A PSII monomer consists of 20 subunits (17 transmembrane subunits, three peripheral proteins, plus several cofactors) and has a total molecular weight of roughly 350 kDa. It contains 35 chlorophylls, two pheophytins, 11 β -carotenes, two plastoquinones (Q_A , Q_B), two haem irons and one non-haem iron, three Cl^- ions, one bicarbonate ion, more than 15 detergents and 20 lipids, and four Mn atoms and three to four Ca atoms [Umena et al., 2011]. All four Mn atoms and one Ca belong to the so called *manganese complex* where the oxidation of water takes place.

As mentioned above, photons are absorbed using an antenna system containing several hundred chlorophylls and carotinoids (light-harvesting complex). The energy is transferred to a special chlorophyll dimer called P680 within PSII where a charge separation between P680 and a pheophytin (Pheo) occurs. An electron moves from

1.1. Photosystem II and the manganese complex

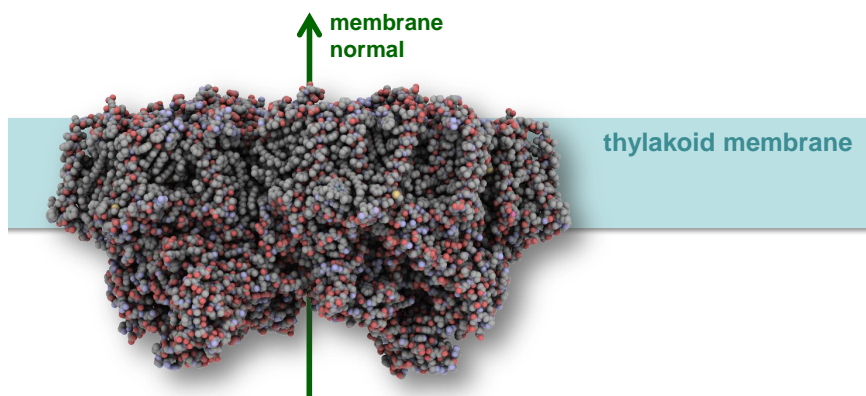


Figure 1.2.:

A photosystem II dimer embedded in a thylakoid membrane. The sketch of PSII is based on the XRD data 2AXT from Loll et al. [2005].

P680 to the pheophytin creating a $P680^+/Pheo^-$ pair. From there, the electron is transferred to the plastoquinone Q_A , a one-electron acceptor within the D_2 subunit of PSII. After this, a mobile plastoquinone Q_B (two-electron acceptor) located in the D_1 subunit is reduced by two electrons and two protons to a plastohydroquinone. For this process, the protons are taken from the outside of the thylakoid membrane. The plastohydroquinone then delivers the electrons to the next link in the electron-chain outside PSII (Fig. 1.1).

The now positive electron donor $P680^+$ is a powerful oxidizing agent. It oxidizes a tyrosine (Tyr_Z) in a distance of approximately 14 \AA , which is then reduced by the manganese complex (Mn complex), a Mn_4CaO_5 cluster (see following Section 1.1.3). The Mn complex catalyzes the oxidation of water and generates molecular oxygen during this process.

To examine the structure of PSII, X-ray crystallography was used (for an example, see Fig. 1.2). The first XRD structure with a resolution of 3.8 \AA was published in 2001 [Zouni et al., 2001]. In the following years, the resolution was continuously further improved [Kamiya and Shen, 2003; Ferreira et al., 2004; Biesiadka et al., 2004; Loll et al., 2005; Guskov et al., 2009]. In fall of 2010 at an international photosynthesis congress in Beijing, China, Shen presented new crystallographic data of PSII with a resolution of 1.9 \AA [Umena et al., 2011]. The extraordinary high resolution is an astonishing achievement (compare Fig. 1.3) and this breakthrough in the field of X-ray crystallography of PSII may further accelerate the understanding of the light-dependent reactions of photosynthesis.

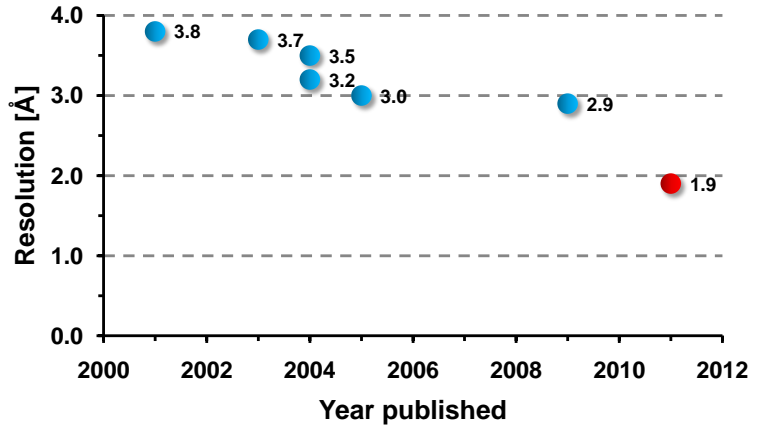
1.1.3. The manganese complex of PSII

The catalytic site of PSII water oxidation is commonly referred to as the *manganese complex* (Mn complex) or *oxygen-evolving complex* (OEC) [Debus, 1992; Yachandra et al., 1996; McEvoy and Brudvig, 2006]. Today it is known that the Mn complex contains four Mn ions and one Ca ion, which are connected via five oxygens, forming mono- μ -oxo, di- μ -oxo, and/or hydroxo bridges [Umena et al., 2011]. This Mn_4CaO_5

1. Introduction

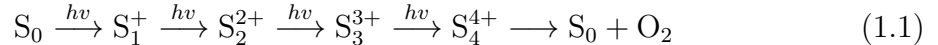
Figure 1.3.:

Improvement of the resolution of XRD measurements of PSII. *Blue Dots:* 3.8 Å: Zouni et al. [2001], 3.7 Å: Kamiya and Shen [2003], 3.5 Å: Ferreira et al. [2004], 3.2 Å: Biesiadka et al. [2004], 3.0 Å: Loll et al. [2005], 2.9 Å: Guskov et al. [2009]. *Red dot:* 1.9 Å: Umena et al. [2011].



complex catalyzes the oxidation of water molecules. During this process, it cycles through different redox states and molecular oxygen is emitted. The cycle is known as the *Kok cycle*, the states are named *S-states*.

In the classical Kok cycle, five states S_0 , S_1 , S_2 , S_3 , and S_4 are distinguished [Kok et al., 1970] (compare Fig. 1.4). With exception of the $S_4 \rightarrow S_0$ step, absorption of one photon is needed to progress from one S-state to the next. Each step increases the oxidation state of the manganese complex. One dioxygen molecule is released in the $S_4 \rightarrow S_0$ transition:



Here, the state S_1 is dark-stable, whereas S_2 and S_3 decay toward the S_1 -state within seconds or minutes [Styring and Rutherford, 1988; Messinger et al., 1993]. The manganese complex in the S_0 -state is oxidized slowly with a half-time of roughly 20 min to the S_1 -state for PSII located in intact thylakoid membranes [Styring and Rutherford, 1987].

1.2. X-ray absorption spectroscopy

X-ray absorption spectroscopy (XAS) is a spectroscopic method, which can be used to get information about atoms of a certain element and their surroundings. The method has its origin in the field of solid-state physics, but is today also widely used for biological samples (BioXAS; for an early example, see [Sayers et al., 1975]). For this thesis the so called *EXAFS* (extended X-ray absorption fine structure) region of XAS spectra is of special interest.

In the following, this method and its theory will be described and also an introduction to the *linear-dichroism* (LD) effect of XAS will be given. For further reading on XAS, see [Teo and Joy, 1981; Teo, 1986; Koningsberger and Prins, 1988; Stöhr, 1992; George et al., 1998; Rehr and Albers, 2000; Newville, 2008].

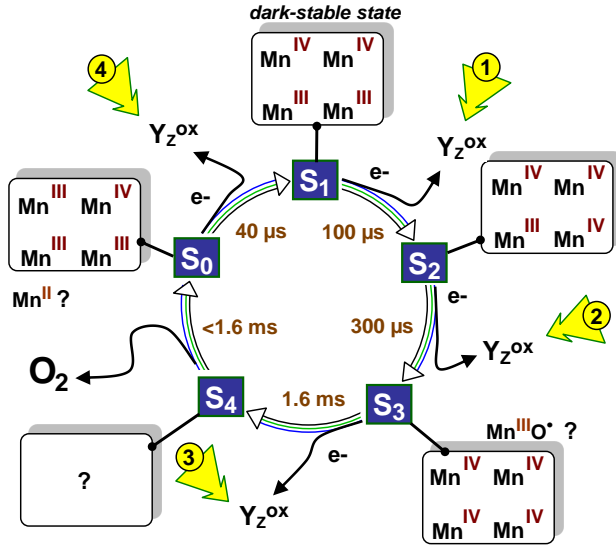


Figure 1.4.:

S-state (or Kok) cycle of photosynthetic water oxidation as proposed by Kok et al. [1970] with typical time constants of the electron transfer steps. Also likely oxidation states for the Mn ions are shown. (See [Dau and Haumann, 2007b] for an extension of this classical Kok cycle.) Figure from Grundmeier and Dau [2012].

1.2.1. Introduction

X-ray absorption spectroscopy (XAS) is based on the absorption of a photon in the X-ray region by a core electron (photoelectric effect). If the binding energy of the core level is less than the energy of the incident X-ray photon, the electron is excited to the continuum.

An important variable for XAS is the absorption coefficient μ , which is defined by the *Beer-Lambert law* (or simply *Beer's law*):

$$I_1 = I_0 e^{-\mu t} \quad (1.2)$$

Here, I_0 is the intensity of the incoming X-ray beam, t the sample thickness, and I_1 the intensity of the transmitted beam.

For most X-ray energies E , the absorption coefficient, μ , depends on the energy as follows [Haken and Wolf, 1996]:

$$\mu(E) \propto \frac{Z^x}{E^3} \text{ with } 3 \lesssim x \lesssim 4 \quad (1.3)$$

Herein, the variable Z is the atomic number.

When the energy of the incident X-ray beam equals the binding energy of a core-level electron, the absorption and therefore μ increases drastically. This increase is known as *absorption edge*. Dependent on the shell from which the excited electron stems from, one speaks of a K-, L-, or M-edge.

The excited state may decay by emission of an X-ray photon. This process is known as *X-ray fluorescence*. Another possibility is the Auger effect (one electron drops to a lower level and a second electron is emitted to the continuum), which dominates for low X-ray energies (< 2 keV).

For measuring of X-ray absorption spectra, two modes exist:

1. Introduction

1. The *absorption mode* where the intensity, I_1 , of the transmitted X-ray beam is measured. Here, the absorption coefficient can be calculated using Beer's law:

$$\mu(E) \propto \ln[I_0/I_1(E)] \quad (1.4)$$

2. The *fluorescence mode* where the intensity, I_F , of the fluorescence is detected. The emission probability of a fluorescence photon is proportional to the absorption probability and therefore the intensity of the fluorescence, I_F , divided by I_0 is in first approximation (neglecting any damping effects by the sample) proportional to the absorption coefficient:

$$\mu(E) \propto I_F(E)/I_0 \quad (1.5)$$

It can be shown (see, e. g., [Newville, 2008]) that this approximation is valid for thin ($\mu t \ll 1$) or alternatively thick ($\mu t \gg 1$), dilute samples.

1.2.2. The EXAFS region of XAS spectra

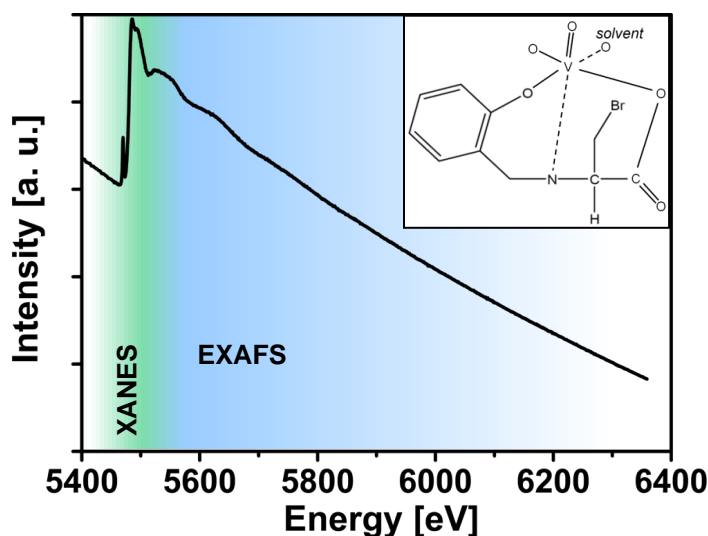


Figure 1.5.:

XAS spectrum for the vanadium compound shown in the inset measured by the author at BESSY [Grundmeier et al., 2008b]. EXAFS oscillations and a pre-edge peak are visible. The XANES and EXAFS regions are marked. The shown data were measured in absorption mode. The figure shows the spectrum after division of I_1 by I_0 and taking the logarithm as described by Eq. (1.4). See Fig. 1.7 for the fully evaluated EXAFS spectrum in the k domain and after applying a Fourier transform.

1.2. X-ray absorption spectroscopy

The *EXAFS* (extended X-ray absorption fine structure) region is the fine-structure after the absorption. The structure of the region around the edge is referred to as *XANES* (X-ray absorption near edge structure; compare Fig. 1.5). This EXAFS part of the XAS spectrum is normally analyzed as

$$\chi(E) = \frac{\mu(E) - \mu_0(E)}{\mu_0(E)}, \quad (1.6)$$

where $\mu_0(E)$ is a background function which is subtracted from the measured data (representing the case of absorbing atoms without any surrounding atoms).

Hereby, χ is usually written as a function of the wavenumber, k , of the emitted photoelectron instead of the energy, E , of the X-ray photon. The variables E and k are connected via the formula

$$k = \sqrt{\frac{2m_e}{\hbar^2}(E - E_0)}, \quad (1.7)$$

where E_0 is the threshold energy of the respective absorption edge and m_e the electron mass. Additionally, χ is often multiplied with k^3 (or k^2) to emphasize the EXAFS oscillations for higher k values by this k^3 (or k^2) weighting.

Typically, in the EXAFS region oscillations are visible. These oscillations can be explained by an interference effect: The emitted photoelectron is backscattered from the surrounding atoms and the electron wave interferes with itself. If the electron wave is only scattered by one atom, this is called *single scattering*. In case of successive backscattering processes from multiple atoms, one speaks of *multiple scattering*. The interference changes the electron wavefunction and therefore the absorption probability of photons at the position of the absorber. The energy of the incoming X-ray beam changes the interference pattern of the photoelectron wave. Therefore, oscillations are visible in the spectrum after the edge—the EXAFS. These oscillations contain information about atoms that surround the absorber.

This effect can be described by calculating the probability for the absorption of an X-ray photon. Fermi's Golden rule states that the transition rate, P_{if} , from the initial state, $|i\rangle$, to the final state, $|f\rangle$, is given by

$$P_{if} = \frac{2\pi}{\hbar} |\langle i|H|f\rangle|^2 \rho_f(E), \quad (1.8)$$

with an interaction term H , which here is defined by an time-dependent perturbation $V(t) = He^{-i\omega t}$ [Stöhr, 1992]. The function $\rho_f(E)$ is the energy density of final states [Koningsberger and Prins, 1988; Stöhr, 1992]. In the following, it is assumed that this factor is incorporated into the wavefunction normalization. For the absorption coefficient, μ , holds

$$\mu(E) \propto |\langle i|H|f\rangle|^2, \quad (1.9)$$

1. Introduction

where within the *dipole approximation* [Teo, 1986; Stöhr, 1992; Rehr and Albers, 2000] this expression can be rewritten in position space using the electric-field vector $\hat{\epsilon}$ and the electron coordinate \hat{r} as

$$\mu(E) \propto |\langle i | \hat{\epsilon} \cdot \hat{r} | f \rangle|^2. \quad (1.10)$$

By splitting $|f\rangle$ into two parts we obtain

$$|f\rangle = |f_0\rangle + |\Delta f\rangle, \quad (1.11)$$

where $|f_0\rangle$ relates to the absorber and $|\Delta f\rangle$ to the neighboring atoms. Thus, assuming that the backscattered photoelectron wave is sufficiently weak and therefore neglecting the square term $|\langle i | H | \Delta f \rangle|^2$ [Teo, 1986] substitution of (1.11) in (1.9) yields:

$$\mu(E) \propto |\langle i | H | f_0 \rangle|^2 \left[1 + \langle i | H | \Delta f \rangle \frac{\langle i | H | f_0 \rangle^*}{|\langle i | H | f_0 \rangle|^2} + \text{c.c.} \right] \quad (1.12)$$

Here, “c.c.” is the complex conjugate [Teo, 1986; Newville, 2008].

Equation (1.6) can be written as

$$\mu(E) = \mu_0(E)[1 + \chi(E)]. \quad (1.13)$$

Therefore, we get by comparing this expression with Eq. (1.12) and

$$\mu_0(E) \propto |\langle i | H | f_0 \rangle|^2 \quad (1.14)$$

for the fine-structure of XAS:

$$\chi(E) \propto \frac{2 \cdot \text{Re}(\langle i | H | \Delta f \rangle \langle i | H | f_0 \rangle^*)}{|\langle i | H | f_0 \rangle|^2} \quad (1.15)$$

Further evaluation of these expressions using the dipole approximation (see above) as well as the *plane wave approximation* (The size of the atoms is assumed as much smaller than the interatomic distances. Spherical photoelectron waves can therefore be approximated by plane waves [Teo, 1986].) and transformation from E to k values results in [Teo, 1986; Newville, 2008]:

$$\chi(k) = \frac{f(k)}{kR^2} \sin(2kR + \delta(k)) \quad (1.16)$$

Here R is the bond distance. The amplitude function, $f(k)$, and the phase shift, $\delta(k)$, are scattering properties of the neighboring atom. They depend on the Z value of the atom and, to a lower extent, on the (local) atomic structure of the investigated material.

For N atoms (N equals the coordination number.) at distance R this equation can be rewritten as

$$\chi(k) = \frac{N}{kR^2} e^{-2\sigma^2 k^2} f(k) \sin(2kR + \delta(k)). \quad (1.17)$$

The quantity σ^2 is the mean-square displacement in the bond distance R , known as the *Debye-Waller factor*. It reflects thermal movement and statistical disorder of the backscattering atom. It is connected to a Gaussian distribution of distances about the mean value R [Teo, 1986]:

$$G(R') = \frac{1}{\sqrt{2\pi\sigma^2}} e^{-\frac{(R'-R)^2}{2\sigma^2}} \quad (1.18)$$

Two more factors are usually added to Eq. (1.17):

$$\chi(k) = \frac{N}{kR^2} S_0^2 e^{-2\sigma^2 k^2} e^{-2R/\lambda(k)} f(k) \sin(2kR + \delta(k)) \quad (1.19)$$

This new quantities have the following meaning:

- The expression λ is the mean-free path of the photoelectron, reflecting both inelastic scattering and the core-hole lifetime.
- $S_0^2 \leq 1$ is known as the *amplitude reduction factor*, which takes into account multiple-electron excitation [Rehr 1978, Stern 1988]. Although methods for calculating this value do exist (e. g., [Roy et al., 2001]), mostly empirical values are used. Herein, for PSII S_0^2 is set to 0.85.

In the past, the functions $f(k)$, $\delta(k)$, and $\lambda(k)$ were determined experimentally from known structures, but today they are mostly calculated using computer programs like FEFF [Mustre de Leon et al., 1991; Rehr and Albers, 2000; Ankudinov and Rehr, 2003].

Until now, only one *coordination shell* consisting of N backscatterer atoms per absorber was taken into account. For the case of an arbitrary number n of coordination shells, Eq. (1.19) can be generalized [Teo and Joy, 1981; Teo, 1986; Koningsberger and Prins, 1988; Rehr and Albers, 2000; Newville, 2008]:

$$\chi(k) = \sum_{i=1}^n \frac{N_i}{kR_i^2} S_0^2 e^{-2\sigma_i^2 k^2} e^{-2R_i/\lambda(k)} f_i(k) \sin[2kR_i + \delta_i(k)] \quad (1.20)$$

This expression does not incorporate any multiple scattering effects.

Furthermore, it should be noted that due to the R_i^{-2} term and the $\lambda(k)$ function, the EXAFS method is a local method, i. e., only atoms close to the absorber atom (for proteins typically absorber-backscatterer distances up to 5 Å [George et al., 1998]) influence the EXAFS spectrum significantly and therefore can be detected.

1.2.3. XAS measurements and EXAFS data evaluation

Today, most XAS experiments are pursued at synchrotron radiation sources. Using a double-crystal monochromator the X-ray energy can be selected very precisely. As

1. Introduction

said above, XAS (and therefore also EXAFS) data can be measured in fluorescence or transmission mode (Fig. 1.6). In both cases, the intensity I_0 of the incoming X-ray beam has to be measured. This is typically done by using an ionization chamber. The intensity, I_1 , of the transmitted beam can be measured using a second ionization chamber, whereas the fluorescence intensity, I_F , is typically detected with a photodiode or an energy-resolving semiconductor detector (e. g., Ge detector).¹

EXAFS spectra for high concentrated samples are measured in transmission. Thin samples (EXAFS not visible in transmission) and also thick, but dilute samples (almost no transmission existing) should be measured in fluorescence mode. In these cases, the approximative formula from Eq. (1.5) holds. When measuring the fluorescence, filter foils can be used to eliminate elastically scattered X-rays (“ $Z-1$ ” low-pass filter, see [Newville, 2008]).

Additionally to acquisition of the XAS spectrum of the sample, typically an energy standard is measured in parallel to calibrate the energy axis of the spectra. The energy standard is a sample with a characteristic feature (e. g., K-edge, pre-edge peak) in its XAS spectrum of which the energy position is well known. For Mn-XAS for example, potassium permanganate (KMnO_4) is typically used. This chemical compound shows a distinct pre-edge peak at 6543.3 eV in its XAS spectrum. (It is important that the feature used for energy-calibration does not change due to radiation damage.)

For measurement of this energy-calibration spectrum, the X-ray beam after the second ionization chamber (with intensity I_1) is directed through the energy standard. Then the intensity, I_2 , of the outgoing X-ray beam is measured again with an ionization chamber (see Fig. 1.6). With I_1 and I_2 , the XAS spectrum of the energy standard can be calculated.

The evaluation of EXAFS spectra normally involves (at least) the following steps:

1. Energy calibration.
2. Subtraction of a smooth pre-edge background. Often a line or a polynomial is fitted to the pre-edge region of the spectrum.
3. Calculation of $\chi(E)$ by subtraction of a background function $\mu_0(E)$ (after the edge) plus normalization according to Eq. (1.6). Often a spline is used to approximate μ_0 .
4. Transformation to k space using Eq. (1.7) and multiplication with k^3 (or k^2) to emphasize the small oscillations for high k values (compare Fig. 1.7A).
5. Curve fitting of $\chi(k)$ based on Eq. (1.20) to determine distances R_i , coordination numbers N_i , and Debye-Waller factors σ_i^2 . The functions $f(k)$, $\delta(k)$, and $\lambda(k)$ can be calculated using programs like FEFF [Mustre de Leon et al., 1991; Rehr

¹Energy-resolving multi-element semiconductor detectors were employed for all XAS measurements of PSII samples discussed in this thesis.

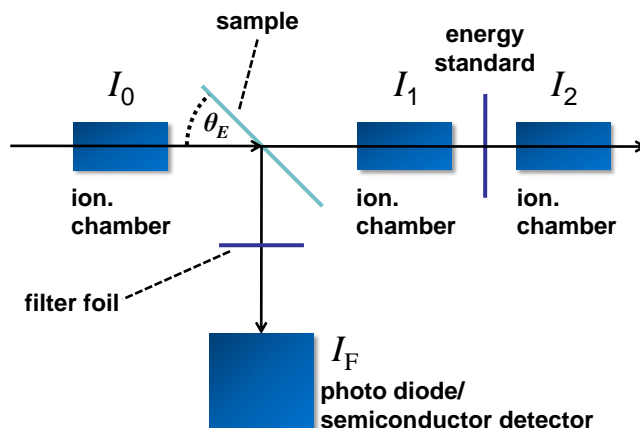


Figure 1.6.:

Scheme of a typical XAS experiment. The intensity I_0 of the incoming X-ray beam is measured by an ionization chamber. The beam then hits the sample and the intensities of the transmitted beam (I_1) as well as of the fluorescence (I_F) are measured. Often, a “Z-1” filter before the fluorescence detector absorbs most of the scattered X-rays. A spectrum of a second sample placed between the second (I_1) and a third (I_2) ionization chamber is used for energy calibration.

and Albers, 2000; Ankudinov and Rehr, 2003] based on a molecular structure similar to the one of the examined sample. In Fig. 1.7, an example for such a curve-fitting procedure is shown. (Alternatively, the data can be fitted after performing a Fourier transformation.)

The exact approach for each of these steps may vary and depends also on the data and the properties of the examined sample.

Often a Fourier transform of the $\chi(k)k^n$ spectrum is calculated. For this purpose, the data are multiplied with a window function $w(k)$ to reduce side lobes. A fractional cosine function, also named *Tukey window* [Harris, 1978; Tukey, 1967], may be used.² For all FT spectra shown in this thesis, the amplitude of the Fourier transform $|\mathcal{F}[\chi(k)k^n w(k)](R)|$ is displayed (see Fig. 1.7B for an example of an EXAFS spectrum in Fourier space).

Equation (1.20) predicts FT-peaks at the positions of the interatom distances, R_i , plus a small shift (typically 0.5 \AA), which occurs due to the phase shift $\delta_i(k)$ in the expression $\sin[2kR_i + \delta_i(k)]$. Therefore, these shifted distance values are called *reduced distances*. The heights of these peaks are among others determined by the coordination numbers, N_i , and by the Debye-Waller parameters, σ_i^2 .

²This window function is sometimes erroneously called *Hanning window* within the EXAFS literature, including the IFEFFIT software package [Newville, 2004].

1. Introduction

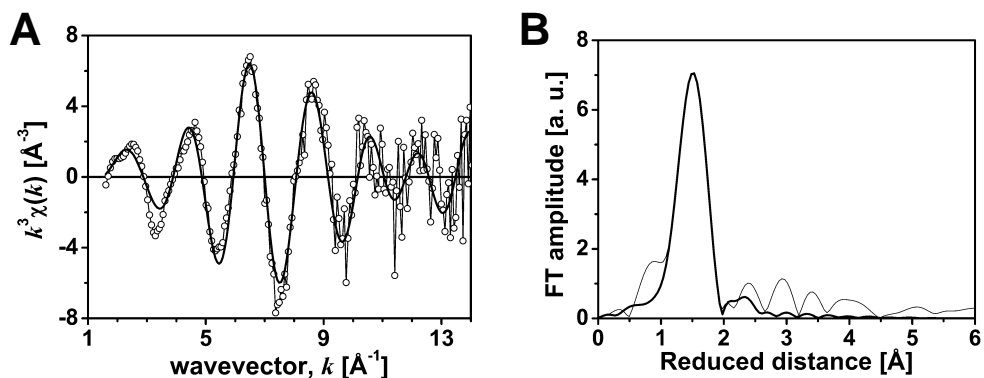


Figure 1.7.:

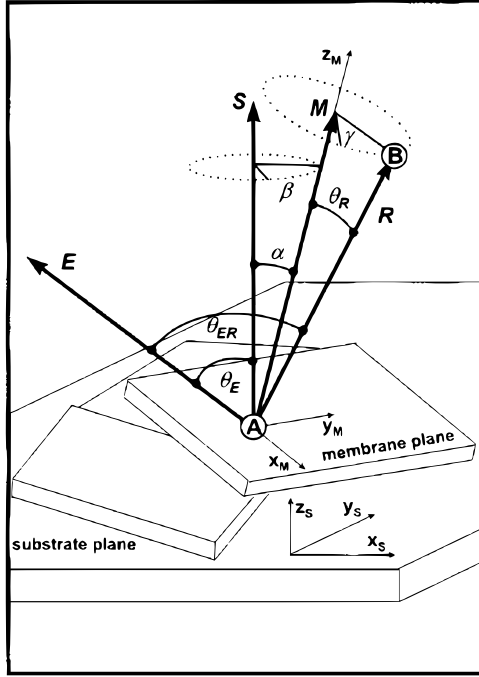
Evaluated EXAFS spectrum and fit result for the vanadium compound shown in Fig. 1.5. **A:** Spectrum in k space after multiplication with k^3 . Thin line with open circles depicts the experimental results, the thick line the curve-fitting results. Data modeling reveals one 1.58 Å distance (V=O bond), four 1.97 Å distances (V-O bonds), and one 2.48 Å distance (probably from the solvent). **B:** Amplitude of Fourier transform from spectra shown in A. A fractional cos-window from 0.9 to 12.5 Å⁻¹ with ramps spanning 10% at low and high k values was used.

1.2.4. Linear dichroism effect

Some of the formulas presented in Section 1.2.2, in particular Eq. (1.20), are only correct for isotropic (i. e., fully disordered) systems. Due to the polarized nature of synchrotron X-rays, the orientation of the investigated structure is important and influences the XAS spectrum. Most notably, the amplitudes of the EXAFS spectra can change. This effect is known as *linear-dichroism* (LD) effect. Through this effect, the orientations of binding vectors become accessible. In the article Dittmer and Dau [1998] a theory for the LD effect is presented for the case of single-scattering contributions to the EXAFS.

For samples that are at least partially ordered, the LD effect comes into play. In Fig. 1.8 an example for such a sample is given. PSII membrane sheets are stacked on a substrate. Overall, a preferential orientation does exist: On average, the membrane normal, M , points in the direction of the sample normal, S . Such a sample is called *partially oriented*. EXAFS spectra collected for such a sample depend on the angle θ_E between the sample normal and the electric field, E , of the X-ray beam.

In Dittmer and Dau [1998] the authors introduce a distribution function $P(\alpha, \beta, \gamma)$, which depends on the angles α , β , and γ reflecting the orientation of the vectors M and R with respect to the sample normal S (compare Fig. 1.8). The vector R connects an absorber and a backscatterer atom. In the case of an isotropic sample, the function P equals $(2\pi)^{-2}$, for crystals it consists of δ -functions.


Figure 1.8.:

Vectors and angles for a sample consisting of partially oriented membranes. The vector S is the sample normal, M is the normal of the membrane plane, E is the electric-field vector of the X-ray beam. The vector R connects an absorber atom, A , and a backscatter atom, B . The angle θ_{ER} is the angle between E and R , θ_R the angle between R and M , and θ_E the angle between E and S . The angles α , β , and γ describe the orientation of M and R . Reprinted with permission from Dittmer, J. and Dau, H. (1998). Theory of the linear dichroism in the extended X-ray absorption fine structure (EXAFS) of partially vectorially ordered systems. *J. Phys. Chem. B*, 102(42):8196-8200. Copyright 1998 American Chemical Society.

With such a distribution function, partially unidirectionally oriented systems can be defined by the characteristic that two vectors M and S exist such that $P(\alpha, \beta, \gamma)$ depends solely on α , i. e.:

$$P(\alpha, \beta, \gamma) = P(\alpha) \quad (1.21)$$

Dittmer and Dau consider the general case of a quantity χ depending on the energy ϵ and the direction of the electric field vector E given by the angle θ_{ER} between E and the absorber-backscatterer vector R . Moreover, for this χ two functions χ^c and χ^s should exist such that

$$\chi(\epsilon, \theta_{ER}) = \chi^c(\epsilon) \cos^2 \theta_{ER} + \chi^s(\epsilon) \sin^2 \theta_{ER}. \quad (1.22)$$

This assumption is true for the EXAFS function, χ , introduced in Section 1.2.2. In this case, χ^c and χ^s can be calculated equally to Eq. (1.19), but different functions $f(k)$, $\delta(k)$, and $\lambda(k)$ for χ^c and χ^s have to be used (compare Section 4.2 and Appendix A.2 for more details).

Starting from Eq. (1.22) and using the definition of a partially oriented system as described above (see Eq. (1.21)), the following equation is derived in Dittmer and Dau [1998]:

$$\chi(\epsilon, \theta_E) = \frac{1}{3}(\chi^c + 2\chi^s) + \frac{1}{6}(\chi^c - \chi^s)(3 \cos^2 \theta_E - 1)(3 \cos^2 \theta_R - 1)I_{\text{ord}} \quad (1.23)$$

Here, the variable θ_R is the angle between M and R and the order parameter I_{ord} with

1. Introduction

$0 \leq I_{\text{ord}} \leq 1$ is given by

$$I_{\text{ord}} = 2\pi^2 \int_0^{\pi/2} d\alpha (3 \cos^2 \alpha - 1) P(\alpha) \sin \alpha. \quad (1.24)$$

For an isotropic system $I_{\text{ord}} = 0$ holds.

Furthermore, in case of $\theta_E = \arccos \sqrt{1/3} \approx 55^\circ$ (the so called *magic angle*) the second summand of Eq. (1.23) vanishes. In this case, χ equals the result for an equivalent isotropic system ($I_{\text{ord}} = 0$). If the XAS spectrum of an perfectly isotropic system is wanted, the sample should be measured with an angle of 55° between the E -field of the incoming X-ray beam and the sample normal M (orientation axis).

It should be noted that Eq. (1.23) has been derived for partially oriented systems, but can also be applied to crystals with specific symmetry groups. Among these groups is the $P2_12_12_1$ symmetry of the PSII crystals, as shown in Appendix A.1.

2. Structural models of the Mn complex – Present status

For understanding of the mechanism of photosynthetic water oxidation, the structure of the manganese complex of PSII is essential. Before the first successful X-ray crystallographic data of photosystem II was measured by Zouni et al. [2001], various methods like X-ray absorption spectroscopy (XAS) [Yachandra et al., 1986; MacLachlan et al., 1992; Yachandra et al., 1993, 1996; Penner-Hahn, 1998; Dau et al., 2001; Sauer et al., 2005; Dau and Haumann, 2008; Sauer et al., 2008], electron paramagnetic resonance (EPR) and electron nuclear double-resonance (ENDOR) spectroscopy [Dismukes and Siderer, 1981; Evelo et al., 1989; Miller and Brudvig, 1991; Pace et al., 1991; Hasegawa et al., 1999; Ioannidis et al., 2002; Olesen and Andreasson, 2003; Britt et al., 2004; Kulik et al., 2005; Haddy, 2007; Teutloff et al., 2009; Pantazis et al., 2009], Fourier-transform infrared (FTIR) spectroscopy [Hillier and Babcock, 2001; Yamanari et al., 2004; Noguchi, 2008; Debus, 2008] were used to examine the OEC and also develop models of the manganese complex [Brudvig and Crabtree, 1986; Vincent and Christou, 1987; Sauer et al., 1992; Klein et al., 1993; Yachandra et al., 1993; Rüttinger and Dismukes, 1997; Peloquin et al., 2000].

Due to the successful X-ray diffraction measurements on photosystem II [Zouni et al., 2001] and the steady improvement in this field [Kamiya and Shen, 2003; Ferreira et al., 2004; Biesiadka et al., 2004; Loll et al., 2005; Guskov et al., 2009] and most recently [Umena et al., 2011] (compare Fig. 1.3) as well as new approaches with X-ray absorption spectroscopy (XAS) like extended-range EXAFS (Section 3.3) and LD-EXAFS (Section 1.2.4), more and more information about the OEC is becoming available [Sauer et al., 2005; Yano et al., 2005b; Pushkar et al., 2007; Dau et al., 2008]. As a result of this development, several promising models of the manganese complex of photosystem have been proposed in recent years based on information of these new techniques [Yano et al., 2006; Sproviero et al., 2008b; Dau et al., 2008].

In the following chapter, an overview over the historical development of the in literature proposed models of the manganese complex is given and also the influential articles of Yano et al. [2006] and Sproviero et al. [2008b] are summarized.

2. Structural models of the Mn complex – Present status

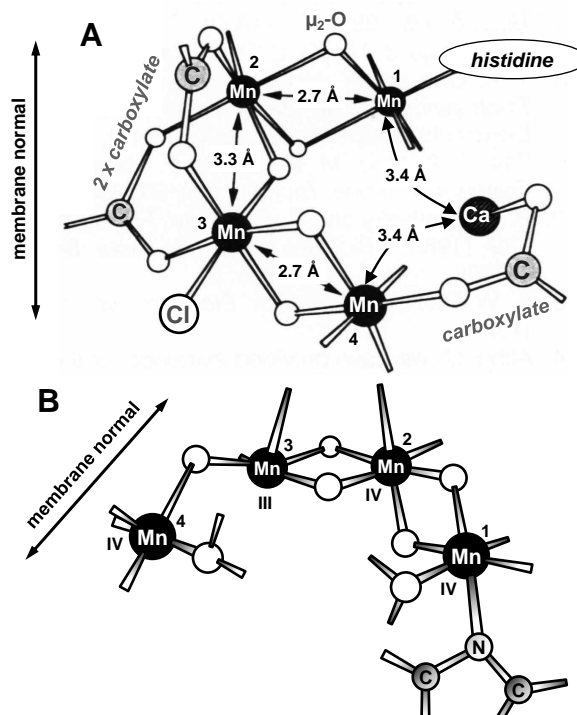


Figure 2.1.:

Early models of the manganese complex of PSII. Oxygens are shown as white spheres, all other elements are labeled in the figure. The approximate direction of the membrane normal is shown. **A:** Dimer-of-dimers model proposed by Yachandra et al. [1993] (S_1 - and S_2 -state). **B:** Dangler model of Peloquin et al. [2000]. For further explanations of these models see text. Figure from Grundmeier and Dau [2012].

2.1. Early models based on EXAFS and EPR results

Before crystallographic information became available, it was suggested that the center of the OEC contained four manganese, one calcium, and probably one chloride ion [Yachandra et al., 1996; Debus, 1992; Yocum and Pecoraro, 1999]. X-ray absorption spectroscopy was widely used to gain information about the structure of the OEC [Yachandra et al., 1996, 1986, 1993; Goodin et al., 1984]. It should be noted that the information from experiments gained at cryogenic temperatures (as normally used for EXAFS on PSII) is equivalent to the information obtained at room temperature [Meinke et al., 2000; Haumann et al., 2002a,b, 2005].

Symmetric Mn_4O_n structures like the *butterfly* or the *cubane* model from Christou and Dismukes [Vincent and Christou, 1987; Rüttinger and Dismukes, 1997] or the cubane-adamantane model of Brudvig and Crabtree [1986] could be rejected early. Another well known early model was the *dimer-of dimers* (DoD) model from the Berkeley group proposed in 1993 [Yachandra et al., 1993; Sauer et al., 1992; Klein et al., 1993]. This model (shown in Fig. 2.1A) consists of two Mn dimers where each dimer is a di- μ -oxo bridged Mn_2 unit. This model was based on EXAFS results which showed that 2–3 Mn-Mn vectors with a length of roughly 2.7 Å must exist. This distance is typical for di- μ_2 -oxo bridges between Mn^{III} or Mn^{IV} ions (see Table 2.1 for a list of metal-metal distances in the manganese complex predicted based on EXAFS results). The two $Mn-(\mu_2-O)_2-Mn$ dimers of the DoD model are connected by mono-

2.2. Protein crystallography and OEC structure

μ_2 -oxo, bis-carboxylato bridging which results in a 3.3 Å Mn-Mn distance (compare Table 2.1). It was assumed that the chloride was a ligand of one of the manganese ions; a hypothesis that was later disproven [Haumann et al., 2006] (see further below). Also, a 3.4 Å distance between Mn^1 and Ca as well as Mn^4 and Ca was assumed. This distance has been confirmed with Ca and Sr (substituting Ca) XAS [Cinco et al., 2002; Müller et al., 2005]. The presence of the histidine (bound to Mn^1) was concluded from EPR measurements [DeRose et al., 1991].

Additionally, it was known in 1993 by polarized EXAFS measurements that the two 2.7 Å-Mn-Mn vectors have an angle to the membrane normal that is greater than 54.7° , the magic angle [George et al., 1989; Yachandra et al., 1993] (see Section 1.2.4). This result was confirmed repeatedly [Mukerji et al., 1994; Liang et al., 1994; Dau et al., 1995; Schiller et al., 1998; Dau et al., 2001; Pushkar et al., 2007]. For the Mn-Ca vector it was found that here the angle should be smaller than 54.7° [Cinco et al., 2004]. However, the alignment of the 3.3 Å-Mn-Mn vector parallelly to the membrane normal was not confirmed by polarized EXAFS measurements of Pushkar et al. [2007].

Based on EPR results, Britt and coworkers proposed in 2000 the *dangler* model (Fig. 2.1B) [Peloquin et al., 2000]. In this model three manganese ions (Mn^1 , Mn^2 , and Mn^3) are connected by di- μ -oxo bridges. The fourth Mn ion (Mn^4) is connected to this Mn_3 core by a mono- μ -oxo bridge.

In 1997, Hoganson and Babcock made an important proposal regarding the mechanism of oxygen-oxygen bond formation (*hydrogen-atom abstraction*, HAA) based on the DoD model [Hoganson et al., 1995; Hoganson and Babcock, 1997; Tommos and Babcock, 1998]: They suggested that the Tyr_Z becomes a neutral radical after oxidation and deprotonation. This radical could abstract H-atoms from two water molecules bound to the terminal Mn ions in the DoD model (Mn^1 and Mn^4). Eventually, an O-O bond is formed between these two Mn-oxo species.

2.2. Protein crystallography and OEC structure

Crystallographic models and their improvement over the last 10 years played an essential role in development of a realistic model of the OEC structure (compare Fig. 1.3). From the beginning, XRD gave some essential answers, e. g., regarding possible ligands of the Mn complex, and it was also possible to exclude some previously proposed models.

The first XRD data with a resolution of 3.8 Å was presented in 2001 by Zouni, Fromme, Krauss, Saenger, Witt, and coworkers [Zouni et al., 2001]. For these measurements the thermophilic cyanobacterium *Synechococcus elongatus* was used, because of the stability of its proteins. Zouni et al. were able to locate the Mn complex and therefore determine the amino acid residues in its environment. Unfortunately, the ligands of the Mn and Ca ions could not be identified. However, due to the size of

2. Structural models of the Mn complex – Present status

Table 2.1.:

EXAFS results for Mn-Mn and Mn-Ca distances in the manganese complex of PSII (S_1 -state). The first column indicates the type of bond, the second column the expected length R of the bond, and the third column the number of bonds of such type. In column four a assessment of this bond type is listed. The angle θ_R between the metal-metal vectors and the membrane normal is shown in the last column. Table adapted from Grundmeier and Dau [2012].

bond	R [Å]	number	assessment	avg. θ_R [°]
Mn-Mn	2.65–2.8	2	clearly present	> 60
Mn-Mn	2.8–2.9	0 or 1	presence disputed	> 60
Mn-Mn	2.9–3.1	?	possibly present	?
Mn-Ca	3.2–3.6	≥ 2	undisputed	< 45
Mn-Mn	≈ 3.3	1?	recently proposed	> 60
Mn-Ca	≈ 3.7	?	in conflict with Ca/Sr EXAFS?	?
Mn-Mn	≈ 3.7	1?	recently proposed [Dau et al., 2008]	?
Mn-Mn	≈ 4.8	1?	possibly present [Grundmeier and Dau, 2012]	?
Mn-Me	> 5	?	identification not possible	?

the complex, the DoD as well as the dangler model could be excluded. Additionally, the distance between the TyrZ and the Mn ions was too high too allow the HAA model from Babcock and coworkers. In 2003, the results from Zouni et al. [2001] could be reproduced by 3.7 Å XRD data measured by Kamiya and Shen [2003].

The next huge step occurred in 2003, when Barber and coworkers could present crystallographic results with a resolution of 3.5 Å [Ferreira et al., 2004] (compare Fig. 2.2). They succeeded in locating the Ca ion in a distance of 3–4 Å to three Mn ions in agreement with EXAFS data (Table 2.1). With this result, it was established that the Mn complex was a pentameric Mn_4Ca complex. Barber et al. suggested a $CaMn_3(\mu-O)_4$ cubane with a fourth Mn ion (Mn^4) connected to one of the oxygens of this cubane (similar to the dangler model of Britt and coworkers [Peloquin et al., 2000]). Unfortunately, the resolution was still not high enough to assign correctly the ligating amino acids.

In 2005, Zouni and coworkers published XRD data of PSII with a resolution of 3.0 Å [Loll et al., 2005] (protein data bank accession code 2AXT). Due to the still insufficient resolution and likely radiation damage, in this article no suggestions were made regarding the oxygens bridging the metal ions. Nevertheless, twelve ligating amino acid residues could be assigned (eleven oxygen ligands of carboxylate sidechains

2.2. Protein crystallography and OEC structure

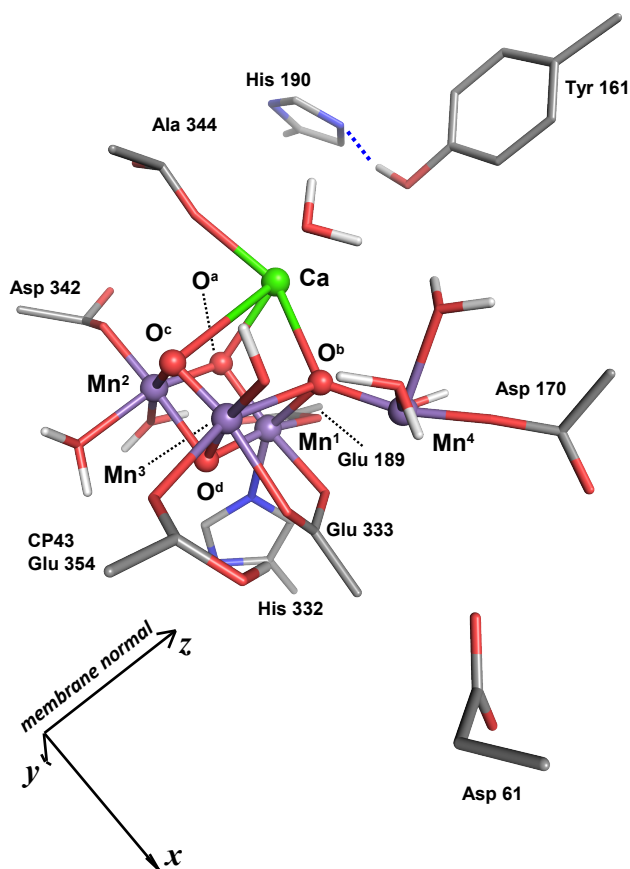


Figure 2.2.:

OEC model R-QM/MM from Sproviero et al. [2008b] (S_1 -state) based on the crystallographic model presented by Ferreira et al. [2004] and EXAFS data from Yano et al. [2006] and Haumann et al. [2005]. Important modifications to the structure presented in Ferreira et al. [2004] are the removal of the originally suggested bicarbonate ligand and complementation by additional water molecules or hydroxides. All depicted residues are from the D1 protein of PSII, with the exception of Glu354, which is a residue of the CP43 protein. *Remark:* For this figure (and also the calculations for B-II) coordinates personally communicated were used which slightly deviate from the ones given in the supporting material of the article Sproviero et al. [2008b]. Figure from Grundmeier and Dau [2012].

and one nitrogen ligand of a ligating histidine; Fig. 2.3). For only two of these ligands, diverging results were found in the latest XRD analysis of Umena et al. [2011]. This model as well as the earlier EXAFS-based model of Dau et al. [2008] suggests a special role of Mn^4 where two water molecules are bound. Therefore, it may play a crucial role in the generation of the oxygen-oxygen bond.

One year later in 2006, XAS at the Br K-edge showed (after substitution of the chloride cofactor by bromide) that the halide cofactor is not bound to a metal ion of the OEC [Haumann et al., 2006] (see also [Dau et al., 1999; Rehder et al., 2000]). This result was later confirmed by XRD studies [Murray et al., 2008; Kawakami et al., 2009; Guskov et al., 2009]. Therefore, the Mn complex is not a Mn_4CaCl complex and it now is believed that chloride is not directly involved in the process of water oxidation (but possibly in protein transfer steps).

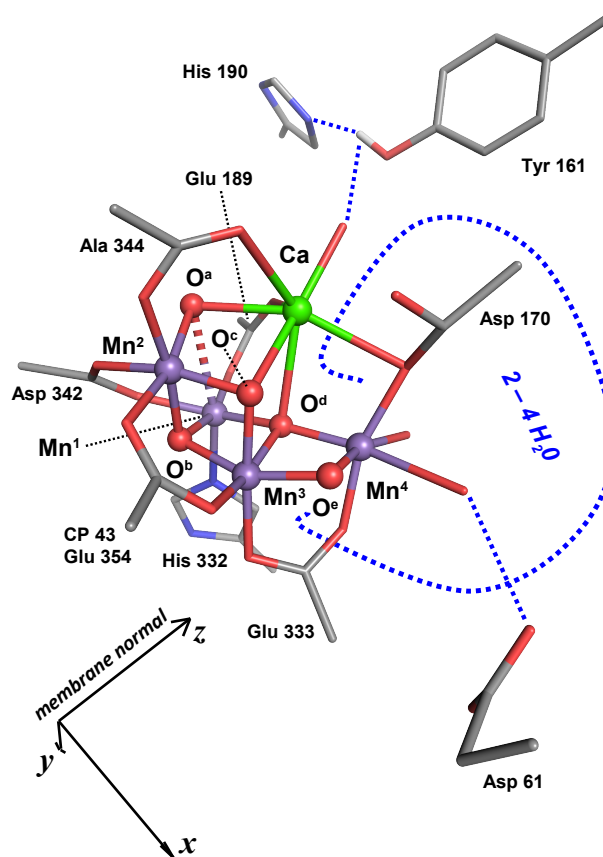
In 2009, the workgroup around Zouni and Saenger could increase the resolution of PSII XRD data from 3.0 Å to 2.9 Å by reprocessing the old XRD data 2AXT [Loll et al., 2005] with an improved software package [Guskov et al., 2009] (accession codes 3BZ1 and 3BZ2 for the coordinate files of the two monomers).

In fall of 2010, Shen presented at an international photosynthesis congress in Beijing,

2. Structural models of the Mn complex – Present status

Figure 2.3.:

Model of the OEC presented in Dau et al. [2008]. The ligating amino acids are connected to the Mn ions as shown in the XRD data of Loll et al. [2005]. The model was obtained by molecular mechanics modeling using HyperChem 7, Hypercube, and taking into account the extended-range EXAFS data from Dau et al. [2008]. The result is similar to models of Siegbahn [2008, 2009] and Umena et al. [2011]. Hydrogen bonds are depicted as blue dashed lines. It is assumed that 2–4 additional water molecules are located close to Mn^4 . The approximate region is margined in the figure using a blue dotted line. With the exception of Glu 354 (residue of CP 43), all shown residues are from the D1 protein of PSII. In this model, the Mn^1 ion is quasi five-coordinated with a long distance between Mn^1 and O^a (dashed bond). *Remark:* Only the proton bound to Tyr_z (Tyr 161) is depicted, all other protons are omitted. Figure from Grundmeier and Dau [2012].



China, new XRD results for PSII with an astonishing resolution of 1.9 Å. In contrast to the previous XRD measurements, this time *Thermosynechococcus vulcanus* was used as species for extraction of PSII. The results were later published in the article Umena et al. [2011] (accession code 3ARC). Due to the high resolution it was possible, to identify clearly the binding modes of the amino acid residues (see Fig. 2.5). As already mentioned above, the results from Loll et al. [2005] regarding the ligand assignment could largely be confirmed (compare Fig. 2.4). Two notable exceptions are the bridging of Mn^4 and Ca by Asp 170 in the data of Shen and coworkers and also the missing bond between Glu 189 and the Ca ion, which the XRD data of Loll et al. suggested. Instead of bridging Mn^1 and Ca, in the XRD data of Shen and coworkers Glu 189 is only a ligand to Mn^1 . These two differences are partly due to a changed position of the Ca ion. The very high resolution also allowed for resolving the bridging between the ligating amino acids and the metal ions. Additionally, the bridging oxygens (named O^a to O^e in this work) between the metal ions as well as more than 1,300 water molecules per PSII monomer were made visible (2,795 water molecules per dimer).

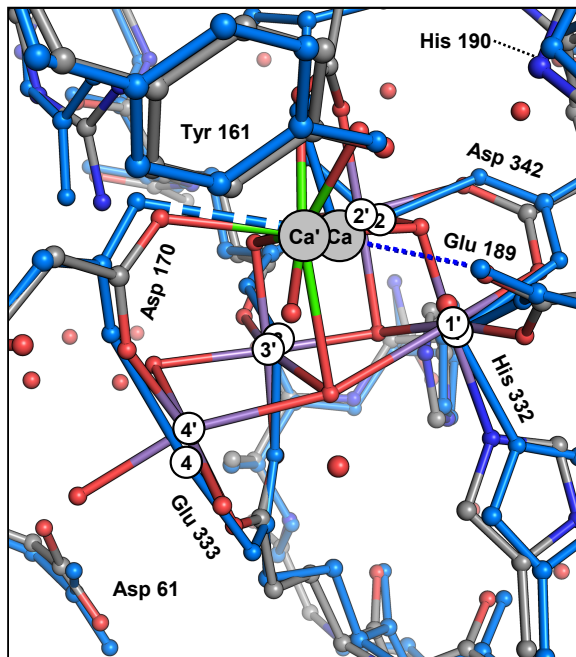


Figure 2.4.:

Comparison of crystallographic data sets 3ARC published by Umena et al. [2011] (1.9 Å resolution; colored by element code) and 2AXT from Loll et al. [2005] (3.0 Å resolution; blue). The spheres with labels 1, 2, 3, 4 and Ca depict the position of the metal ions in the model of Loll et al., whereas the spheres with primed numbers respectively Ca' refer to the model of Umena et al. *Remark:* The XRD data set 3ARC was rotated and shifted to maximize the correspondence between the two crystal structures. This was done using the `align` command of PyMOL [DeLano Scientific, LLC, 2008] and considering only atoms with an approximate distance between 7 and 20 Å to the Mn ions. Figure from Grundmeier and Dau [2012].

It should be noted that in the XRD data 3ARC of Umena et al. [2011], the dimensions of the PSII unit cell are given as $a \approx 122$ Å, $b \approx 228$ Å, and $c \approx 286$ Å and therefore differ significantly from the values $a \approx 128$ Å, $b \approx 225$ Å, $c \approx 306$ Å given in Loll et al. [2005] (accession code 2AXT). Additionally, the dimers in 3ARC are slightly rotated in respect to the dimers of 2AXT. These deviations of the XRD results from each other might *inter alia* be due to the different species used (*Thermosynechococcus elongatus* vs. *Thermosynechococcus vulcanus*) or have their origin in differences between the crystallization procedures.

2.3. Radiation damage

Modifications of the structure of the OEC by X-ray photoreduction (*radiation damage*) of the manganese atoms is a very critical problem when examining PSII samples with XAS. Even though the samples are typically measured at low temperatures (often 20 K are used), photoreduction normally still occurs and is detectable through the shift of the Mn-edge position [Dau et al., 1997; Schiller et al., 1998; Haumann et al., 2005].

Radiation damage is expected also for the case of XRD (measured at typically 100 K) where the intensity of the X-ray beam is normally magnitudes higher than for XAS [Dau et al., 2004]. The positions of the metal ions of the OEC (and their ligating oxygens) shown in XRD data therefore deviates probably from their original positions. The results presented by Ferreira et al. [2004] and Loll et al. [2005] most

2. Structural models of the Mn complex – Present status

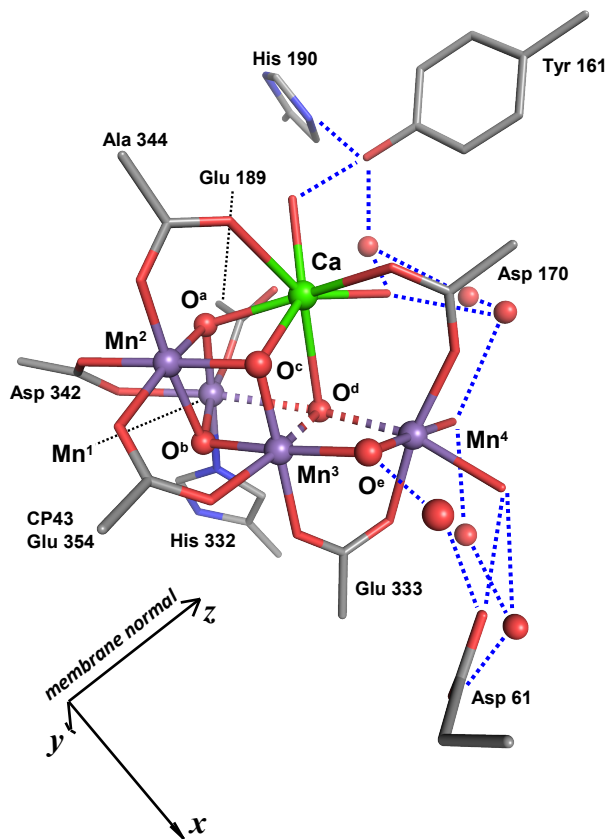


Figure 2.5.:

Manganese complex of PSII as obtained by the XRD measurements from Umena et al. [2011]. The Mn-O bonds with a length greater than 2.3 Å are shown as broken sticks. Oxygen atoms of selected water molecules are depicted as red spheres, possible hydrogen bonds as blue dashed lines. Figure from Grundmeier and Dau [2012].

likely shows a Mn complex close to an all-Mn^{II} level. This was in 2005 confirmed by XAS measurements on single-crystals of PSII [Yano et al., 2005a].

For the XRD measurements presented in Umena et al. [2011], the authors tried to avoid radiation damage by applying an optimized protocol for data collection. Nevertheless, the Mn photoreduction is still clearly visible in the data: Mn-Mn and Mn-O distances are partly in stark conflict to results from XAS measurements. (For further discussion of the model of Umena et al. [2011] and possible radiation damage, see Section 5.4.)

The influence of the radiation damage on the ligating amino acid residues is still unclear. The low temperature of 100 K used for X-ray crystallography might be enough to keep the system in a stable state and thus the positions of the amino acids might be accurate in the XRD data. On the other hand it was shown [Dau et al., 1997] that each absorbed X-ray photon generates several hundred radicals. Therefore, even major changes of the protein environment due to X-ray photoreduction seem possible.

2.4. Combining XAS and XRD data

Due to lower X-ray intensities and special measurement protocols to further reduce radiation damage (supporting information of Haumann et al. [2005]), XAS (especially EXAFS) is a very good method to examine the structure of the manganese complex of PSII and complement the XRD data of the OEC.

In the following, summaries of two prominent articles will be given, which proposed models of the Mn complex solely based on EXAFS results [Yano et al., 2006] and EXAFS in combination with XRD studies [Sproviero et al., 2008b], respectively. Furthermore, a third approach presented in Dau et al. [2008] will be described using extended-range EXAFS (compare Chapter 3 of this thesis) and the crystallographic data from Loll et al. [2005].

2.4.1. Models of Yano and coworkers

In 2006, Yano and coworkers presented a group of models of the manganese complex which are based on EXAFS measurements on PSII crystals (see Fig. 2.6) and comparison of these results to simulated spectra [Yano et al., 2006].

In this article, PSII crystals from *Thermosynechococcus elongatus* in the S_1 -state were examined. Using an X-ray beam with an E -field vector parallel to one of the three crystal axes (a , b , or c), EXAFS spectra were collected. The Fourier transforms of the measured EXAFS spectra are shown in Fig. 2.7. Obviously, the heights of the three main peaks at ~ 1.8 Å (mainly Mn-O distances), ~ 2.7 Å (mainly Mn-Mn), and ~ 3.3 Å (mainly Mn-Mn/Mn-Ca) depend clearly on the crystal axis.

Yano et al. used these experimental data to compare it to EXAFS spectra calculated by FEFF for 18 in literature proposed models of the manganese complex (see Fig. 2.8) plus topologically equivalent structures. In a first step, they compared their experimental data with simulated spectra from XRD-based models from Ferreira et al. [2004] (3.5 Å resolution) and Loll et al. [2005] (3.0 Å). In their article they come to the conclusion that the differences between the spectra are most likely due to limited resolution and X-ray damage [Yano et al., 2005a].

Then, they compared the experimental data to simulated spectra calculated for several previously proposed models of the manganese complex: Each model was rotated stepwise. EXAFS spectra were simulated for each of these orientations. Yano and coworkers focused in their analysis on the second and third peak originating mainly from Mn-Mn and Mn-Ca distances.

Yano and coworkers exclude all models without three Mn-Mn distances between roughly 2.7 Å and 2.8 Å based on the following findings:

- Analysis of extended-range EXAFS spectra (solution) published in Yano et al. [2005b].
- Shift of second peak to longer distance along a axis for polarized EXAFS data.

2. Structural models of the Mn complex – Present status

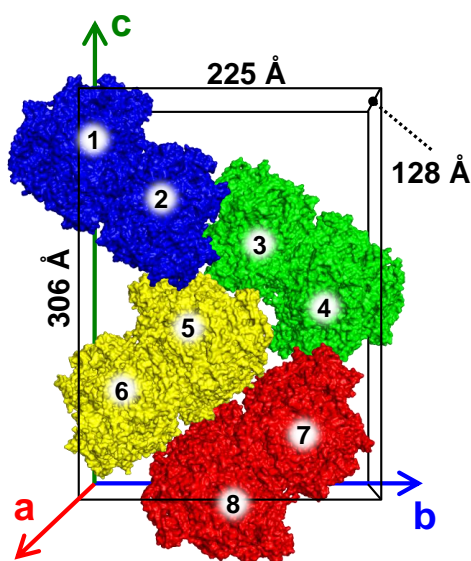


Figure 2.6.:

Unit cell of crystallized PSII with its four PSII dimers. The space group is $P2_12_12_1$. The numbers 1 to 8 mark the positions of the eight Mn complexes of PSII within the unit cell. For the measurements performed by Yano et al. [2006], the electric field vector E of the X-ray beam was parallel to one of the unit cell axes a , b , or c . The axes are shown in the same color as used for the according spectra in the figures displaying the spectra. The proportions of the unit-cell size were taken from the XRD data published in Loll et al. [2005] with accession code 2AXT. Figure adapted from Grundmeier and Dau [2012].

- Inability to reproduce intensity of second FT peak for polarized EXAFS data, especially for b and c axis. (This argument of Yano et al. is further discussed in Section 5.6.)

In the article Yano et al. [2006] it is outlined that all models containing only two distances in the 2.7 \AA region were unable to reproduce both the extended-range data from Yano et al. [2005b] and the crystal data.

Models with one or two Mn-Mn distances at around 3.3 \AA were used to find a matching model. In this context Yano states that based on EXAFS on solution samples the third peak is best simulated by one Mn-Mn vector at 3.3 \AA and two 3.4 \AA Mn-Ca distances as was shown in [Haumann et al., 2005]. Yano mentions that this finding is supported by Sr and Ca EXAFS [Cinco et al., 2002, 2004].

Finally, based on their calculations Yano et al. come to the conclusion that only one of the tested models (plus topological equivalents) is consistent with the experimental data, namely motif **r** from Fig. 2.8. This structure has been presented in Yano et al. [2005b] and Robblee et al. [2002]. In the article and its supporting online material, four

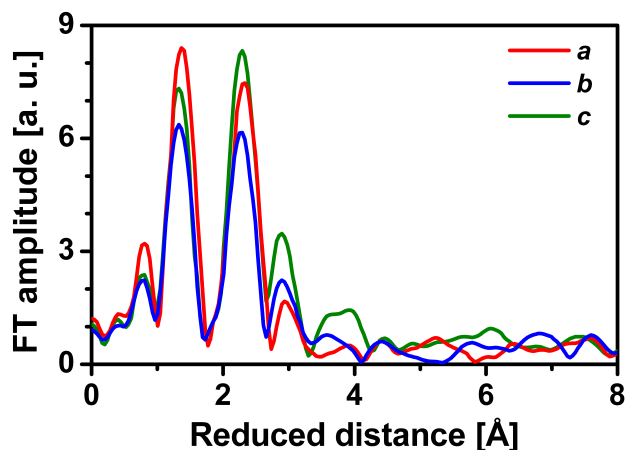


Figure 2.7.:

Fourier transform of polarized EXAFS spectra of PSII crystals as presented in Yano et al. [2006]. For these measurements, the electric field vector E of the X-ray beam was aligned along one of the three crystal axes a , b , and c . *Remark:* The data for this figure were taken from Fig. 1. (B) of Yano et al. [2006] and multiplied by a factor to be consistent with the amplitudes of the other Fourier transforms in this thesis. This factor was determined by comparing the FT of isotropic data from Yano et al. [2006] (Fig. 2. (B)) and a FT spectrum of the isotropic extended-range EXAFS data from Dau et al. [2008] calculated using the same E_0 value and window function as used by Yano and coworkers ($E_0 = 6561.3$ eV and a Tukey window from 3.0 to 12.0 \AA^{-1} with each ramp spanning 11.1% of the data [Yano, pers. comm.]).

models are distinguished, named model I, II, IIa (only mentioned in the supporting material), and III. These models are shown in Fig. 2.9.

Yano et al. states that all four models are very similar in regard to the second and third FT peak (The first peak is hard to model due to contributions of terminal ligands.). The authors were not able to discriminate between these models based on the EXAFS results. Additionally, four orientation are possible for each model due to the $\cos(\theta)^2$ dependence and the C_2 symmetry. Therefore, Yano and coworkers use the following informations to reduce the number of possible orientations:

- The placement of the calcium. In detail, the Mn-Ca vectors are aligned along the membrane normal [Cinco et al., 2004] and the Ca is expected to be above the Mn plane [Loll et al., 2005; Ferreira et al., 2004].
- The electron density distribution [Loll et al., 2005].
- Putative position of amino acids [Loll et al., 2005].

2. Structural models of the Mn complex – Present status

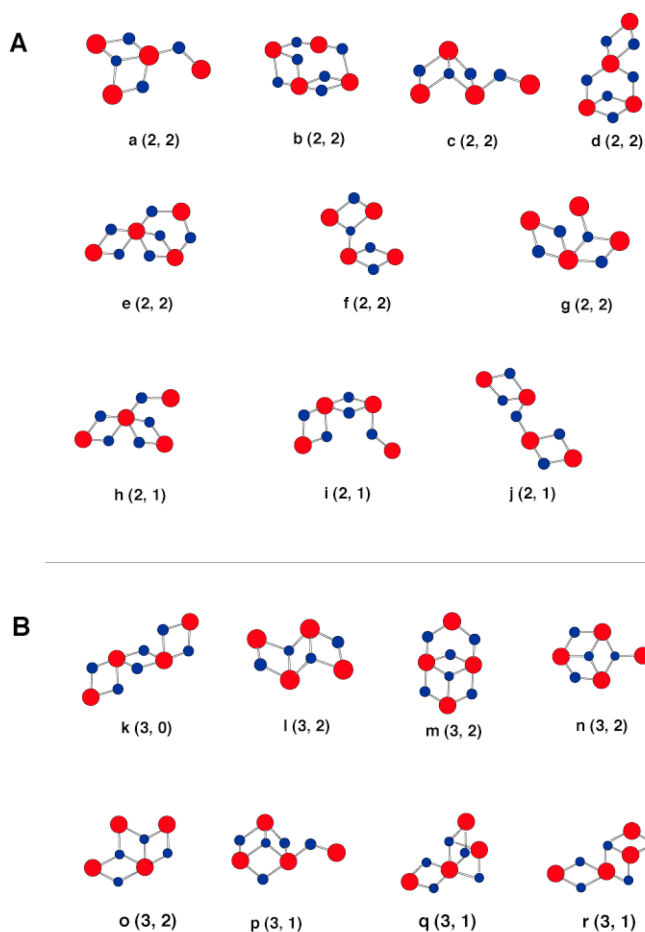


Figure 2.8.:

Structures of models tested by Yano et al. [2006]. In parentheses the number of short (2.7 to 2.8 Å) and long Mn-Mn (about 3.3 Å) distances is shown. Only topologically unique structures are shown. From supporting material of Yano, J., Kern, J., Sauer, K., Latimer, M. J., Pushkar, Y., Biesiadka, J., Loll, B., Saenger, W., Messinger, J., Zouni, A., and Yachandra, V. K. (2006). Where water is oxidized to dioxygen: structure of the photosynthetic Mn₄Ca cluster. *Science*, 314(5800):821-825. Reprinted with permission from AAAS.

The best orientations for each of the four models are shown in Fig. 2.9. Yano mentions that overlap between the models of the Mn complex and the ligand positions does exist and the assignment of the ligands has to remain tentative due to radiation damage during the XRD measurements.

2.4.2. Models of Sproviero and coworkers

In 2008 Sproviero and coworkers [Sproviero et al., 2008b] described a structural model (named R-QM/MM, see Fig. 2.2) of the Mn complex in the S₁-state based on experimental isotropic and polarized EXAFS spectra and a model of PSII named DFT-QM/MM developed by DFT and QM/MM calculations presented earlier [Sproviero et al., 2006, 2007, 2008a,c,e]. The DFT-QM/MM model (and therefore also the model R-QM/MM) uses as a starting point the XRD data 1S5L from *Thermosynechococcus elongatus* with a resolution of 3.5 Å [Ferreira et al., 2004].

In their article, Sproviero and coworkers state that polarized-EXAFS data calculated

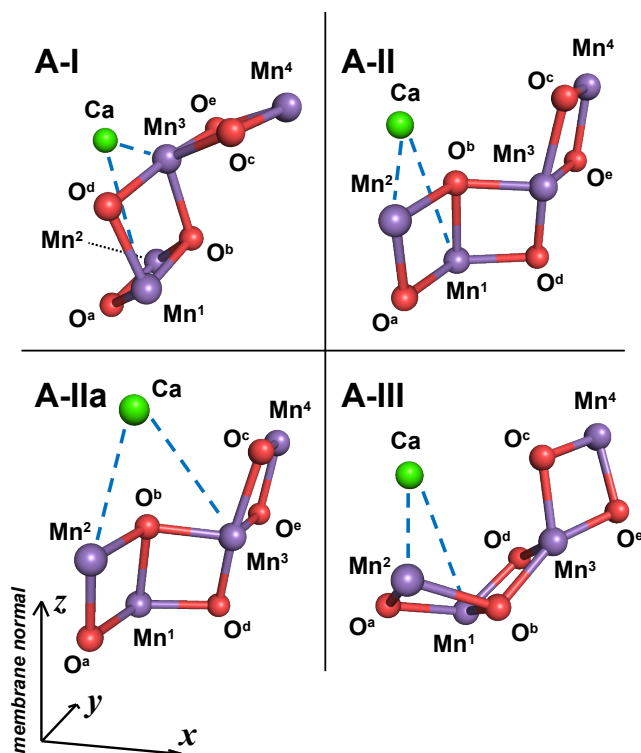


Figure 2.9.:

Proposed models I, II, IIa, and III of the manganese complex (S_1 state) from Yano et al. [2006] based on the polarized EXAFS spectra collected on PSII crystals. The z axis points in the same direction as the membrane normal, the x axis connects the two nonheme iron atoms of the PSII dimer. The distance between Mn^1 and Mn^2 is roughly 2.8 \AA for all four models. The other short Mn-Mn distances (Mn^1 - Mn^3 , Mn^3 - Mn^4) are $\sim 2.7 \text{ \AA}$ long. The two $\sim 3.4 \text{ \AA}$ Mn-Ca distances for each model are illustrated by dashed lines. Coordinates for these models (given in the coordinate system of the 3.0 \AA XRD structure 2AXT from Loll et al. [2005]) were taken from the supporting material of Yano et al. [2006]. *Remark:* In Fig. 3 of Yano et al. [2006], the x axis is displayed in a misleading way: The associated arrow points away from the other Mn complex of the dimer. This has been corrected. Therefore, the models shown here are rotated by 180° around the z axis in contrast to the ones depicted in the article Yano et al. [2006]. Figure from Grundmeier and Dau [2012].

2. Structural models of the Mn complex – Present status

from the coordinates of the XRD model from Ferreira et al. [2004] using FEFF deviate significantly from the experimental data of Yano et al. [2006]. They explain these differences with the relatively low resolution of the XRD data. Nevertheless, they assume a cuboidal core of the OEC in agreement with the XRD data. They note that the empirical models suggested by Yano et al. are neither consistent with such a structure nor the ligand environment suggested by the XRD data.

In the article it is stressed that in contrast to the models of Yano and coworkers, the model DFT-QM/MM is consistent with both a cuboidal Mn_3CaO_4 core with a dangler Mn atom and the distribution of the ligating amino acids as implied by the 1S5L XRD data. This model is also in agreement with the isotropic EXAFS spectra from Haumann et al. [2005]. Despite this, the calculated isotropic EXAFS spectra are not in good agreement with the spectra published in Yano et al. [2006].

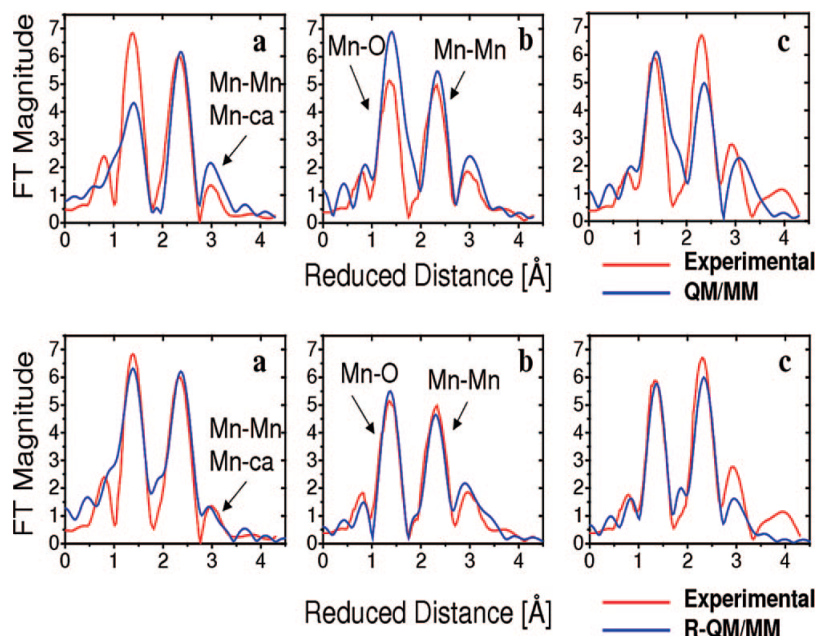


Figure 2.10.:

Fourier transform of polarized EXAFS spectra of PSII crystals for all three crystal axes *a*, *b*, and *c* for the DFT-QM/MM model (top) and the R-QM/MM model (bottom). Experimental spectra are shown as red, calculated spectra as blue lines. Reprinted with permission from Sproviero, E. M., Gascón, J. A., McEvoy, J. P., Brudvig, G. W., and Batista, V. S. (2008). A model of the oxygen-evolving center of photosystem II predicted by structural refinement based on EXAFS simulations. *J. Am. Chem. Soc.*, 130(21):6728-6730. Copyright 2008 American Chemical Society.

Therefore, Sproviero et al. further optimized this model DFT-QM/MM by refining the atom positions of the OEC based on FEFF simulation of isotropic and polarized

EXAFS spectra and comparison of these spectra to the experimental data. During this process, a sum of squared deviations between calculated and simulated spectra is minimized plus a penalty factor reflecting displacements of the atoms (with respect to the original DFT model). The spectra calculated for the resulting refined R-QM/MM model were found to be in good agreement to both the isotropic [Haumann et al., 2005] and the crystal spectra [Yano et al., 2006]. In Fig. 2.10, the original spectra published for both the DFT-QM/MM and the R-QM/MM (see Fig. 2.2) model are shown. In their article, Sproviero and coworkers emphasize that this result is only a local solution and other models may exist.

2.4.3. Model of Dau and coworkers

In Dau et al. [2008], a model based on the XRD structure 2AXT from Loll et al. [2005] in combination with extended-range EXAFS data (measured by the author of this thesis and presented in Chapter 3) was proposed (Fig. 2.3).

Starting from the crystallographic data 2AXT of Loll et al. [2005], the model was optimized by a molecular mechanics (MM) approach utilizing the program HyperChem. As mentioned in Section 3.4, for this optimization restraints were used, which were for intermetal distances based on curve-fitting results for extended-range EXAFS data (compare Table 3.1). Movement of the atoms were restricted to a relatively small range around Mn^1 , Mn^2 , and Mn^3 . To account for possible radiation damage, near Mn^4 greater deviations from the crystallographic model were allowed.

The model of Dau and coworkers is very similar to another model presented by Siegbahn and coworkers based on DFT calculations [Siegbahn, 2008, 2009]. Siegbahn et al. also are assuming a five-coordinated Mn^1 . However, for the model from Dau et al. [2008] a Jahn-Teller axis is assumed along the $\text{O}^a \cdots \text{Mn}^1\text{-N-His332}$ vector (resulting in a long $\text{Mn}^1\text{-O}^a$ distance), whereas the DFT calculations of Siegbahn show a Jahn-Teller axis along the $\text{O}^d \cdots \text{Mn}^1\text{-O-Asp342}$ vector (long $\text{Mn}^1\text{-O}^d$ distance). Despite this difference, both models are very similar and in good agreement to the XRD data from Umena et al. [2011].

A slightly more optimized version of this model (C-I) published in Grundmeier and Dau [2012] will be discussed further below in Section 5.5.

2.4.4. Conclusions

For all the models mentioned above, EXAFS results were taken into account. However, for none of them, all available types of EXAFS data (i. e., polarized EXAFS on partially oriented PSII membrane particles *and* polarized EXAFS on PSII crystals) were used.

For these models in Chapter 5 (and Grundmeier and Dau [2012]) LD-EXAFS spectra will be calculated and discussed in respect to experimental data. Additionally, new models are presented, which are optimized for all available EXAFS results and take into account the XRD results of Loll et al. [2005].

3. Improved distance resolution by extended-range EXAFS

In this chapter, the so called *extended-range EXAFS* method is introduced, which was used to examine PSII samples at the synchrotron DESY (Deutsches Elektronen-Synchrotron) in Hamburg, Germany. The results of these measurements, which were published in Dau et al. [2008], are discussed. Additionally, the sample preparation as well as the experimental setup are briefly described.

3.1. Preparation of samples

3.1.1. Preparation of PSII membrane particles

Photosystem II samples prepared from spinach (*Spinacia Oleracea*) were used for the XAS measurements. PSII from spinach typically normally has a high oxygen evolution, the preparations are relatively easy to perform, and comparability to many other experiments is given. The production of PSII enriched membrane particles was first described by Berthold, Babcock, and Yocum in Berthold et al. [1981] and is therefore widely referred to as *BBY preparation*. Later, Iuzzolino and coworkers improved this method [Iuzzolino et al., 1998]. (See also [Schiller and Dau, 2000] for additional information.) For this work a modified version of the prescription of Iuzzolino et al. [1998] was used [Schiller and Dau, 2000; Müller, 2006].

The isolated membrane particles were kept at a temperature of -80°C . The oxygen evolving rate for these samples under saturating white-light illumination and at 28° was determined to be at about $1200 \frac{\mu\text{mol of O}_2}{\text{mg of Chl.} \times \text{h}}$.

3.1.2. Preparation of partially oriented samples

Partially oriented samples consisting of oriented PSII membrane fragments were used for the EXAFS measurements. To produce such samples, the PSII membrane particles were treated as explained in detail in Müller [2006]. This procedure is again based on the work of Iuzzolino et al. [1998].

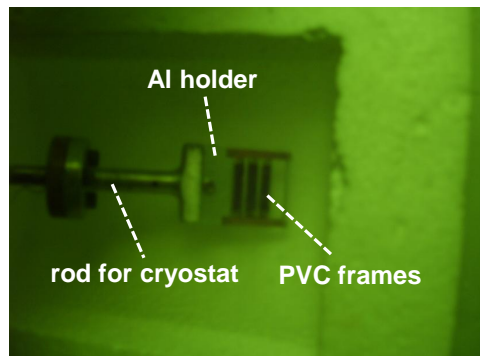
During this process, a solution containing the PSII membrane particles was centrifuged on thin Kapton foils held by small PVC frames (see Fig. 3.1). Directly after the preparation, the samples were illuminated from both sides with one pulse from a xenon

3. Improved distance resolution by extended-range EXAFS

flash lamp with a pulse length of app. $5\ \mu\text{s}$ (FWHM) and a wavelength of $\lambda > 400\ \text{nm}$. This step is necessary, to drive the majority of the PSII to the dark-stable S_1 -state. (Dark adapted samples have up to 25% of their centers in the S_0 -state and 75% in the S_1 -state; compare Section 1.1.3.) Therefore, directly after the flash most of the PSII are in S_1 - and S_2 -state. As a last step, these frames were dried for roughly 2 hours in dark at 10°C and at a pressure of $\approx 300\ \text{mbar}$. Afterwards, they were kept under liquid nitrogen and in total darkness until the measurements.

Figure 3.1.:

PVC frames with PSII membrane fragments under liquid nitrogen and green light directly after they were examined with XAS at DESY. The three shown frames are mounted on an aluminum holder, which itself is attached to the cryostat rod. Aluminum and PVC are used to avoid additional Fe fluorescence that could occur when using, e. g., steel.



3.2. Experimental setup and data collection

The XAS data were collected at a bending-magnet beamline of the DORIS III (*Doppel-Ring-Speicher*) synchrotron source (EMBL outstation at DESY, Hamburg). The data analysis was performed as described elsewhere [Iuzzolino et al., 1998; Schiller et al., 1998; Haumann et al., 2005] (see also Section 1.2.3).

During the measurements, the samples were kept in a liquid He cryostat at 20 K and the X-ray energy was scanned from 6420 to 7610 eV. Here, the samples were measured with an angle θ_E of roughly 55° between the electric-field vector of the X-ray beam and the sample normal (“magic angle”, see Section 1.2.4). After each scan of roughly 40 min duration the position of the sample in the beam was changed to reduce radiation damage. Approx. 75 XAS spectra were measured in fluorescence mode. An energy-resolving 13-element Ge detector from Canberra was used for data acquisition.

3.3. Extended-range EXAFS and data evaluation

The idea of the so called extended-range (also originally “range-extended”) EXAFS was first used in Gu et al. [2003]: When measuring EXAFS for an element (in this case Mn with K_α at approximately 5899 eV), normally only the measurement until the K-edge of the next element ($Z + 1$, here Fe with K_α at approximately 6404 eV and the K-edge at 7110 eV) is possible. This may reduce the quality of the EXAFS data

3.3. Extended-range EXAFS and data evaluation

drastically. A possibility to circumvent this problem is to measure the K_{α} fluorescences of both elements parallelly. After the measurement the weighted “ $Z + 1$ ”-signal can be subtracted from the polluted second signal to generate a pure spectrum.

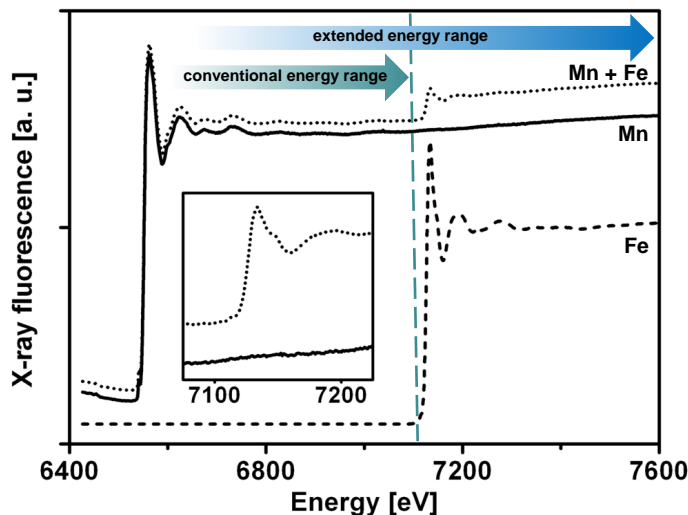


Figure 3.2.:

Mn and Fe XAS signals measured for PSII samples at DESY. For generating a pure Mn spectrum (solid line), the Fe signal (dashed line) was multiplied with an empirical factor and subtracted from the polluted Mn spectrum (dotted line). The inset shows the region around the Fe-edge on an expanded scale. The extended and the conventional (approximately up to the Fe-edge) energy ranges are marked by a blue and a green arrow, respectively. Figure adapted from Dau et al. [2008].

In the case of the measurements at DESY, in 11 discriminators of the 13-element Ge detector the windows were set to the Mn K_{α} -fluorescence. The remaining two measured the Fe fluorescence. The Fe spectra multiplied by a factor could then be subtracted from the whole spectrum as can be seen in Fig. 3.2. The choice of this factor is important, but reliable Mn EXAFS data can be generated by this method (Fig. 3.3).

Such extended-range EXAFS measurements allow in case of Mn spectra for a significantly higher distance resolution as can be seen in Fig. 3.4. In comparison to other approaches like [Yano et al., 2005b; Pushkar et al., 2007] to increase the energy range of EXAFS, the method described above is based purely on data evaluation and requires no modifications of the experimental setup aside from setting the discriminator windows to the fluorescence of the two elements.

A value of $E_0 = 6547.0$ eV was used for transformation to k -scale where the spectra were weighted with k^3 . For data modeling, the k -values from 1.2 to 16.6 \AA^{-1} were considered. Furthermore, an amplitude reduction factor, $S_0^2 = 0.85$, was used. The

3. Improved distance resolution by extended-range EXAFS

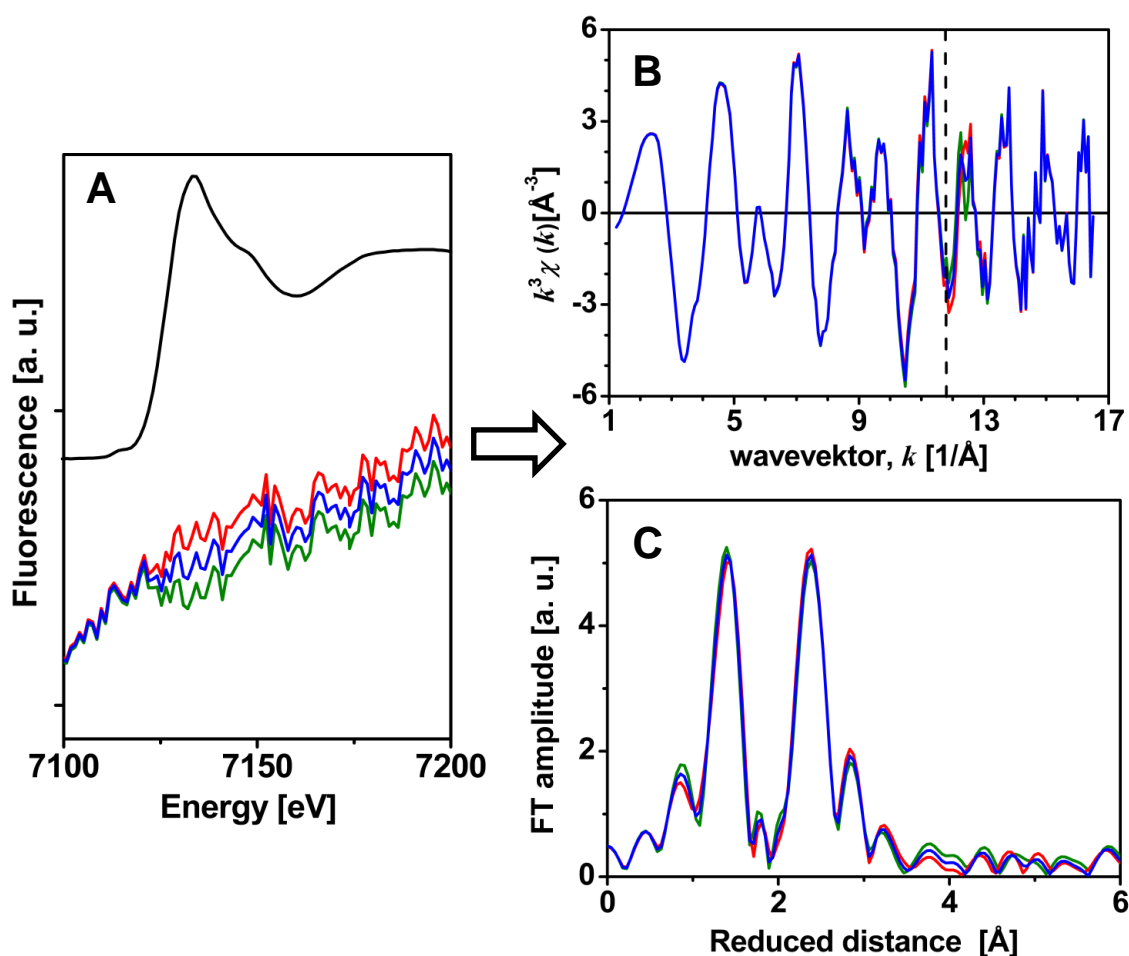


Figure 3.3.:

Effect of different factors for subtraction of the Fe spectrum on the resulting EXAFS spectrum. *Red line:* Factor too small. *Blue line:* Optimal factor. *Green line:* Factor too large. **A:** Spectrum around Fe K-edge. *Black line:* Fe spectrum (plus constant). **B:** Spectrum in k domain. The approximate position of the Fe K-Edge is marked by a dashed line. **C:** Fourier-transformed spectra for extended-range EXAFS of PSII ($0.9\text{--}16.6 \text{\AA}^{-1}$). A fractional cos-window function was applied with ramps extending at the low and high k -sides over 20% of the data. There are only small variations in the FT if a close to optimal subtraction of the Fe-edge is employed. Thus, reliable Mn EXAFS data can be obtained by a relative simple subtraction of the Fe K-edge. Extended-range XAS is feasible using a “conventional” BioXAS setup.

functions $f(k)$, $\delta(k)$, and $\lambda(k)$ needed for this curve-fitting process (compare Section 1.2.2) were calculated using FEFF [Mustre de Leon et al., 1991; Rehr and Albers, 2000; Ankudinov and Rehr, 2003].

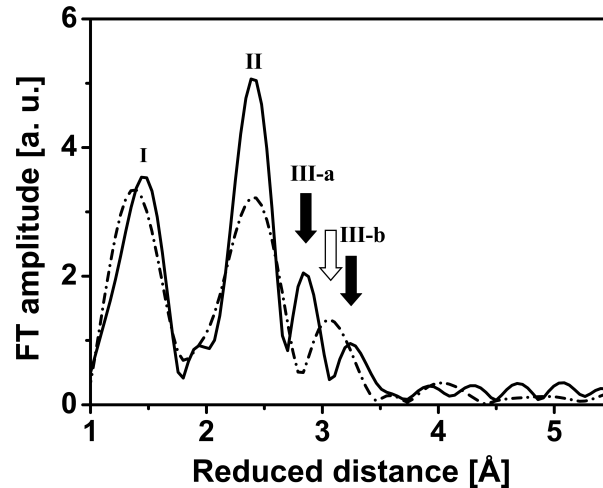


Figure 3.4.:

Fourier-transformed spectra for conventional ($4.1\text{--}11.8\text{ \AA}^{-1}$, dashed line) and extended-range ($4.1\text{--}16.6\text{ \AA}^{-1}$, solid line) EXAFS of PSII. Peak III (open arrow) of the conventional EXAFS spectrum splits into two peaks III-a and III-b (filled arrows) in the extended-range EXAFS spectrum. These peaks correspond to Mn-backscatterer distances of approximately 3.3 \AA and 3.7 \AA . For calculation of the shown Fourier transforms, a fractional cos-window function was used with ramps extending at the low k -side over 10% and at the high k -side over 20% of the data. Figure adapted from Dau et al. [2008].

3.4. Results

As can be seen in Fig. 3.4, the extended energy range ($4.1\text{--}16.6\text{ \AA}^{-1}$) has a distinctively better distance resolution than the conventional range ($4.1\text{--}11.8\text{ \AA}^{-1}$): Peak III at a reduced distance of approximately 3 \AA splits into two peaks at 2.85 \AA (peak III-a) and 3.3 \AA (III-b) of reduced distance. This suggests the presence of backscatterer distances of roughly 3.3 \AA and 3.7 \AA . Additionally, peak II, which is mainly due to Mn-Mn vectors of roughly 2.7 \AA , becomes narrower but increases in height. In other extended-range EXAFS measurements, peak III-a was also found at lower R values, but peak III-b remained below the noise level [Yano et al., 2005b; Pushkar et al., 2007].

3. Improved distance resolution by extended-range EXAFS

The curve fitting (for results see Table 3.1) was performed in k space with a k^3 -weighted version of the measured EXAFS spectrum using the in-house software *SimX* presented in the PhD thesis of Dittmer [1999]. The peak III-b could only be simulated if atoms at 3.7 Å distance were assumed to be present. This suggests a Mn-Ca/Mn vector of this length (compare [MacLachlan et al., 1992]). Because EXAFS measurements at the Ca- or Sr-edge (substituting Ca) do not indicate a 3.7 Å Mn-Ca vector [Cinco et al., 2002, 2004; Müller et al., 2005], the existence of a Mn-Mn vector of this length seems to be more likely. Alternatively, several light backscatterers (5–20 Mn-O/N vectors) at this distance as suggested [Pospíšil et al., 2003; Haumann et al., 2005] could be assumed, but this would be in stark conflict to all recently published models and is therefore highly unrealistic.

The coordination number N is approximately one for the 2.7 Å distance corresponding to two Mn-Mn vectors per Mn_4Ca complex. Adding a third Mn-Mn vector of a length between 2.77–2.97 Å results in very small coordination numbers (< 0.15 , often < 0.08) for this additional shell. The data are therefore incompatible with three short

Table 3.1.:

Parameters obtained by curve fitting of the extended-range EXAFS data. The first column indicates the backscatter for the respective shell. Numbers set in italics were kept constant during the fit process. Fit I and II were presented in Dau et al. [2008] (Table 1). The results were used for modeling the in Dau et al. [2008] proposed structure of the OEC (see Section 2.4.3). Fit III reflects another fit possibility with a single shell for each Mn/Ca-backscatterer. The absorber-backscatterer distances R from this fit were partly used for the HyperChem restraints in Step 1 of the in Section 4.4 described optimization process for new models.

	Fit I			Fit II			Fit III		
	N [1]	R [Å]	σ [Å]	N [1]	R [Å]	σ [Å]	N [1]	R [Å]	σ [Å]
O	<i>3.0</i>	1.85	0.07	<i>3.0</i>	1.85	0.07	<i>2.5</i>	1.83	0.07
O	<i>2.75</i>	2.06	0.13	<i>2.75</i>	2.06	0.13	<i>3.25</i>	1.96	0.13
Mn	1.04	2.72	0.03	1.02	2.72	0.03	<i>0.5</i>	2.70	<i>0.032</i>
Mn	<i>0.5</i>	3.25	0.03	<i>1.0</i>	3.27	0.05	<i>0.5</i>	2.71	<i>0.032</i>
Mn	-	-	-	-	-	-	<i>0.5</i>	3.00	<i>0.032</i>
Mn	-	-	-	-	-	-	<i>0.5</i>	3.14	<i>0.032</i>
Ca	<i>0.5</i>	3.29	0.06	<i>0.5</i>	3.36	0.07	<i>0.25</i>	3.26	<i>0.032</i>
Ca	-	-	-	-	-	-	<i>0.25</i>	3.33	<i>0.032</i>
Ca	-	-	-	-	-	-	<i>0.25</i>	3.33	<i>0.032</i>
Mn	<i>0.5</i>	3.71	0.06	<i>0.5</i>	3.71	0.06	<i>0.5</i>	3.68	<i>0.032</i>
Ca	-	-	-	-	-	-	<i>0.25</i>	3.87	<i>0.032</i>

Mn-Mn vectors ($< 2.9 \text{ \AA}$) as suggested by Yano et al. [2005b] and Pushkar et al. [2007]. Possible reasons for the different results have been discussed in Dau et al. [2004].

The fit results were used as restraints when utilizing geometry optimization via HyperChem for construction of the models presented in Dau et al. [2008] (fit I and II) as well as Grundmeier and Dau [2012] (fit III). For a more detailed explanation, see Section 2.4.3 and Section 4.4.

3.5. Summary

In this chapter, extended-range EXAFS data measured (using a simple approach as described by Gu et al. [2003]) on PSII membrane particles were presented. Hereby, a significantly better distance resolution than with conventional EXAFS (up to the Fe K-edge) could be achieved. For the first time the region around 3 \AA was clearly better resolved (compare Fig. 3.4), splitting the the third main FT peak and suggesting Mn-Mn/Ca distances of both 3.3 \AA and 3.7 \AA . In the following chapter, these experimental results will be used to evaluate and optimize models of the manganese complex of PSII.

4. Modeling the Mn complex

In this chapter, the method used for evaluating alternative models of the manganese complex is described. For given models of the Mn complex, EXAFS spectra were calculated using FEFF and equations derived by Dittmer and Dau [1998]. The difference to experimental data was then reduced by modifying these models applying a Levenberg-Marquardt algorithm (*levmar*, [Lourakis, 2004]) utilized by a self-written program (for a description of this program, see Appendix A.4).

4.1. Experimental data used for model evaluation

Seven spectra belonging to three different types of experimental EXAFS data were used. All spectra were collected for PSII samples at the K-edge of manganese:

Isotropic extended-range EXAFS (Iso). The extended-range EXAFS spectrum presented in Dau et al. [2008] was used. As described in detail in Chapter 3, the data were collected for curves ranging up to 1050 eV above the K-edge (16.6 \AA^{-1}) using PSII membrane particles. To obtain an isotropic spectrum, measurements were performed at an angle of roughly 55° (“magic angle”, Section 1.2.4) between the normal of the sample substrate and the electric field vector E of the incoming X-ray beam.

Polarized EXAFS of unidirectionally oriented membrane particles (Mem). This data set consist of three EXAFS spectra in the range up to 510 eV (11.6 \AA^{-1}) above the K-edge measured at angles of 15° , 35° , and 75° between the sample normal and the E -field vector of the X-ray beam. (For 55° the extended EXAFS spectrum as described above was used.) To get a better signal-to-noise ratio, spectra from Schiller et al. [1998] and Haumann et al. [2001] were averaged. (The theory behind this angle dependence is described in Chapter 1.2.4, for more information regarding the samples see Section 3.1.2.)

Polarized EXAFS of PSII crystals (Cry). The third set of experimental data consists of three EXAFS spectra published in Yano et al. [2006] as Fourier transforms. Yano, Yachandra and coworkers measured EXAFS spectra for single crystals of dimeric PSII with the electric field vector E parallel to one of the three unit-cell vectors (a, b, and c). (For a summary of the article Yano et al. [2006], see Section 2.4.1.)

4. Modeling the Mn complex

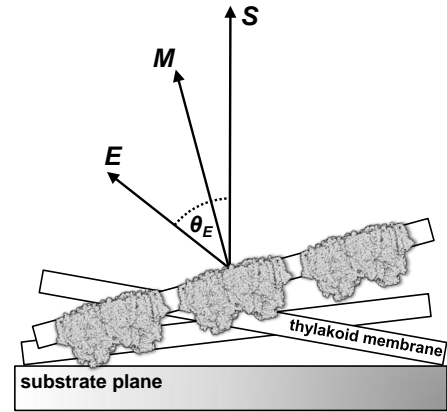
4.2. Calculation of EXAFS spectra

The EXAFS spectra were calculated in k space using the equations from Dittmer and Dau [1998]. In the following, this procedure is described in detail:

The EXAFS spectrum, χ , of a model can be given as a function of k and the angle θ_E . Here, θ_E is the angle between the X-ray electric field vector E and either the sample normal S for oriented membrane particles (Fig. 4.1) or one of the unit cell vectors (a , b , or c) for single-crystal EXAFS (Fig. 2.6). In latter case, the E -field vector is parallel to one of the vectors a , b , c and therefore $\theta_E = 0$ in this case.

Figure 4.1.:

Sketch of partially oriented PSII sample with illustration of important variables. Substrate plane (gray rectangle) and exemplary thylakoid membranes sheets (white) are shown. For one of the membrane sheets, PSII dimers and the corresponding membrane normal M are depicted. The vector S (sample normal) is the normal of the substrate plane. The variable E is the electric field vector of the incoming X-ray beam. For measurements and calculations of spectra, the angle θ_E between S and E was varied. Figure from Grundmeier and Dau [2012].



The function χ can be written as the sum of m EXAFS spectra χ_i , one spectrum for each “shell”:

$$\chi(k, \theta_E) = \sum_{i=1}^m \chi_i(k, \theta_E) \quad (4.1)$$

Here, one “shell” consists of one manganese-backscatterer vector with each of these m spectra given by the following equation:

$$\chi_i(k, \theta_E) = \frac{1}{3}N_i \left[(\chi_i^c(k) + 2\chi_i^s(k)) + \frac{1}{2}(\chi_i^c(k) - \chi_i^s(k))(3 \cos^2 \theta_E - 1)(3 \cos^2 \theta_{R,i} - 1)I_{\text{ord}} \right] \quad (4.2)$$

In this equation, the angle $\theta_{R,i}$ is the angle between the absorber-backscatterer vector of shell i and either the membrane normal M (Fig. 4.1) or one specific crystal axis (a , b , or c , Fig. 2.6). The constant I_{ord} is the order parameter (see Section 1.2.4).

The factor N_i is the coordination number divided by the number of absorbing atoms for the i^{th} shell. Due to the four Mn atoms per manganese complex, this value equals 0.5 in the case of manganese as an backscatterer (a Mn-Mn vector has to be counted twice) and 0.25 else.

4.2. Calculation of EXAFS spectra

The functions χ_i^c and χ_i^s are defined as follows:¹

$$\chi_i^c(k) = \frac{S_0^2}{kR_i^2} e^{-2\sigma_i^2 k^2 - \frac{2R_i}{\lambda_i^c(k)}} f_i^c(k) \sin[2kR_i + \phi_i^c(k) + 2\delta_i^c(k)] \quad (4.3a)$$

and

$$\chi_i^s(k) = \frac{S_0^2}{kR_i^2} e^{-2\sigma_i^2 k^2 - \frac{2R_i}{\lambda_i^s(k)}} f_i^s(k) \sin[2kR_i + \phi_i^s(k) + 2\delta_i^s(k)] \quad (4.3b)$$

Here, R_i is the absorber-backscatterer distance, σ_i is the Debye-Waller parameter, and S_0^2 the amplitude reduction factor. The program FEFF 8.4 [Mustre de Leon et al., 1991; Rehr and Albers, 2000; Ankudinov and Rehr, 2003] was used for ab-initio calculation of the phase and amplitude functions (more precisely $\lambda_i^{c/s}$, $f_i^{c/s}$, $\phi_i^{c/s}$, $\delta_i^{c/s}$). For this, a structural model close to the discussed models was used. (For details on the calculation process of the phase/amplitude functions see Appendix A.2.) It was verified that multiple-scattering contributions to the EXAFS were small and that their neglect could not affect the conclusions.

All spectra were calculated using an S_0^2 -value of 0.85 and a σ_i^2 value of 0.001 \AA^2 for all shells. The order parameter I_{ord} was set to 1 in case of crystals and near to 0.5 (exact value used: 0.468) for partially oriented membrane particles, as has been determined in previous EPR experiments [Schiller et al., 1998]. A weighting by k^3 was applied to all spectra.

The EXAFS Fourier transforms for the *Mem* and *Iso* spectra were calculated for k -values ranging from 3.5 to 11.5 \AA^{-1} using a fractional cosine window, which ramps spanned 10.0% of the data at low k -values and 10% at high k -values. For the *Cry* spectra, a fractional cosine window from 3.0 to 12.0 \AA^{-1} with 11.1% ramps was used as within the articles Yano et al. [2006] and Sproviero et al. [2008b].²

Further, different ΔE_0 values were chosen for the *Mem/Iso* and the *Cry* case for shifting of the calculated spectra to account for vastly different E_0 values used when

¹Erroneously, in the article Grundmeier and Dau [2012] a cosine instead of a sine function was printed for $\chi_i^c(k)$. Though this does only add an additional constant phase shift, it is important to use the correct formula when having calculated $\phi_i^c(k) + 2\delta_i^c(k)$ with, e. g., FEFF (see Appendix A.2).

²Yano and coworkers as well as Sproviero and coworkers used this type of window for their articles Yano et al. [2006] and Sproviero et al. [2008b]. In more detail, the IFEFFIT command `fft` was applied with the parameters $k_{\text{min}} = 3.5 \text{ \AA}^{-1}$, $k_{\text{max}} = 11.5 \text{ \AA}^{-1}$ and $\Delta k = 1 \text{ \AA}^{-1}$ [Sproviero, Yano, pers. comm.]. Here, the variables k_{min} and k_{max} denote the center positions of the two slopes and Δk equals the width of these slopes [Newville, 2004]. This translates to a window function from $k_{\text{min}} - \Delta k/2 = 3.0 \text{ \AA}^{-1}$ to $k_{\text{max}} + \Delta k/2 = 12.0 \text{ \AA}^{-1}$ with the two ramps spanning both $\Delta k / (12.0 \text{ \AA}^{-1} - 3.0 \text{ \AA}^{-1}) \approx 11.1\%$ of the data each.

For reasons of simplification, in the article Grundmeier and Dau [2012] only a $3.5 \text{ \AA}^{-1}/11.5 \text{ \AA}^{-1}/10.0\%$ window is mentioned. Although the resulting differences in the FT spectra are small, they are still visible.

4. Modeling the Mn complex

evaluating the experimental data ($E_0 = 6547.0$ eV for *Mem/Iso*, $E_0 = 6561.3$ eV for *Cry* [Yano, pers. comm.]).

Due to the fact that for shells with backscatterers of the same element and at exactly the same distance varying only in the value of $\theta_{R,i}$, the functions χ_i^c and χ_i^s are identical, the number m of spectra χ_i to be calculated (and therefore also the computer power needed for calculation of χ) can be reduced by defining an average angle $\bar{\theta}_{R,i}$:

$$\cos^2 \bar{\theta}_R := \frac{1}{N} \sum_{i=1}^N \cos^2 \theta_{R,i} \quad (4.4)$$

Here, N is the number of angles $\theta_{R,i}$ that are averaged (which equals the number of equivalent shells). Using this definition, Eqs. (4.1) and (4.2) can be rewritten as

$$\chi(k, \theta_E) = \sum_{i=1}^n \chi_i(k, \theta_E) \quad (4.5)$$

and

$$\begin{aligned} \chi_i(k, \theta_E) = & \frac{1}{3} N_i [(\chi_i^c(k) + 2\chi_i^s(k)) + \\ & + \frac{1}{2} (\chi_i^c(k) - \chi_i^s(k)) (3 \cos^2 \theta_E - 1) (3 \cos^2 \bar{\theta}_{R,i} - 1) I_{\text{ord}}] \end{aligned} \quad (4.6)$$

with $n \leq m$ shells and angles $\bar{\theta}_{R,i}$ given by the average value of N_i angles.

The two Mn complexes of one PSII dimer have the same orientation to the membrane normal. Therefore, for calculating spectra for the case of partial oriented (or isotropic) samples, one shell consists only of one absorber-backscatter combination. Consequently, no angles have to be averaged ($N_i = 1$ for all i). In case of PSII crystals, the average angle for one whole unit cell consisting of four PSII dimers (see Fig. 2.6) has to be taken into account. Due to the $P2_12_12_1$ symmetry of PSII (see Appendix A.1), the average angle can be calculated averaging the angles for only one dimer (two Mn complexes, therefore $N_i = 2$ for all i).

All four manganese atoms of the OEC had to be taken into account as absorbers, as backscatterers O, N, C, Mn and Ca atoms were used. Because each individual absorber-backscatterer combination with the average angle given by equation (4.4) is treated as a single shell, the n -value in Eq. (4.5) is very high (e. g., 326 shells for 84 atoms, in simulation of model C-II).

The method described above for calculation of EXAFS spectra is different from the one used by Yano et al. [2006] and Sproviero et al. [2008b], who use solely the FEFF program for calculation of spectra. However, the calculations result in very similar spectra. Advantages of the approach described above, are:

- Clearly smaller computational costs.
- The possibility to treat correctly the spectra collected on partially oriented PSII membrane particles.

4.3. Considered models of the OEC

EXAFS spectra were calculated for the following OEC models:

Models of Yano et al. (A-I, A-II, A-IIa, A-III) The coordinates for the four models A-I to A-III were taken from the supporting material of the article Yano et al. [2006] (named I, II, IIa, III in Yano et al. [2006]; Fig. 2.9).

Models of Sproviero et al. (B-I, B-II) The coordinates for model B-I were taken from the supporting material of Sproviero et al. [2008b] (equals model DFT-QM/MM in Sproviero et al. [2008b]). For the model B-II (equals R-QM/MM from Sproviero et al. [2008b]) coordinates were used that had been personally communicated. These coordinates are slightly different from the coordinates given in the supporting material of Sproviero et al. [2008b] (Fig. 2.2).

Model of Dau et al. (C-I) The coordinates of the model C-I were obtained as described in the following section using only the *Iso* data set. This model is essentially identical to the model in Dau et al. [2008] (Chapter 2.4.3; Fig. 2.3).

Modifications of model of Dau et al. (C-II, C-III, C-IV, D, F) The models C-II to C-IV, D, and F were constructed as described in the following section using all three data sets (*Iso*, *Mem*, *Cry*). They are based on different structural concepts, but are (like model C-I) based on the XRD data from Loll et al. [2005]. Here, model C-II is an optimization of model C-I, taking all EXAFS spectra into account but preserving the overall idea (Figs. 2.3 and 5.5).

Models of Umena et al. (E-A, E-B) The coordinates for these models were taken from the crystallographic data 3ARC published by Umena et al. [2011] where E-A and E-B refer to the two Mn complexes of the PSII dimer and their surrounding amino acids. Here, the names E-A and E-B correspond to monomers A and B from the supplementary information of Umena et al. [2011] (Fig. 2.5).

4.4. Optimization of structural models

A series of (new) models named C-I, C-II, C-III, C-IV, D, and F was created as variants of the model proposed in Dau et al. [2008] (which is largely equivalent to model C-I). Starting from the crystallographic data of Loll et al. [2005], for all six models the following steps were implemented:

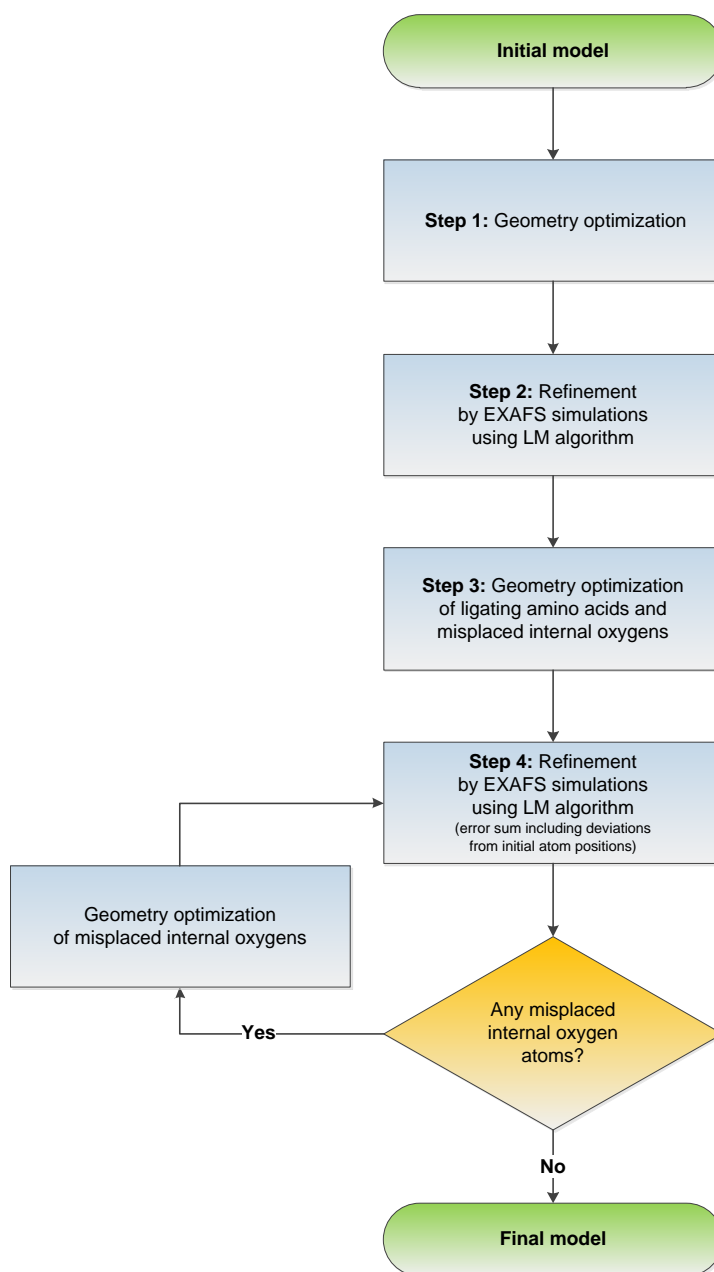
Step 1 – Molecular mechanics modeling with restraints

This first step is similar to the procedure described in Dau et al. [2008]. The crystallographic results from Loll et al. [2005] were refined using molecular mechanics

4. Modeling the Mn complex

Figure 4.2.:

Flow chart showing steps used for optimization of models. For each model, at first a geometry optimization using HyperChem is applied (Step 1), then the model is refined by EXAFS simulations to reach a better agreement with experimental data (using a Levenberg-Marquardt algorithm, Step 2). Finally, the positions of ligating amino acids and possibly misplaced atoms are corrected by renewed geometry optimization and EXAFS calculations (Step 3 and 4). For a detailed description of the optimization process, see text.



4.4. Optimization of structural models

simulations (using HyperChem 6, Hypercube, with a MM+ force field and steepest descent algorithm).

Strong restraints for all Mn-Mn distances (with exception of the long Mn²-Mn⁴ distance), for the Mn-ligand distances of the first coordination sphere (Mn-O/N) and for selected bond angles of the Mn atoms were used. The chosen Mn-Mn and Mn-Ca distances were mostly based on EXAFS fit results (fit III in Table 3.1) for the isotropic spectrum from Dau et al. [2008] (equals *Iso* data set), whereas the Mn-O/N bond lengths and the bond angles were restrained to chemically reasonable values. All in all, six specific combinations of metal-metal distances were used for the assignment of the fit results to the metal-metal distances, resulting in the models C-I, C-II, C-III, C-IV, D, and F.

For the geometry optimization, only movement of atoms in spheres of about 5.5 Å around Mn¹, Mn², and Mn³ and of 6.5 Å around Mn⁴ were allowed. Here, the sphere around Mn⁴ was chosen larger to account for the influence of the assumed severe radiation damage in this region [Loll et al., 2005]. The positions of all atoms outside of these four spheres were kept constant (fixed to the values of the crystallographic coordinates of Loll et al. [2005]).

Step 2 – Refined models by EXAFS simulations

This refinement aims at the optimization of the Mn-Mn and Mn-Ca distances of the model. For this, the agreement between calculated and experimental EXAFS spectra was maximized. Except for model C-I, all three types of EXAFS data described in Section 4.1 were used, namely the isotropic extended-range spectrum (*Iso*), the polarized EXAFS collected on PSII membrane particles (*Mem*), and the polarized EXAFS collected on PSII crystals (*Cry*). For model C-I, only the *Iso* spectrum was used, in line with the modeling approach of Dau et al. [2008].

The spectra were calculated using Eqs. (4.5) and (4.6) as described in Section 4.2. Here, all non-hydrogen atoms with a maximal distance of 6.5 Å to the Mn atoms were considered as backscatterers, resulting in around 80 atoms.

To optimize the structure, that is, the atom coordinates, an error ε was calculated and minimized using the Levenberg-Marquardt (LM) algorithm *levmar* [Lourakis, 2004], implemented in a self-written program (see Appendix A.4 for details). This error consisted of two parts: Firstly, the differences between experimental and simulated spectra (least-square error), and secondly, a term implementing chosen restraints regarding atom-atom distances.

In more detail, for a spectrum an error sum was calculated by summing up the squared differences between experimental and simulated spectra. For the partial oriented and isotropic spectra (*Mem* and *Iso* data sets), the error sums ε_{Mem} and ε_{Iso} , respectively, were calculated directly in k -space. In contrast, for crystal spectra (*Cry*), the Fourier transforms of the simulated EXAFS spectra were calculated and compared to the experimental FT-amplitude spectra published in Yano et al. [2006] to generate

4. Modeling the Mn complex

the corresponding error ε_{Cry} . For this comparison, only the region between 1.1 and 3.2 Å of reduced distance was considered (equals roughly first to third main peak).

Further, weak restraints for the length of internal Mn-O bonds were used. To preserve the structural idea of the model during the fit process, a strong additional restraint was applied to the single 2.45 Å Mn-O distance (either Mn¹-O^a or Mn¹-O^d) of the Mn complex. Finally, more strong restraints were used for all short C-C, C-O, and C-N distances (≤ 2.5 Å) to maintain the structures of the ligating amino acids. For terminal oxygens and Mn-Mn/Ca distances, no restraints were applied. All the distance restraints were implemented as an additional error sum ε_{Res} of weighted squared deviations from the wanted distances.

Using all calculated error sums, the final joint error ε for the models C-II, C-III, C-IV, D, and F was calculated by adding up all error sums weighting ε_{Cry} with an empirical factor c . In case of model C-I, the error ε was given only by the difference of the calculated 55° spectrum to the *Iso* data set plus restraints. Therefore, the restraints had to be weighted weaker (i. e., ε_{Res} multiplied with an additional factor $d < 1$) to keep the ratio of spectra and restraints the same for both cases. Summarized, the joint error used is described by the following formula:

$$\varepsilon_{\text{all}} = \begin{cases} \varepsilon_{\text{Iso}} + d \cdot \varepsilon_{\text{Res}} & \text{for model C-I} \\ \varepsilon_{\text{Mem}} + \varepsilon_{\text{Iso}} + c \cdot \varepsilon_{\text{Cry}} + \varepsilon_{\text{Res}} & \text{for models C-II, C-III, C-IV, and D} \end{cases} \quad (4.7)$$

For this optimization process, the coordinates of all atoms with a distance greater than 5 Å to their nearest Mn atom were held constant resulting in around 50 movable atoms.

Step 3 – Corrections in the molecular mechanics framework

This step optimizes the coordinates of ligating amino acids as well as internal oxygen atoms misplaced in Step 1. Despite the fact that the LM algorithm does not affect the coordinates of the outer atoms as much as the more central ones (shorter absorber-backscatter distances), normally the positions of all movable atoms are changed notably. Due to this, some of the the ligating amino acids partly were moved to chemically impossible positions. Additionally, the same problem could occur for internal bridging oxygen atoms. Therefore, renewed geometry optimizations using HyperChem (MM+ force field and steepest descent algorithm as in Step 1) were applied to all ligating amino acids as well as obviously misplaced internal bridging oxygens.

Step 4 – Further refinement of model

The movement of the light backscatterers in Step 3 normally changes strongly the calculated EXAFS spectra. Especially, the first FT peak is affected drastically, but also the second peak is modified visibly. To correct for this, the LM algorithm from

4.4. Optimization of structural models

Step 2 was used again. In comparison to Step 2 the squared differences between the starting and current position of the atoms was added to the error sum (4.7), here denoted as ε_{pos} , and weighted using a factor e :

$$\varepsilon'_{\text{all}} = \varepsilon_{\text{all}} + e \cdot \varepsilon_{\text{pos}} \quad (4.8)$$

Due to ε_{pos} , the atoms are moved only slightly by the LM algorithm (average movement of atoms during this fit process was typically in the region of 0.07 \AA) and therefore the structure generated by the previous steps was mostly preserved. In the case of renewed misplaced internal oxygen atoms (unrealistic Mn-O distances), a new geometry optimization was performed for these misplaced atoms (see Step 3) before repeating Step 4.

5. Evaluation of OEC models

In this chapter, OEC models based on the method described in Chapter 4 are evaluated and compared to recently proposed models [Yano et al., 2006; Sproviero et al., 2008b; Umena et al., 2011]. The models are judged based on the agreement of simulated to experimental data using all seven spectra listed in Section 4.1.

For the following considerations, it is required that structure and orientation of the OEC are identical in the cyanobacterial (*Cry* data) and plant PSII (*Mem* data). Otherwise, these two data sets could not be used in combination. X-ray absorption spectroscopy [McDermott et al., 1988; Yachandra et al., 1993] as well as EPR measurements [Aasa et al., 1989; McDermott et al., 1988] on *Synechococcus* and spinach indicate that in fact both system are remarkably similar.

5.1. Calculation and evaluation of spectra

As described in Section 4.1, seven spectra were used to analyze existing models of the OEC and develop new ones: One isotropic extended EXAFS spectrum at 55° (*Iso*), three spectra collected on unidirectionally oriented PSII membrane particles at 15° , 35° , and 75° (*Mem*), and three spectra measured with single crystals of PSII for all three crystal axes (*Cry*). Tables 5.1 and 5.2, important structural parameters of the models are listed, namely the metal-metal distances and the angles between these vectors and the membrane normal. Additionally, an error value, $\varepsilon_{\text{Spectra}}$, calculated via

$$\varepsilon_{\text{Spectra}} := \varepsilon_{\text{Mem}} + \varepsilon_{\text{Iso}} + c \cdot \varepsilon_{\text{Cry}} \quad (5.1)$$

is displayed (compare Eq. (4.7) and Section 4.4 for explanation of the used variables). It reflects the difference between the calculated spectra and the experimental *Iso*, *Mem*, and *Cry* data sets described in Section 4.1.

For evaluation of the models presented in Yano et al. [2006] and Sproviero et al. [2008b] as well as the models developed using the procedure from Section 4.4, the second main FT peak is of high interest. It is mainly originating from di- μ -oxo bridged pairs of Mn atoms with distances typically around 2.7 Å. The exact length of these di- μ -oxo bridges and especially their orientation towards the membrane normal is an important characteristic of the respective OEC model. Therefore, the peak height of the second peak and its dependence on the measurement angle is a feature of the EXAFS data comparable to a “fingerprint” of the discussed Mn complex. Additionally, this peak is typically clearly above noise level and therefore eases the comparison

5. Evaluation of OEC models

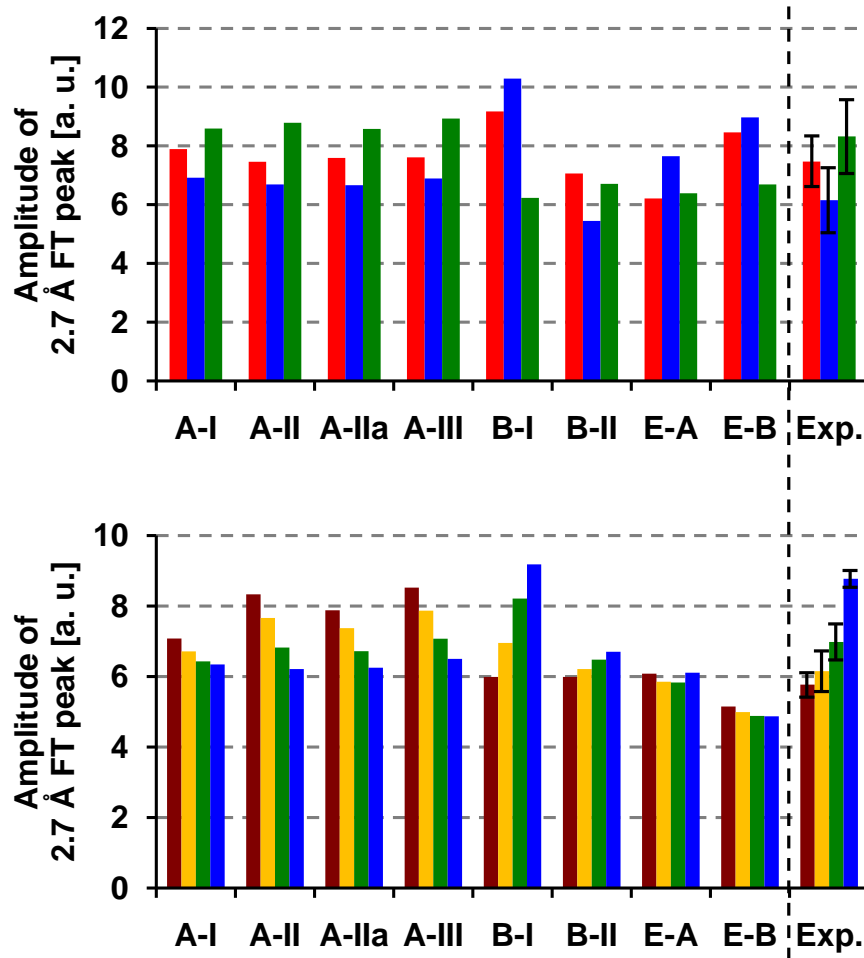


Figure 5.1.:

Bar diagrams showing the height of the second FT peak (at $\sim 2.7 \text{ \AA}$) for the calculated EXAFS spectra for models A-I, A-II, A-IIa, and A-III of Yano et al. [2006] as well as B-I, B-II of Sproviero et al. [2008b] and the XRD data of Umena et al. [2011] (both monomers E-A and E-B) in comparison to the experimental results. The upper bar diagram displays the results for polarized EXAFS spectra of PSII crystals (*Cry* data), the lower relates to the case of polarized EXAFS on partially oriented samples (*Mem* and *Iso* data). The color coding for this and following figures showing bar diagrams or spectra (excluding Fig. 5.2) is for *Cry* data: Electric-field vector of the X-ray beam parallel to crystal axis *a*: red, *b*: blue, *c*: green. For *Mem* and *Iso* data: Angle between Electric-field vector and sample normal 15° : red, 35° : yellow, 55° : green, 75° : blue. The error bars for the experimental data are 2σ -errors calculated of the FT data in the region between 5.5 and 8 \AA of reduced distance. *Remarks:* The error for the experimental 75° -spectrum of the *Mem* data is probably greater than the displayed error bar. Figure from Grundmeier and Dau [2012].

between simulation and experiment. In Fig. 5.1 a bar diagram is shown, comparing the heights of this important second FT peak for the examined models.

5.2. Models A-I, A-II, A-IIa, and A-III

As described in Section 2.4.1, Yano et al. proposed four models A-I, A-II, A-IIa, and A-III (Fig. 2.9) in Yano et al. [2006] (there plainly named I, II, IIa, and III), for which the calculated EXAFS spectra reproduce the polarized EXAFS data obtained for PSII crystals (*Cry* data).

The four models of Yano et al. were optimized (Yano et al.) to match the experimental EXAFS data gained from PSII crystals (*Cry*). Therefore, the good agreement shown in Fig. 5.1 between calculated and experimental data is expected.

It should be mentioned that the calculated spectra for the models A-I, A-II, A-IIa, and A-III presented in Yano et al. [2006] match even better with the experimental data than the spectra for these models calculated for this thesis (and Grundmeier and Dau [2012]). This is due to two things: Firstly, the differences in methods for calculation of the spectra (compare Section 2.4.1 and 4.2). Secondly, Yano and coworkers used a Debye-Waller factor of $\sigma_i^2 = 0.002 \text{ \AA}^2$ [Yano, pers. comm.], where for this work $\sigma_i^2 = 0.001 \text{ \AA}^2$ was used.

However, the models of Yano et al. contradict the experimental EXAFS spectra of PSII membrane particles (*Mem* data): As can be seen in Fig. 5.1, the height of the second peak should increase with increasing angle θ_E between membrane normal and *E*-field vector. This is not the case for the simulated spectra. Thus, the models of Yano et al. can be ruled out.

Additionally, there could be other issues with the models of Yano et al.:

- They are hard to reconcile with the experimental XRD data. It is unclear, how the amino acids are bound to the Mn complex, though in Yano et al. [2006] suggestions are made.
- The models were optimized without taking into any specific ligand environment of ligating amino acid residues (only the internal bridging oxygens plus manganese and calcium atoms). This could lead to a significant change of the EXAFS spectra when actually inserting the model structures into a PSII dimer in a chemically reasonable way.

5.3. Models B-I and B-II

Sproviero and coworkers used QM/MM and DFT calculations to create a model (DFT-QM/MM, in this thesis named B-I; Fig. 2.2) based on the 3.5 Å-resolution XRD data from Ferreira et al. [2004], which he later refined by using EXAFS data collected on

5. Evaluation of OEC models

Table 5.1.:

Mn-Mn/Ca distances (R) and angles (θ_R) between Mn-Mn/Ca vectors and membrane normal for models A-I to A-III from Yano et al. [2006], B-I (DFT-QM/MM) and B-II (R-QM/MM) from Sproviero et al. [2008b], and both monomers E-A and E-B of the XRD data from Umena et al. [2011]. Short Mn-Mn vectors are emphasized by bold printing. The error ($\epsilon_{\text{Spectra}}$; see Eq. (5.1), in arbitrary units) is shown in the last row, reflecting the difference between the calculated spectra and the experimental *Iso*, *Mem*, and *Cry* data sets described in Section 4.1 for the respective model. Table adapted from Grundmeier and Dau [2012].

	A-I		A-II		A-IIa		A-III		B-I		B-II		E-A		E-B	
atom pair	R [Å]	θ_R [°]	R [Å]	θ_R [°]	R [Å]	θ_R [°]	R [Å]	θ_R [°]	R [Å]	θ_R [°]	R [Å]	θ_R [°]	R [Å]	θ_R [°]	R [Å]	θ_R [°]
Mn ¹ -Mn ²	2.81	86	2.80	57	2.80	60	2.80	63	2.76	60	2.74	58	2.84	74	2.76	74
Mn ¹ -Mn ³	2.70	23	2.70	50	2.70	46	2.70	47	2.82	65	2.77	68	3.29	86	3.30	87
Mn ¹ -Mn ⁴	4.74	40	4.96	41	4.96	36	4.97	35	3.34	54	3.34	55	5.00	64	4.95	63
Mn ² -Mn ³	3.26	34	3.28	86	3.28	81	3.25	80	2.76	86	2.63	81	2.89	78	2.91	79
Mn ² -Mn ⁴	4.94	38	5.50	66	5.49	61	5.46	59	5.38	52	5.40	52	5.44	56	5.37	56
Mn ³ -Mn ⁴	2.73	65	2.72	42	2.72	38	2.72	35	3.72	33	3.68	37	2.97	35	2.91	33
Mn ¹ -Ca	4.94	58	4.36	6	3.41	29	3.40	27	3.31	50	3.29	50	3.51	45	3.46	45
Mn ² -Ca	3.40	33	3.39	34	3.41	62	3.40	59	3.59	12	3.57	8	3.36	13	3.29	12
Mn ³ -Ca	3.40	88	3.40	40	3.75	73	3.73	71	3.95	33	3.88	36	3.41	38	3.44	40
Mn ⁴ -Ca	5.04	78	3.61	81	4.41	76	4.38	76	3.84	87	4.12	87	3.79	86	3.80	87
Mn-Ca avg.	4.19	60	3.69	41	3.75	58	3.73	56	3.67	44	3.72	44	3.52	44	3.50	44
dist./angle																
$\epsilon_{\text{Spectra}}$	6.5		5.6		5.8		6.6		18.1		5.8		50.2		42.9	

Table 5.2.:

Mn-Mn/Ca distances (R) and angles (θ_R) between Mn-Mn/Ca vectors and membrane normal for models C-I to C-IV, D, and F. The second row shows the Mn-O distance exceeding 2.4 Å belonging to the open coordination site at a (quasi-)five-coordinated Mn^{III} ion. Short Mn-Mn vectors are emphasized by bold printing. The error ($\epsilon_{\text{Spectra}}$; see Eq. (5.1), in arbitrary units) is shown in the last row, reflecting the difference between the calculated spectra and the experimental *Iso*, *Mem*, and *Cry* data sets described in Section 4.1 for the respective model.

	C-I		C-II		C-III		C-IV		D		F	
> 2.4 Å	Mn ¹ -O ^a	θ_R [°]	Mn ¹ -O ^a	θ_R [°]	Mn ¹ -O ^d	θ_R [°]	Mn ¹ -O ^d	θ_R [°]	Mn ³ -O ^d	Mn ¹ -O ^d	θ_R [°]	Mn ¹ -O ^d
atom pair	R [Å]	θ_R [°]	R [Å]	θ_R [°]	R [Å]	θ_R [°]	R [Å]	θ_R [°]	R [Å]	θ_R [°]	R [Å]	θ_R [°]
Mn ¹ -Mn ²	2.99	77	3.07	89	2.73	75	2.73	72	2.72	78	2.71	88
Mn ¹ -Mn ³	3.13	87	3.22	86	3.19	70	3.17	78	3.17	79	3.17	88
Mn ¹ -Mn ⁴	3.72	59	3.70	58	3.72	70	4.33	63	3.70	63	3.72	56
Mn ² -Mn ³	2.69	79	2.75	84	2.71	82	2.70	86	2.71	89	2.69	89
Mn ² -Mn ⁴	4.85	58	4.81	66	4.79	66	5.04	56	4.82	62	4.47	61
Mn ³ -Mn ⁴	2.73	40	2.69	50	3.03	39	3.03	31	3.03	40	2.75	37
Mn ¹ -Ca	3.26	41	3.23	26	3.64	50	3.37	45	3.34	41	3.64	37
Mn ² -Ca	3.26	15	3.38	29	3.34	25	3.27	9	3.26	18	3.06	13
Mn ³ -Ca	3.37	39	3.62	42	3.67	22	3.74	36	3.63	30	3.70	36
Mn ⁴ -Ca	3.38	81	3.44	74	3.39	72	3.72	83	3.37	76	3.34	76
Mn-Ca avg. dist./angle	3.32	43	3.42	42	3.51	42	3.53	43	3.40	41	3.44	41
$\epsilon_{\text{Spectra}}$	5.2		1.4		1.2		1.3		1.3		1.3	

5. Evaluation of OEC models

PSII crystals (equals *Cry* data set) resulting in model R-QM/MM, which corresponds to B-II [Sproviero et al., 2008b] (see Chapter 2.4.2). The heights of the 2.7 Å FT peaks for the calculated EXAFS data are shown in Fig. 5.1.

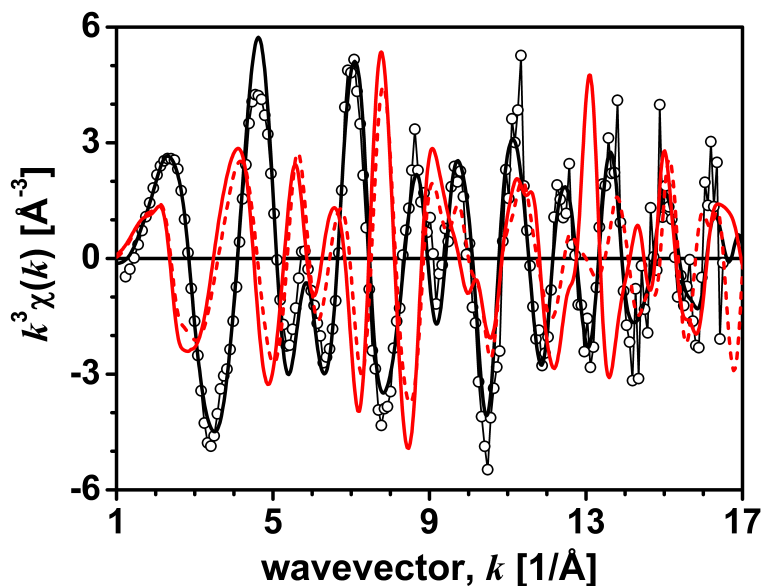


Figure 5.2.:

Comparison of experimental extended-range EXAFS data for isotropic PSII samples in the S_1 -state (*Iso* data; open circles) with calculated spectra for (i) model C-II (black line) and (ii) monomer A (solid red line) and B (dashed red line) from 1.9 Å-structure published in Umena et al. [2011]. The EXAFS data has been weighted by k^3 . The spectra calculated for the individual PSII monomers differ only slightly at lower wavenumbers but more pronouncedly at higher wavenumbers. Both spectra calculated on the basis of the crystallographic coordinates of Umena et al. [2011] are incompatible with the experimental spectrum.

While the model B-I shows a strong linear dichroism for partially oriented samples in the second main peak as can be seen in Fig. 5.1, the calculated spectra contradict the experimental data for the crystal case. In contrast to this, the model B-II is in sufficiently good agreement with both the *Cry* as well as the *Mem/Iso* data sets as also illustrated by the according bar diagrams in Fig. 5.1. While the linear dichroism in case of partially oriented samples is weaker than for model B-I (but still distinct), the calculated peak heights for the crystal case also reproduce the experimental data (when taking into account the error of the experimental spectra).

A serious problem of both models, B-I and B-II, are the ligating amino acids. Their proposed arrangement reflects the XRD results from Ferreira et al. [2004], but contradicts more accurate crystallographic results from Loll et al. [2005] and also more

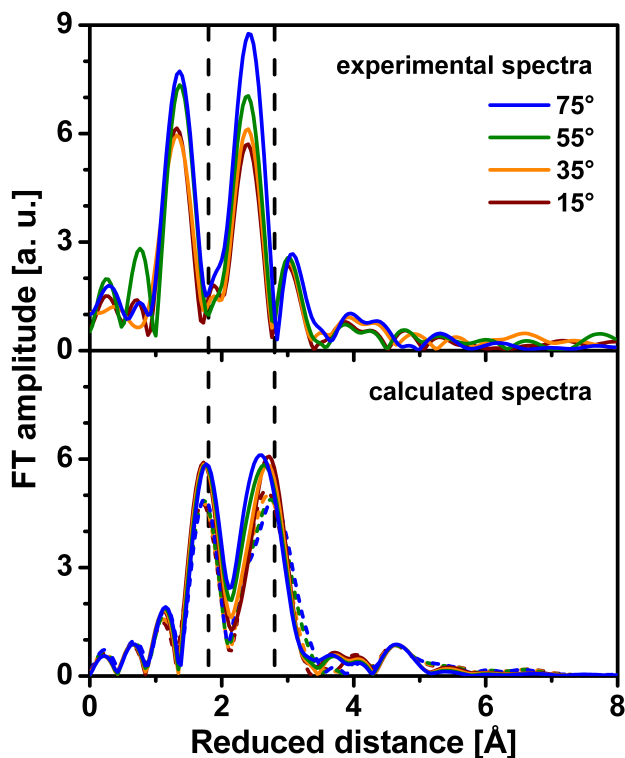


Figure 5.3.:

Fourier transform of polarized EXAFS spectra for partially oriented PSII samples at different excitation angles. *Top:* Experimental results (*Mem* and *Iso* data sets). *Bottom:* Calculated spectra for the 1.9 Å-structure published in Umena et al. [2011]. The results for both monomers A (solid lines) and B (dashed lines) are shown. Beginning and end of distance range covered by the second main peak of the experimental data are marked by dashed lines to stress the different position of this peak in the calculated spectra. Figure from Grundmeier and Dau [2012].

recently [Umena et al., 2011]. As the ligand environment chosen by Sproviero et al. now appears to be unreasonable, the corresponding models can be rejected.

5.4. Models E-A and E-B

As already mentioned in Section 2.2, Shen and coworkers published in 2011 new XRD data (3ARC) of PSII from *Thermosynechococcus vulcanus* with a very high resolution of 1.9 Å [Umena et al., 2011]. The two Mn complexes of this data set and their surrounding amino acids (see Fig. 2.5) are named model E-A and E-B in this thesis. (E-A equals monomer A from the supplementary information of Umena et al. [2011]. Accordingly, E-B equals monomer B.)

The simulated EXAFS spectra for the XRD data of Shen and coworkers are in stark contradiction to the experimental results (compare Figs. 5.1, 5.2, 5.3, and 5.4). This result is to be expected as most Mn-ligand bonds as well as Mn-Mn distances are longer than predicted for the $\text{Mn}_4^{\text{III,III,IV,IV}}$ oxidation state (Mn complex in its S_1 -state; compare Table 5.1 of this thesis and Table 3 of the supplementary information of Umena et al. [2011]). For example, for both monomers of the 3ARC data there exists only one short Mn-Mn distance in the region of roughly 2.7 Å, but at least two are expected from EXAFS results (compare Table 2.1).

Using the bond valence method and bond valence parameters from Brese and

5. Evaluation of OEC models

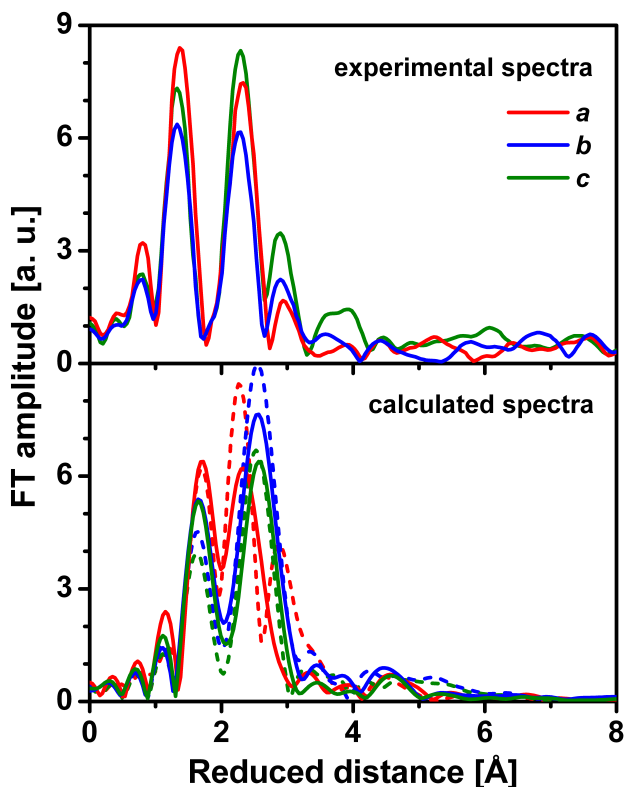


Figure 5.4.:

Fourier transform of polarized EXAFS spectra for crystallized PSII particles. *Top:* Experimental spectra collected by Yano et al. [2006]. *Bottom:* Calculated spectra for the 1.9 Å-structure published in Umena et al. [2011]. The results for both monomers A (solid lines) and B (dashed lines) are shown. Figure from Grundmeier and Dau [2012].

O’Keeffe [1991], it is possible to estimate the oxidation states of the Mn ions as shown in Table 5.3 (see Appendix A.3 for a description of these calculations). Assuming fully localized valencies, this again clearly indicates a heavily reduced Mn complex in a $\text{Mn}_4^{\text{II,II,III,III}}$ complex, which could be denoted as S_{-3} -state (given that $\text{Mn}_4^{\text{III,III,IV,IV}}$ equals the S_1 -state and the sums of the oxidation numbers of these states differ by four).

All in all, photoreduction of the Mn complex during the XRD measurements of Umena et al. [2011] is very likely.

5.5. Models C-I, C-II, C-III, C-IV, D, and F

In the following, six models developed with the optimization procedure described in Section 4.4 are presented. All of these models follow different structural concepts (compare Table 5.4), but are all (with exception of model C-I) optimized for both EXAFS data of partial oriented PSII samples and PSII crystals. All models were optimized starting from the XRD structure of Loll et al. [2005]. The inorganic cores of these models can be seen in Fig. 5.5.

Table 5.3.:

Fractional oxidation states V and Mn-O distances R for the Mn atoms of the manganese complex. The values for both monomers A and B of the XRD data 3ARC presented in Umena et al. [2011] as well as the averaged values for the PSII dimer are given. The fractional oxidation states were derived by linear interpolation of the results shown in Table A.1. Here, a five-coordinated Mn^1 ($N = 5$) and six-coordinated Mn^2 , Mn^3 , and Mn^4 ($N = 6$) were assumed to be present. Table adapted from Grundmeier and Dau [2012].

	N [1]	Monomer A		Monomer B		Dimer	
		R [Å]	V [1]	R [Å]	V [1]	R [Å]	V [1]
Mn^1	5	1.99	2.7	1.97	2.9	1.98	2.8
Mn^2	6	2.08	2.6	2.07	2.7	2.08	2.7
Mn^3	6	2.13	2.4	2.10	2.5	2.12	2.5
Mn^4	6	2.19	2.0	2.17	2.2	2.18	2.1
Mean oxidation state			2.4		2.6		2.5

Model C-I

In Dau et al. [2008], the model shown in Fig. 2.3 was proposed. The XRD data from Loll et al. [2005] and fit results based on extended-range EXAFS data (*Iso*, published within the same article Dau et al. [2008]) were used in combination with geometry optimization via HyperChem to design this model.

A further optimized version—preserving the original idea—is the model C-I. The method described in Section 4.4 was used to optimize the model C-I in regard to the 55° EXAFS data (*Iso*). In contrast to the approach used in Dau et al. [2008], this method takes the ligating amino acids into account, which can significantly influence the EXAFS spectra (compare Section 5.6).

As can be seen in Fig. 5.6, the spectra calculated for the C-I model are in contradiction to the *Mem* and *Cry* data sets. For the *Mem* data this effect can be explained straight forward: The angle $\theta_{R, \text{Mn}^3\text{-Mn}^4}$ between the $\text{Mn}^3\text{-Mn}^4$ vector (2.73 Å) and the membrane normal is only 40°, which results together with the second short Mn-Mn vector (i. e., $\text{Mn}^2\text{-Mn}^3$ with 2.69 Å and 79°) in an average angle equaling roughly the magic angle. Therefore, no significant angle-dependence of the second EXAFS peak is observed for this model.

5. Evaluation of OEC models

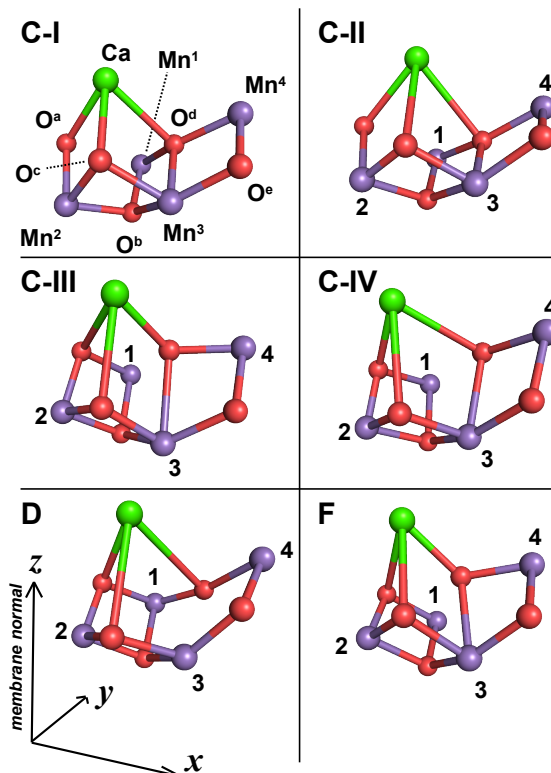


Figure 5.5.:

$\text{Mn}_4\text{Ca}(\mu\text{-O})_4$ cores of the OEC models C-I, C-II, C-III, C-IV, D, and F (S_1 -state). For calculation of model C-I, only the *Iso* spectrum was used. For models C-II, C-III, C-IV, D, and F all data sets (*Iso*, *Mem*, *Cry*) were taken into account.

Model C-II

The model C-II can be seen as an improved version of model C-I. It was obtained using the same initial model and the same restraints as model C-I, but optimized not only for the *Iso* spectra, but also for *Mem* and *Cry* data. This results in an increase of the previously mentioned angle $\theta_{R,\text{Mn}^3\text{-Mn}^4}$ by 10° . This increase results in better agreement with the angle dependence of the *Mem* spectra. Additionally, the crystal spectra (*Cry*) are better reproduced. The calculated spectra for this model can be seen in Figs. 5.7 and 5.8.

Model C-III

In contrast to the two models C-I and C-II, the C-III model is based on a different structural idea: In C-I and C-II, the open coordination site is in trans-position to N-His332, but for model C-III it is in trans-position to O-Asp342. Therefore, a long Mn-O distance ($> 2.4 \text{ \AA}$) occurs between Mn^1 and O^d and not O^a . This equals the structural model proposed by Siegbahn based on DFT calculations [Siegbahn, 2008, 2009]. Instead of $\text{Mn}^3\text{-Mn}^4$ for C-I and C-II, now $\text{Mn}^1\text{-Mn}^2$ is the second short Mn-Mn vector (additionally to $\text{Mn}^2\text{-Mn}^3$). The $\text{Mn}^3\text{-Mn}^4$ distance is now in the region of 3.0 \AA which may indicate a protonation of O^d or O^e .

5.5. Models C-I, C-II, C-III, C-IV, D, and F

Table 5.4.:

Comparison of structural concepts of models C-I to C-IV, D, and F. The first column indicates the five-coordinated manganese ion, the second column shows the two short Mn-Mn distances. The third column finally displays the long Mn-O distance belonging to the open coordination site.

model	five-coordinated Mn ion	short Mn-Mn distances	long ($> 2.4 \text{ \AA}$) Mn-O distance
C-I	Mn ¹	Mn ² -Mn ³ /Mn ³ -Mn ⁴	Mn ¹ -O ^a
C-II	Mn ¹	Mn ² -Mn ³ /Mn ³ -Mn ⁴	Mn ¹ -O ^a
C-III	Mn ¹	Mn ¹ -Mn ² /Mn ² -Mn ³	Mn ¹ -O ^d
C-IV	Mn ¹	Mn ¹ -Mn ² /Mn ² -Mn ³	Mn ¹ -O ^d
D	Mn ³	Mn ¹ -Mn ² /Mn ² -Mn ³	Mn ³ -O ^d
F	Mn ¹	Mn ¹ -Mn ² / Mn ² -Mn ³ /Mn ³ -Mn ⁴	Mn ¹ -O ^d

Model C-IV

This model is similar to model C-III but has a longer Mn¹-Mn⁴ distance (4.3 Å for model C-IV compared to 3.7 Å for models C-I to C-III). Additionally, the O^d-Ca distance is slightly longer (2.3 Å in model C-IV versus 2.2 Å in model C-III). Due to these changes, the atoms Mn¹, O^d, Mn⁴, O^a, Mn³, and O^b all lie roughly within the same plane, which is not given for model C-III. Another interesting feature of the model C-IV is that it only requires small variations of the ligating amino acids during the optimization process via the Levenberg-Marquardt algorithm (see overlay plot in Fig. 5.12).

Model D

The model D has Mn³ as a five-coordinated Mn^{III} ion. This more exotic assumption is not supported by DFT calculations [Siegbahn, 2008, 2009], but results also in qualitatively good agreement to the *Cry/Mem* and *Crys* data sets. Therefore, this idea cannot be ruled out by the in this thesis considered EXAFS and XRD data.

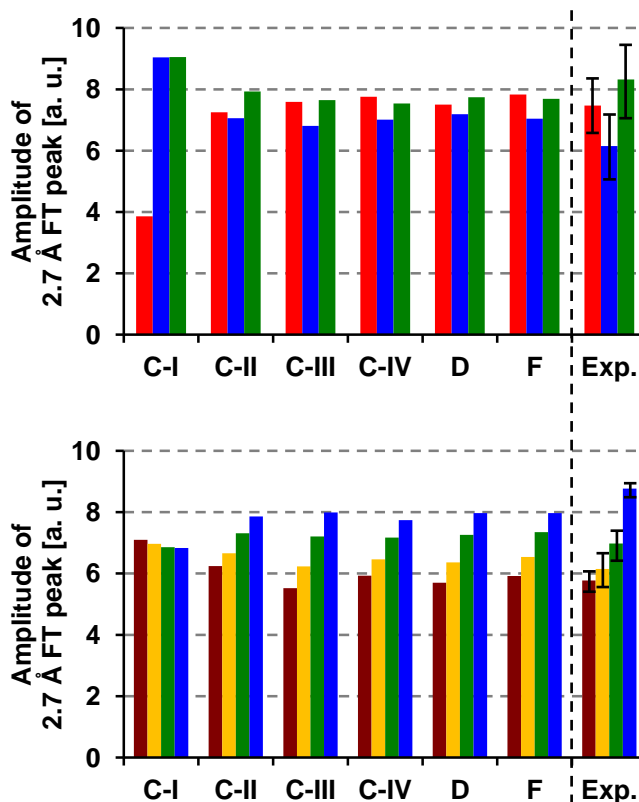
Model F

This model is the only model presented in this section with three short Mn-Mn distances. The overall structural idea is equal to the concepts of the models C-III and C-IV (albeit most of its distances are closer to C-III, compare Table 5.2). The ion Mn¹ is five-coordinated with a long Mn¹-O^d distance. Additionally to the two 2.7 Å Mn-Mn vectors of the models C-III and C-IV, for model F a third short Mn-Mn dis-

5. Evaluation of OEC models

Figure 5.6.:

Bar diagram of the magnitude of the second Fourier peak calculated for models C-I, C-II, C-III, C-IV, D, and F (optimized using the procedure from Section 4.4) and in the experimental spectra. In the upper panel the polarized EXAFS spectra obtained from PSII crystals (*Cry* data) is shown. The lower panel displays the results for polarized EXAFS collected on partially oriented PSII membrane particles (*Mem* data). The error bars for the experimental data are 2σ errors calculated of the FT data in the region between 5.5 and 8.0 Å of reduced distance.



tance exists: The Mn³-Mn⁴ vector is with 2.75 Å significantly shorter as for the models C-III and C-IV (3.03 Å).

This model reproduces the spectra for partially oriented as well as crystal samples reasonably well, although the error value is slightly higher than for models C-III, C-IV, and D. However, this shows that possible models with three short Mn-Mn distances do exist.

5.6. Influence of ligating amino acids on EXAFS

For calculation and optimization of the models C-I, C-II, C-III, C-IV, D, and F all atoms up to a distance of 6.5 Å to the Mn ions were taken into account (see Section 4.4). If these ligating amino acids are neglected, this may influence the resulting EXAFS spectra significantly.

This effect can be seen in Figs. 5.9 and 5.9 for the exemplary case of model C-II. Considering only the ligating oxygens/nitrogens (plus the metal ions) reduces the height of the second FT peak at roughly 2.7 Å. Taking only the five intermetal oxygens into account (i. e., calculating the spectra only for the atoms shown in Fig. 5.5) reduces

5.6. Influence of ligating amino acids on EXAFS

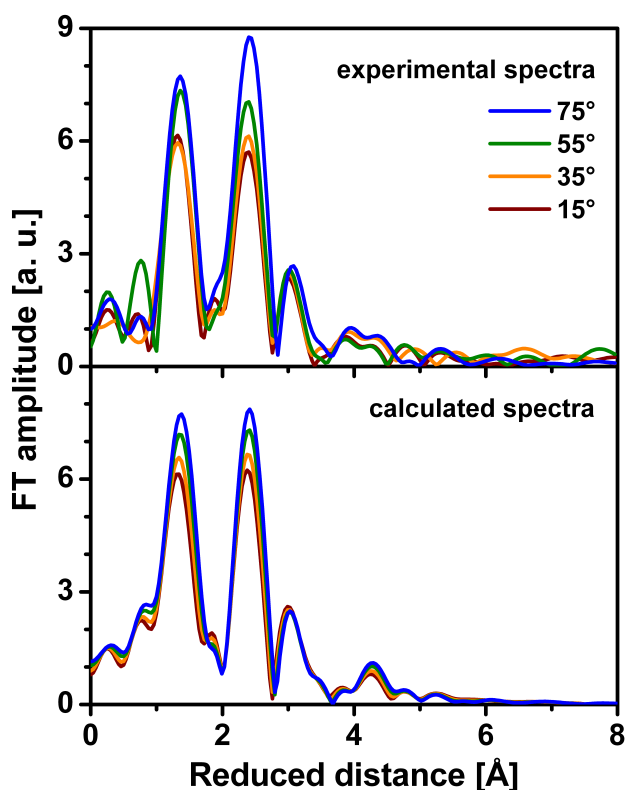


Figure 5.7.:

Fourier transform of polarized EXAFS spectra for partially oriented PSII samples at different excitation angles. *Top:* Experimental EXAFS spectra collected on partially oriented PSII membrane particles (equals *Mem* and *Iso* data). *Bottom:* Calculated spectra calculated for model C-II. Figure from Grundmeier and Dau [2012].

the peak height even further. It is likely that this effect influenced the optimization procedure of Yano et al. [2006]:

As mentioned in Section 5.2, Yano and coworkers did only consider the metal ions plus the intermetal oxygens for the calculation of the EXAFS spectra and the optimization of their models A-I, A-II, A-IIa, and A-III. They state in their article Yano et al. [2006] that “In addition to the 2.8 Å vector, two 2.7 Å vectors are required to reproduce the intensity of the FT peak II [...]. Therefore, the models containing only two short 2.7 Å Mn-Mn distances, or one 2.7 Å and one 2.8 Å Mn-Mn distances [...], were unacceptable in reproducing both the solution range-extended EXAFS and polarized EXAFS data.”

The reason for these observations of Yano and coworkers could be due the effect described above: By neglecting the amino acids for the EXAFS calculations, the EXAFS spectra were changed and a third short Mn-Mn distance became necessary. It should be noted that Yano et al. also excluded the dangler model (model **n** of Fig. 2.8), which was later successfully optimized by Sproviero et al. [2008b]. This exclusion also may have been caused by this over-simplification.

5. Evaluation of OEC models

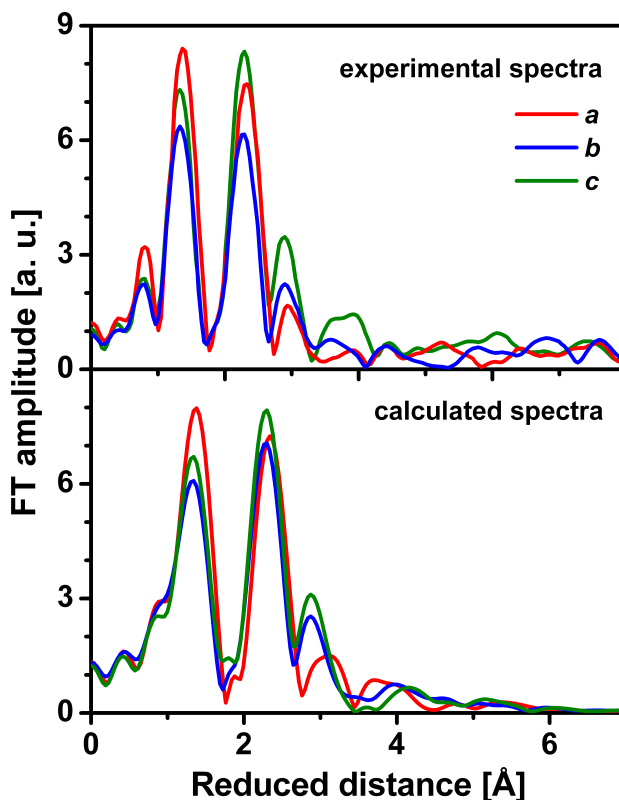


Figure 5.8.:

Fourier transform of polarized EXAFS spectra for crystallized PSII particles. *Top:* Experimental EXAFS spectra collected by Yano et al. [2006] on PSII crystals (*Cry* data). Spectra calculated for model C-II are shown in the lower panel. Figure from Grundmeier and Dau [2012].

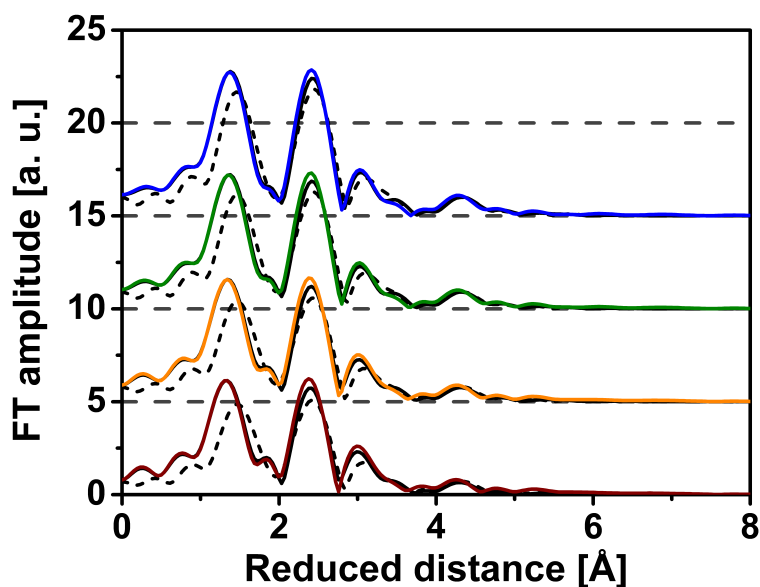


Figure 5.9.:

Influence of the amino acids on the EXAFS spectra in case of model C-II. From top to bottom: 75°, 55°, 35°, 15° between sample normal and electric-field vector of the X-ray beam. Colored lines: All atoms up to 6.5 Å distance to the Mn ions are considered as backscatters. Black solid lines: Only oxygens/nitrogen of the first ligand sphere and metal ions. Black dashed lines: Only intermetal oxygens and metal ions.

5.7. Summary and conclusions

The models of Yano et al. are in strong conflict with the experimental EXAFS data of partially oriented PSII particles (*Mem*). Further, it is difficult to bring these structural models in agreement with current XRD data [Loll et al., 2005; Umena et al., 2011].

The refined model of Sproviero et al. (B-II, R-QM/MM) is in reasonable agreement with the experimental EXAFS results. Nevertheless, conflicts with current XRD results do exist [Loll et al., 2005; Umena et al., 2011].

In contrast, the models C-I to C-IV, D, and F reflect the overall topology suggested by Dau and Haumann [2008], Dau et al. [2008], Siegbahn [2008, 2009] and most recently Umena et al. [2011]. These models are also in agreement with the proposition that in the $S_2 \rightarrow S_3$ transition a five-coordinated Mn^{III} is transformed into a six-coordinated Mn^{IV} [Dau et al., 2001]. This suggestion is supported by changes in the XANES spectra in the $S_2 \rightarrow S_3$ transition [Dau et al., 2003; Müller et al., 2005; Haumann et al., 2005]. Additionally, recent EPR simulations [Pantazis et al., 2009] and the computational work of Siegbahn [2008, 2009] also point toward the presence of five-coordinated Mn^{III} in the S_1 and S_2 states of the OEC (and likely also in the S_0 state).

All in all, the EXAFS-based approach of Dau and coworkers [Dau and Haumann, 2008; Dau et al., 2008; Grundmeier and Dau, 2012] (as described in this thesis) and the DFT-based approach of Siegbahn [2008, 2009]—all in conjunction with the crystallographic model of Loll et al. on the protein environment of the OEC [Loll et al., 2005]—result in similar OEC models. All of these models are largely in line with the high-resolution crystallographic model of Shen and his coworkers [Umena et al., 2011].

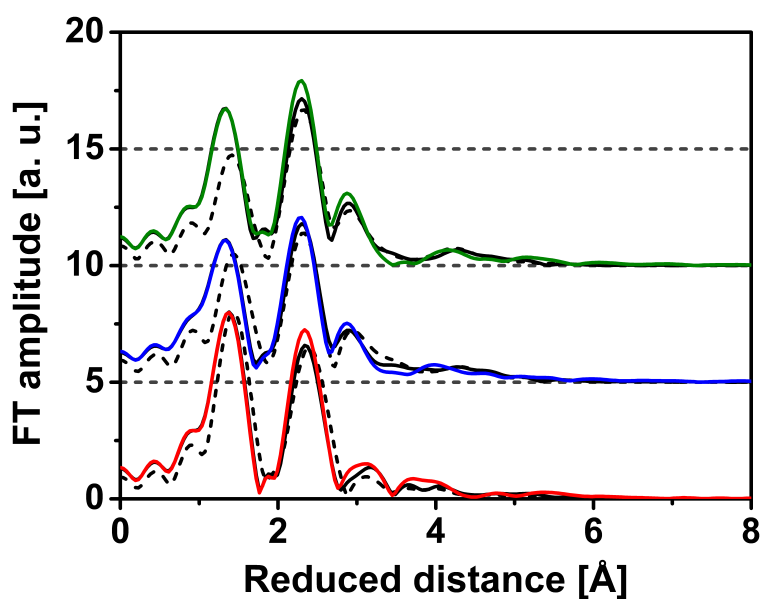


Figure 5.10.:

Influence of the amino acids on the EXAFS spectra in case of model C-II. From top to bottom: Electric-field vector of the X-ray beam parallel to c , b , a axis. Colored lines: All atoms to 6.5 \AA distance to the Mn ions are considered as backscatterers. Black solid lines: Only oxygens/nitrogen of the first ligand sphere and metal ions. Black dashed lines: Only intermetal oxygens and metal ions.

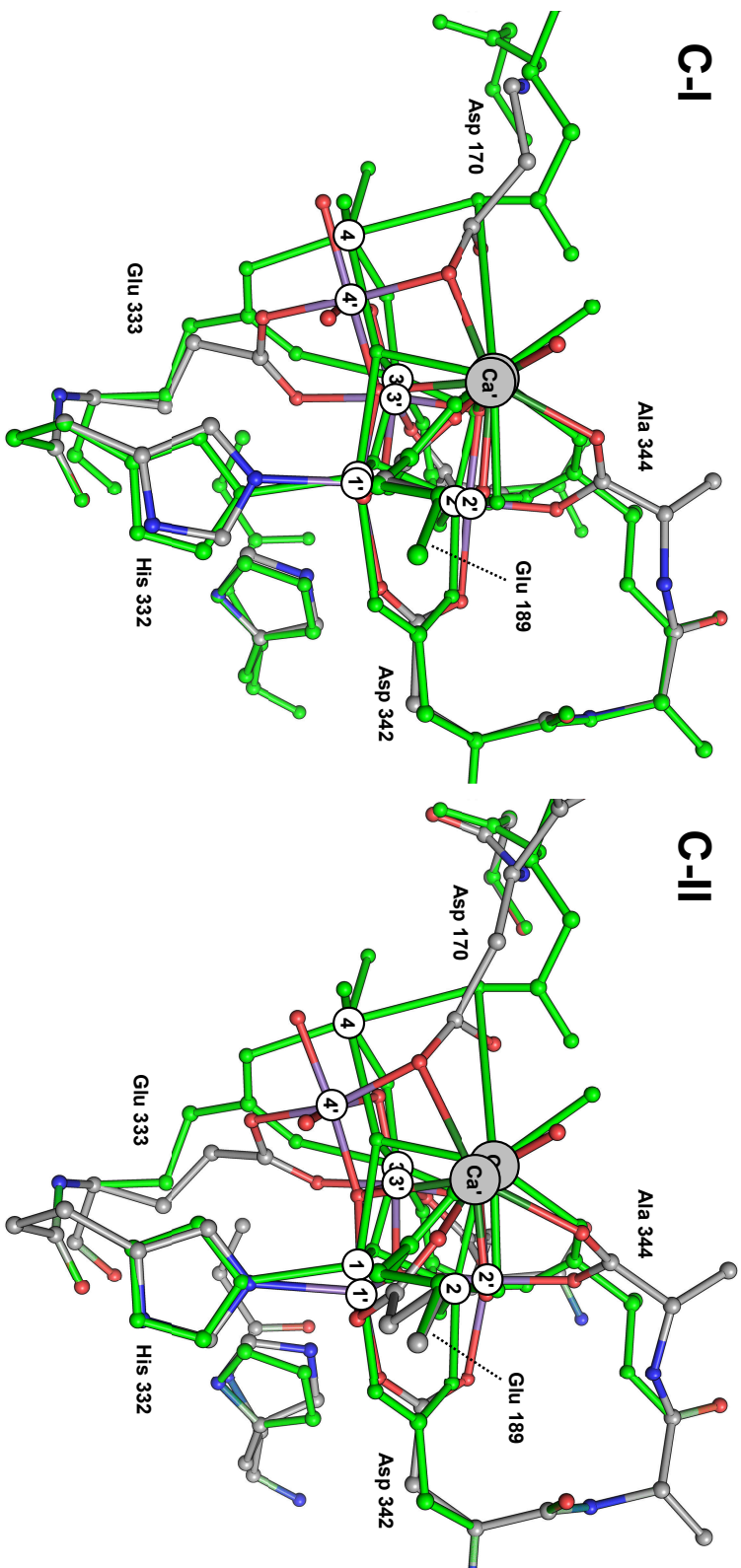


Figure 5.11.:

Overlay of the crystal structure 2AXXT from Loll et al. [2005] (bright green) and the OEC model C-I and C-II (colored). The encircled numbers reflect the positions of the Mn ions. Primed numbers and the label Ca²⁺ relate to the structures of model C-I and C-II. Figure from Grundmeier and Dau [2012].

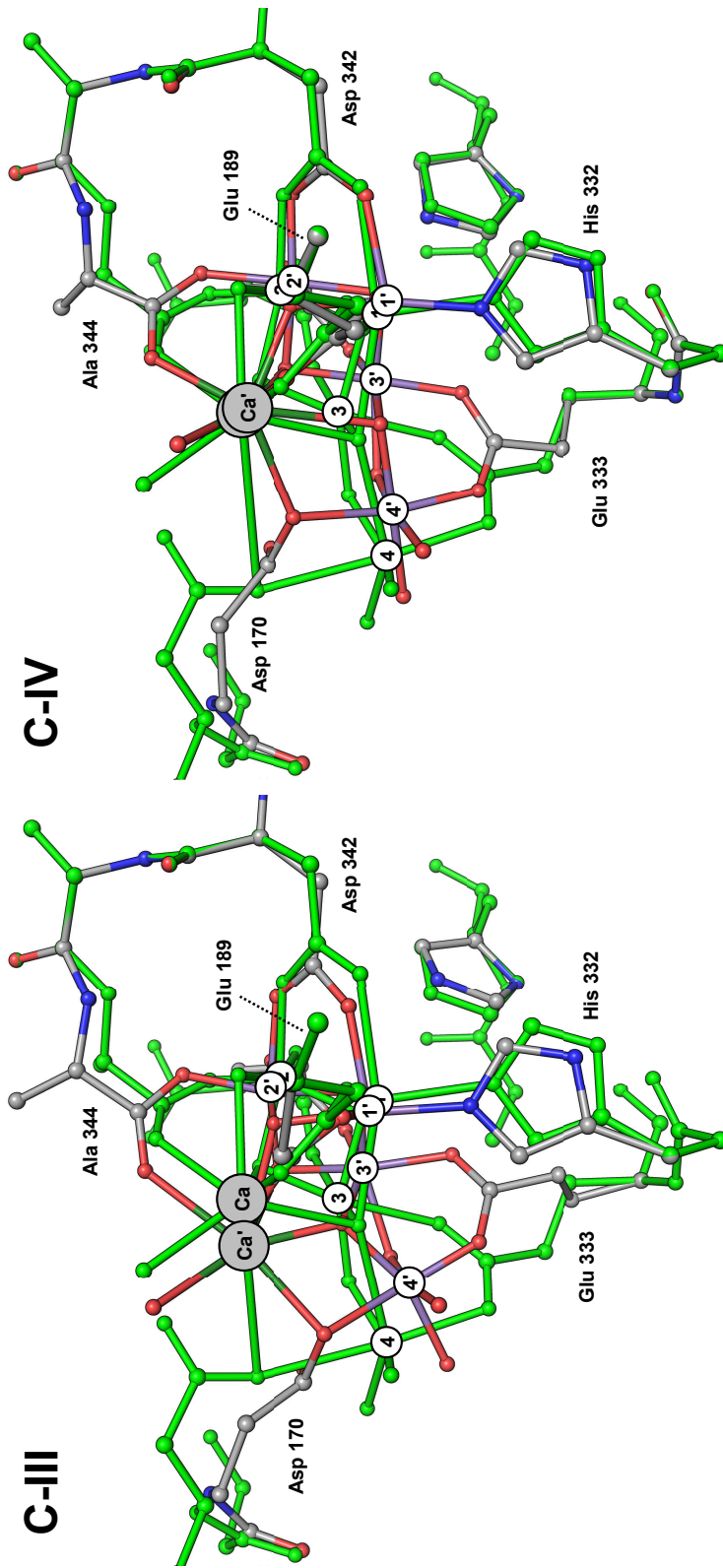


Figure 5.12.:

Overlay of the crystal structure 2AXT from Loll et al. [2005] (bright green) and the OEC model C-III and C-IV (colored). The encircled numbers reflect the positions of the Mn ions. Primed numbers and the label Ca' relate to the structures of model C-III and C-IV. Figure from Grunmeier and Dau [2012].

5. Evaluation of OEC models

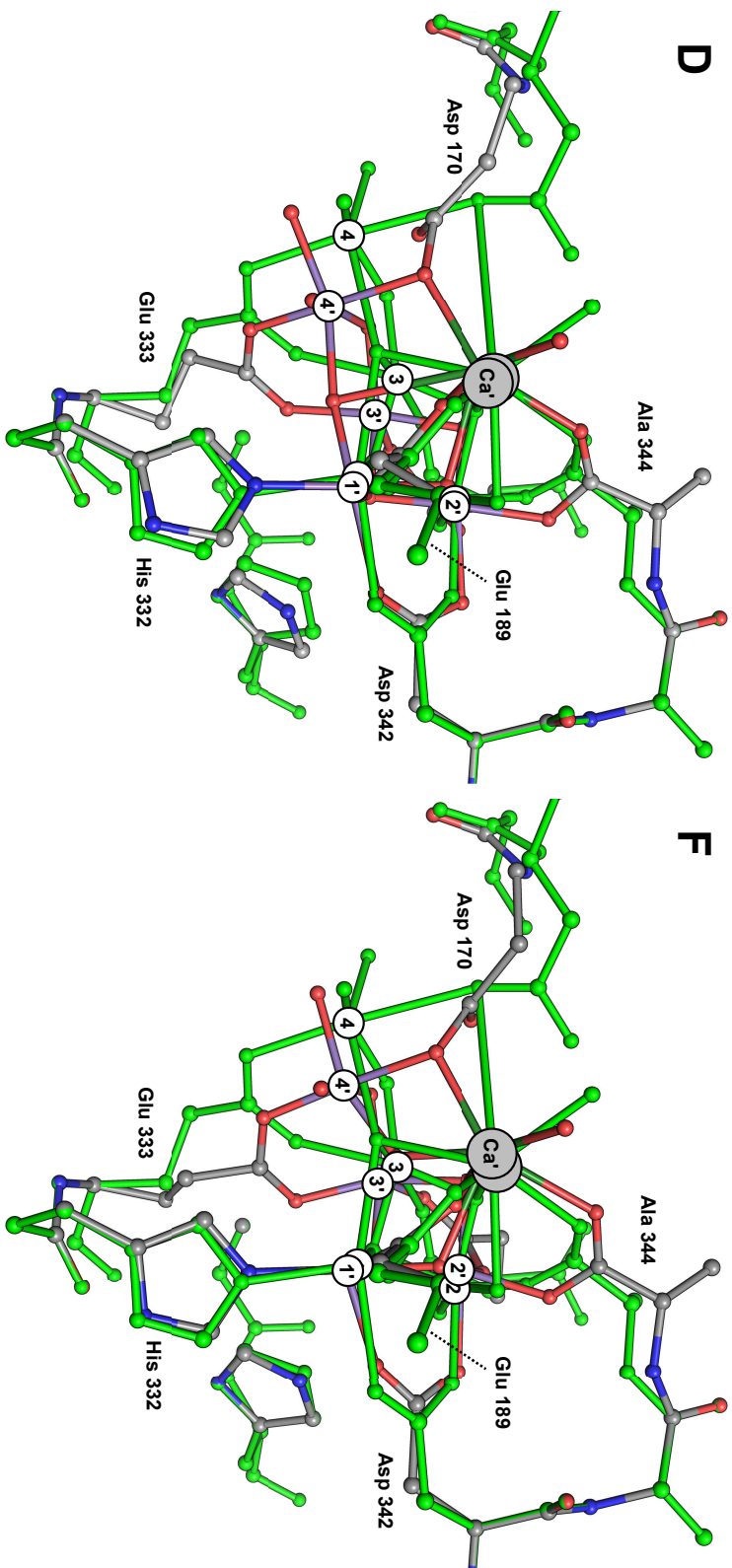


Figure 5.13.:

Overlay of the crystal structure 2AXT from Loll et al. [2005] (bright green) and the OEC model D and F (colored). The encircled numbers reflect the positions of the Mn ions. Primed numbers and the label Ca²⁺ relate to the structures of model D and F. Left figure from Grundmeier and Dau [2012].

6. Implications and future directions

In this chapter, mechanistic implications of the recently developed models for the process of photosynthetic water oxidation will be presented. Additionally, this chapter will give an overview of open problems regarding the manganese complex and possible new approaches will be discussed. The chapter closes with a summary of this thesis.

6.1. Mechanistic implications

In literature several possible mechanisms for the photosynthetic water oxidation at the manganese complex have been proposed. In Fig. 6.1, seven proposed modes (named A–G) for the O–O bond formation are listed. In the following these modes will be discussed based on the recent structural information presented in the chapters before.

- A:** The structure of the manganese complex as resolved by X-ray crystallography [Ferreira et al., 2004; Loll et al., 2005; Umena et al., 2011] as well as all models presented in this thesis show a particularly exposed position of the Mn^4 ion. Additionally, terminally coordinated water molecules (H_2O or OH^-) are only found for this single Mn ion (Figs. 2.3, 2.5, and 6.2). This suggests an essential role of the Mn^4 in the process of O–O bond formation. The possibility that two different Mn ions are deprotonated to form an O–O bond as shown in Fig. 6.1A and proposed by Babcock and coworkers [Hoganson et al., 1995; Hoganson and Babcock, 1997; Tommos and Babcock, 1998; Tommos et al., 1998] can therefore be excluded.
- B:** An O–O bond formation between the oxygens of two water molecules O^{W1} and O^{W2} as shown in Fig. 6.1B at the Mn^4 ion (compare also Figs. 2.3, 2.5, and 6.2) seems not possible on a first glance: Wydrzynski, Messinger, Hillier, and their coworkers showed that there are two binding sites for the two substrate water molecules [Messinger et al., 1995; Hillier et al., 1998; Hillier and Wydrzynski, 2000, 2001; Hillier et al., 2001; Hillier and Wydrzynski, 2004, 2008] that are distinct and “immiscible”: The water molecules can only slowly exchange their positions. On the other hand, a rapid exchange between O^{W1} and O^{W2} appears likely. However, the hydrogen bonds implied by the XRD data of Umena et al. [2011] may indeed prevent the water molecules from exchanging their position quickly. Therefore, this possibility cannot be ruled out.

6. Implications and future directions

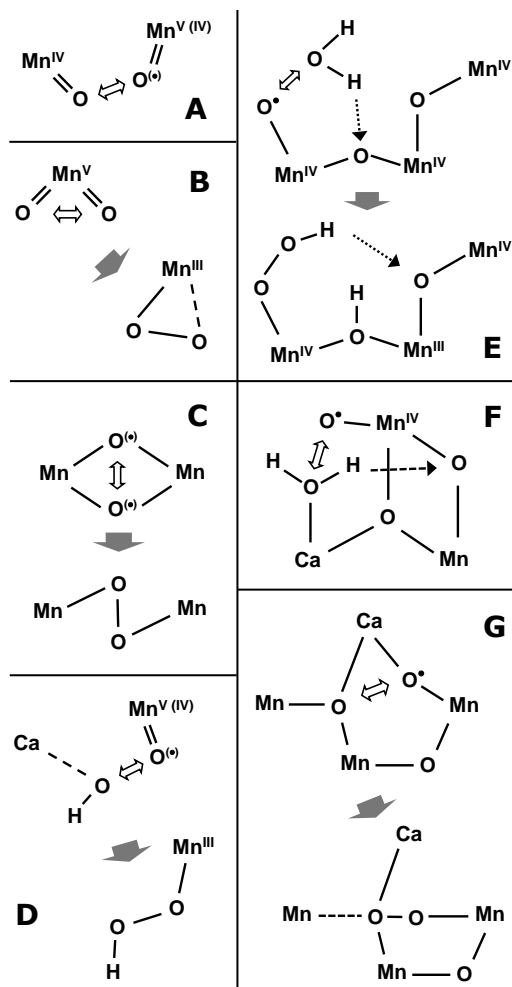


Figure 6.1.:

Some in literature proposed modes for O-O bond formation. For a detailed explanation, see text. Figure from Grundmeier and Dau [2012].

- C:** The O-O formation between two bridging oxygens seems unlikely due to the OEC structure: All μ -oxygens despite O^e are stabilized by bonds to three metal ions (μ_3 -O). The oxygen O^e only bridges two metal atoms (Mn^3 and Mn^4), but a hydrogen bond to Arg 357 might stabilize this atom. Additionally, the exchange of bridging oxygens [Tagore et al., 2006, 2007] normally takes too much time to be in accord with the experimentally observed exchange rates for the PSII substrate water [Messinger et al., 1995; Hillier et al., 1998; Hillier and Wydrzynski, 2000, 2001; Hillier et al., 2001; Hillier and Wydrzynski, 2004, 2008]. Nevertheless,

6.1. Mechanistic implications

recent DFT calculations by Siegbahn [2008, 2009] indicate that a O-O formation involving the oxygen O^d might be feasible (see mode G).

Assuming that one of the water species at the Mn^4 is an oxyl radical, the O-O bond formation mechanism might work due to a nucleophilic attack of a water or hydroxide coordinated to the Ca ion (Figs. 6.1D, 6.1F), or alternatively originates from outer-sphere water (Fig. 6.1E). Such nucleophilic attack mechanisms have been discussed on basis of crystallographic results [Ferreira et al., 2004; McEvoy and Brudvig, 2006; Barber and Murray, 2008; Barber, 2009].

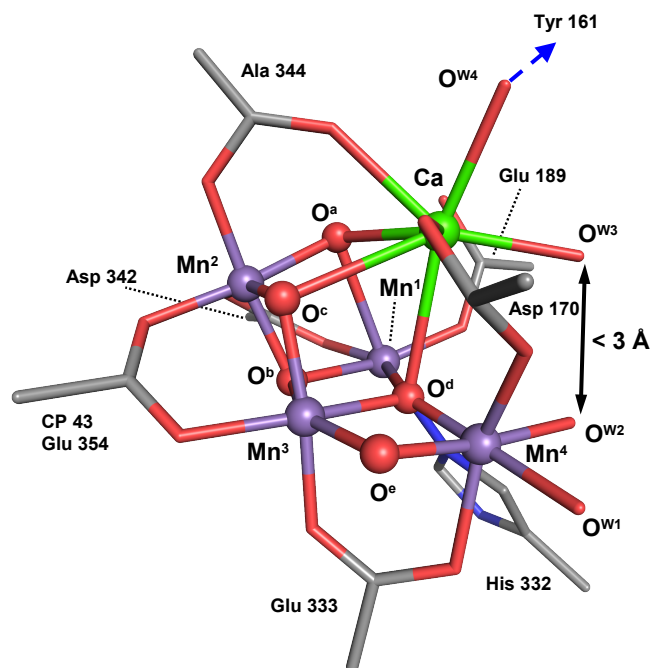
- D:** The recent XRD results by Umena et al. [2011] show a second water molecule (O^{W3} in Fig. 6.2) bond to the Ca ion (in contrast to a bond to Glu 189 as in the crystallographic data from Loll et al. [2005]) and relatively close to an oxyl group (O^{W4} in Fig. 6.2) at Mn^4 . A nucleophilic attack of the Ca-bound water molecule toward this pxyl group seems possible (compare Fig. 6.2).
- E:** In Dau et al. [2001], a nucleophilic attack of an outer-sphere water is described where one or more protons from an outer-sphere water are transferred to bridging oxygens.
- F:** Brudvig, Batista, Sproviero, and coworkers presented a detailed mechanism including a nucleophilic attack by a Ca-bound water. This mode is based on the XRD results of Ferreira et al. [2004] and quantum chemical studies [McEvoy et al., 2005; McEvoy and Brudvig, 2006; Sproviero et al., 2007, 2008c,d]. It was pointed out that the Arg 357 (of CP 43) may facilitate proton movements and serve as a catalytic base. As shown in Fig. 6.1F, it involves the transfer of a proton to a bridging oxide. However, this research is based on the XRD model of Ferreira et al. [2004], which is not in agreement with the most recent crystallographic results [Loll et al., 2005; Guskov et al., 2009; Umena et al., 2011].
- G:** Based on DFT calculations, Siegbahn and coworkers derived a model for the S_1 -state of the OEC, which is similar to the model C-III and C-IV presented in this work [Siegbahn, 2008, 2009]. During the $S_2 \rightarrow S_3$ transition, a hydroxide binds at Mn^1 . This oxygen then serves as a bridging ligand between Mn^1 and the Ca ion. After that, it is deprotonated plus oxidized in the $S_3 \rightarrow S_4$ transition and becomes a oxygen radical. As Fig. 6.1G shows, now an O-O bond can be formed between O^d (bridging Mn^3 , Mn^4 , and Ca) and this radical. This from Siegbahn and coworkers predicted mechanism and its S_1 -state model are in good agreement to both the XRD data and the EXAFS measurements (compare model C-III and C-IV).

With the current structural information available on the manganese complex several O-O bond formation modes can be excluded. Beside the O-O bond formation proposed by Siegbahn (mode G) the nucleophilic attack toward an oxyl radical seem likely.

6. Implications and future directions

Figure 6.2.:

Schematic illustration of the OEC complex (based on the coordinates of model C-II plus the ligand environment from Umena et al. [2011]). A nucleophilic attack of the water (or hydroxide) O^{W3} on the oxyl ligand O^{W2} of Mn^4 seems sterically possible. Figure from Grundmeier and Dau [2012].



The attacking substrate water could be an outer-sphere water species (mode E) or a hydroxid coordinated by the Ca ion (mode D). Alternatively, the extensive hydrogen-bonding network formed by the water molecules O^{W1} , O^{W2} , O^{W3} , O^{W4} (see Fig. 6.2), the Tyr161-His190 moiety, and several outer-sphere water molecules (Fig. 2.5) may facilitate O-O bond formation mechanisms (compare Dau et al. [2010]).

6.2. Future perspectives and outlook

During the last decades, huge progress was made in understanding the structure of the Mn complex of PSII and also the mechanism of water oxidation. However, many questions remain open. In the following, some of these still existing problems are pointed out and possibilities for new approaches (in conjunction with this work) are listed.

- The classical S-state cycle consists of four one-electron oxidation steps [Kok et al., 1970]. Later it was found that the accumulation of positive charges proposed by Kok will increase tremendously the energy required to remove the next electron and therefore alternating e^- and H^+ removal is required [Dau and Haumann, 2006]. This extended S-state cycle is shown in Fig. 6.3 [Dau and Haumann, 2007a,b, 2008]. Each of these steps—including the corresponding energetics and kinetics [Dau and Zaharieva, 2009]—needs to be brought in line with the stru-

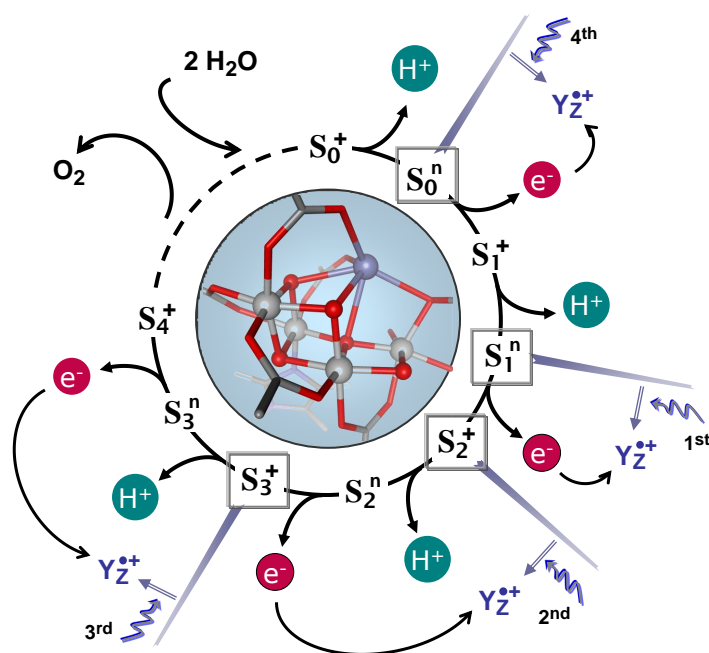


Figure 6.3.:

Extended S-state cycle as proposed by Dau and Haumann [2006, 2007a]. The states S_1^n , S_2^+ , S_3^+ , and S_0^n correspond to the four S-states of the classical Kok cycle [Kok et al., 1970]. In this extended cycle, electrons and protons are removed alternately from the Mn complex. Figure from Grundmeier and Dau [2012].

ral information available today through *inter alia* XRD and XAS as presented in this thesis.

- The chemical and structural changes accompanying each step of the S-state cycle are still not completely understood [Dau and Haumann, 2008]. Therefore, it may be beneficial to develop new methods to complement the present experimental results. As an example for such a new approach, in Fig. 16 of Grundmeier and Dau [2012] a new X-ray spectroscopy experiment is presented: Emission-resolved X-ray spectroscopy with utilization of the linear dichroism effect. This experiment (developed and conducted by Dau, Zaharieva, Haumann, Chernev, and Risch) is based on measuring Mn K-edge spectra under angles of 15° and 55° , but registering the fluorescence at three different emission energies at the Mn- K_α emission lines.
- An atomistic model of the OEC including structures and free-energy differences for all steps of the extended S-state cycle in Fig. 6.3 was proposed by Siegbahn [2008, 2009]. It should be tested, if this model is really in agreement with all experimental information available today. Additionally, it is necessary to gain new experimental results to prove or disprove this models. Especially an estimate for the free-energy differences for each of the steps shown in Fig. 6.3 is needed. First approaches in this direction have been made by Zaharieva et al. [2011] (based on the work of Bernat et al. [2002] and Suzuki et al. [2005]).
- In each step of the S-state cycle, either a Mn ion or the water substrate is

6. Implications and future directions

partially oxidized. The corresponding oxidant in PSII is Tyr_Z with a midpoint potential of $E_m \approx +1.2$ V for the Tyr_Z[•]/Tyr_Z couple [Rappaport et al., 2002; Grabolle and Dau, 2005; Cser and Vass, 2007; Rappaport and Diner, 2008; Dau and Zaharieva, 2009]. This potential equals the anodic potential in electrochemical water oxidation. In electrochemical water oxidation, the overpotential is determined by the step associated with the largest potential requirements. This defines the energetic efficiency of the process. For PSII, the overpotential is only roughly 0.3 V at pH 5 and in PSII the reactions in water oxidation have to be so fast that charge recombinations are impossible [Grabolle and Dau, 2007; Dau and Zaharieva, 2009]. Complete understanding of these highly optimized steps before the O-O bond formation is crucial for full insight into the process of water oxidation.

Beside the more general problems listed above, several improvements for the structure-modeling approach described in this thesis and in the article by Grundmeier and Dau [2012] are conceivable:

- In this thesis, for modeling of the Mn complex, geometry optimization using HyperChem and calculations of EXAFS spectra were done alternately. A direct combination of a molecular-mechanics or DFT approach and calculation of EXAFS data via a combined error value would be more convenient and precise.
- Only extended-range EXAFS data for 55° between the sample normal and the electric-field vector of the incoming X-ray beam were used. Extended-range spectra for all used angles would improve the accuracy considerably.
- The S-state considered in this thesis was the S₁-state. It may be promising to use LD-EXAFS spectra (preferably extended-range) for additional S-states and construct models based on these data. Combining the results for all S-states should drastically reduce the number of possible models.
- The now X-ray crystallography results from Loll et al. [2005] served as a starting point for the construction of the models of the Mn complex presented in this thesis. Despite being mostly very similar to the data of Loll and coworkers (as pointed out in Section 2.2), new modeling should be done based on the XRD data of Umena et al. [2011].

References

- Aasa, R., Andréasson, L.-E., Styring, S., and Vänngård, T. (1989). The nature of the Fe(III) EPR signal from the acceptor-side iron in photosystem II. *FEBS Lett.*, 243(2):156 – 160.
- Ankudinov, A. L. and Rehr, J. J. (2003). Development of XAFS theory. *J. Synchrotron Radiat.*, 10(Pt 5):366–368.
- Barber, J. (2009). Photosynthetic energy conversion: natural and artificial. *Chem. Soc. Rev.*, 38(1):185–196.
- Barber, J. and Murray, J. W. (2008). Revealing the structure of the Mn-cluster of photosystem II by X-ray crystallography. *Coord. Chem. Rev.*, 252(3-4):233–243.
- Barra, M., Haumann, M., Loja, P., Krivanek, R., Grundmeier, A., and Dau, H. (2006). Intermediates in assembly by photoactivation after thermally accelerated disassembly of the manganese complex of photosynthetic water oxidation. *Biochemistry*, 45(48):14523–14532.
- Bernat, G., Morvaridi, F., Feyziyev, Y., and Styring, S. (2002). pH-dependence of the four individual transitions in the catalytic S-cycle during photosynthetic oxygen evolution. *Biochemistry*, 41(18):5830–5843.
- Berthold, D. A., Babcock, G. T., and Yocum, C. F. (1981). A highly resolved, oxygen-evolving photosystem II preparation from spinach thylakoid membranes. *FEBS Lett.*, 134(2):231–234.
- Biesiadka, J., Loll, B., Kern, J., Irrgang, K.-D., and Zouni, A. (2004). Crystal structure of cyanobacterial photosystem II at 3.2 Å resolution: a closer look at the Mn-cluster. *Phys. Chem. Chem. Phys.*, 6:4733–4736.
- Blankenship, R. (2002). *Molecular Mechanisms of Photosynthesis*. Blackwell Science, Oxford, England.
- Brese, N. E. and O’Keeffe, M. (1991). Bond-valence parameters for solids. *Acta Cryst.*, B47:192–197.
- Britt, R. D., Campbell, K. A., Peloquin, J. M., Gilchrist, M. L., Aznar, C. P., Dicus, M. M., Robblee, J., and Messinger, J. (2004). Recent pulsed EPR studies of

References

- the photosystem II oxygen-evolving complex: implications as to water oxidation mechanisms. *Biochim. Biophys. Acta*, 1655(1-3):158–171.
- Brown, I. D. and Altermatt, D. (1985). Bond-valence parameters obtained from a systematic analysis of the inorganic crystal structure database. *Acta Cryst.*, B41:244–247.
- Brudvig, G. W. and Crabtree, R. H. (1986). Mechanism for photosynthetic O₂ evolution. *Proc. Natl. Acad. Sci. U. S. A. of America*, 83(13):4586–4588.
- Cinco, R. M., McFarlane Holman, K. L., Robblee, J. H., Yano, J., Pizarro, S. A., Bellacchio, E., Sauer, K., and Yachandra, V. K. (2002). Calcium EXAFS establishes the Mn-Ca cluster in the oxygen-evolving complex of photosystem II. *Biochemistry*, 41(43):12928–12933.
- Cinco, R. M., Robblee, J. H., Messinger, J., Fernandez, C., McFarlane Holman, K. L., Sauer, K., and Yachandra, V. K. (2004). Orientation of calcium in the Mn₄Ca cluster of the oxygen-evolving complex determined using polarized strontium EXAFS of photosystem II membranes. *Biochemistry*, 43(42):13271–13282.
- Cser, K. and Vass, I. (2007). Radiative and non-radiative charge recombination pathways in photosystem II studied by thermoluminescence and chlorophyll fluorescence in the cyanobacterium *synechocystis* 6803. *Biochim. Biophys. Acta*, 1767(3):233–243.
- Dau, H., Andrews, J. C., Roelofs, T. A., Latimer, M. J., Liang, W., Yachandra, V. K., Sauer, K., and Klein, M. P. (1995). Structural consequences of ammonia binding to the manganese center of the photosynthetic oxygen-evolving complex: an X-ray absorption spectroscopy study of isotropic and oriented photosystem II particles. *Biochemistry*, 34(15):5274–5287.
- Dau, H., Dittmer, J., Epple, M., Hanss, J., Kiss, E., Rehder, D., Schulzke, C., and Vilter, H. (1999). Bromine K-edge EXAFS studies of bromide binding to bromoperoxidase from *Ascophyllum nodosum*. *FEBS Lett.*, 457(2):237–240.
- Dau, H., Dittmer, J., Iuzzolino, L., Schiller, H., Dörner, W., Heinze, I., Sole, V. A., and Nolting, H. F. (1997). X-ray absorption linear dichroism spectroscopy (XALDS) on the photosystem II manganese complex: Radiation damage and S₁-state K-edge spectra. *J. Phys. IV*, 7(C2):607–610.
- Dau, H., Grundmeier, A., Loja, P., and Haumann, M. (2008). On the structure of the manganese complex of photosystem II: extended-range EXAFS data and specific atomic-resolution models for four S-states. *Philos. Trans. R. Soc. London, Ser. B*, 363(1494):1237–1243.

- Dau, H. and Haumann, M. (2006). Reaction cycle of photosynthetic water oxidation in plants and cyanobacteria (response letter). *Science*, 312:1471–1472.
- Dau, H. and Haumann, M. (2007a). Eight steps preceding O-O bond formation in oxygenic photosynthesis—A basic reaction cycle of the photosystem II manganese complex. *Biochim. Biophys. Acta*, 1767:472–483.
- Dau, H. and Haumann, M. (2007b). Time-resolved X-ray spectroscopy leads to an extension of the classical s-state cycle model of photosynthetic oxygen evolution. *Photosynth. Res.*, 92:327–343.
- Dau, H. and Haumann, M. (2008). The manganese complex of photosystem II in its reaction cycle—Basic framework and possible realization at the atomic level. *Coord. Chem. Rev.*, 252(3-4):273–295.
- Dau, H., Iuzzolino, L., and Dittmer, J. (2001). The tetra-manganese complex of photosystem II during its redox cycle—X-ray absorption results and mechanistic implications. *Biochim. Biophys. Acta*, 1503(1-2):24–39.
- Dau, H., Liebisch, P., and Haumann, M. (2003). X-ray absorption spectroscopy to analyze nuclear geometry and electronic structure of biological metal centers—potential and questions examined with special focus on the tetra-nuclear manganese complex of oxygenic photosynthesis. *Anal. Bioanal. Chem.*, 376:562–583. 10.1007/s00216-003-1982-2.
- Dau, H., Liebisch, P., and Haumann, M. (2004). The structure of the manganese complex of Photosystem II in its dark-stable S₁-state—EXAFS results in relation to recent crystallographic data. *Phys. Chem. Chem. Phys.*, 6:4781–4792.
- Dau, H., Limberg, C., Reier, T., Risch, M., Roggan, S., and Strasser, P. (2010). The mechanism of water oxidation: from electrolysis via homogeneous to biological catalysis. *ChemCatChem*, 2(7):724–761.
- Dau, H. and Zaharieva, I. (2009). Principles, efficiency, and blueprint character of solar-energy conversion in photosynthetic water oxidation. *Acc. Chem. Res.*, 42(12):1861–1870.
- Debus, R. J. (1992). The manganese and calcium ions of photosynthetic oxygen evolution. *Biochim. Biophys. Acta*, 1102(3):269–352.
- Debus, R. J. (2008). Protein ligation of the photosynthetic oxygen-evolving center. *Coord. Chem. Rev.*, 252(3-4):244–258.
- DeLano Scientific, LLC (2008). The PyMOL molecular graphics system, version 1.1r1.

References

- DeRose, V. J., Yachandra, V. K., McDermott, A. E., Britt, R. D., Sauer, K., and Klein, M. P. (1991). Nitrogen ligation to manganese in the photosynthetic oxygen-evolving complex: continuous-wave and pulsed EPR studies of photosystem II particles containing ^{14}N or ^{15}N . *Biochemistry*, 30(5):1335–1341.
- Dismukes, G. C. and Siderer, Y. (1981). Intermediates of a polynuclear manganese center involved in photosynthetic oxidation of water. *Proc. Natl. Acad. Sci. U. S. A.*, 78(1):274–278.
- Dittmer, J. (1999). *Linear-Dichroismus-Röntgenabsorptionsspektroskopie zum katalytischen Zyklus des wasserspaltenden Mangankomplexes der Photosynthese in Theorie und Experiment*. PhD thesis, Christian-Albrechts-Universität zu Kiel.
- Dittmer, J. and Dau, H. (1998). Theory of the linear dichroism in the extended X-ray absorption fine structure (EXAFS) of partially vectorially ordered systems. *J. Phys. Chem. B*, 102(42):8196–8200.
- Evelo, R., Styring, S., Rutherford, A. W., and Hoff, A. J. (1989). EPR relaxation measurements of photosystem II reaction centers: influence of S-state oxidation and temperature. *Biochim. Biophys. Acta*, 973:428–442.
- Ferreira, K. N., Iverson, T. M., Maghlaoui, K., Barber, J., and Iwata, S. (2004). Architecture of the photosynthetic oxygen-evolving center. *Science*, 303(5665):1831–1838.
- Frigo, M. and Johnson, S. G. (2005). The design and implementation of FFTW3. *Proceedings of the IEEE*, 93(2):216–231. Special issue on “Program Generation, Optimization, and Platform Adaptation”.
- George, G. N., Hedman, B., and Hodgson, K. O. (1998). An edge with XAS. *Nat. Struct. Biol.*, 5(S):645–647.
- George, G. N., Prince, R. C., and Cramer, S. P. (1989). The manganese site of the photosynthetic water-splitting enzyme. *Science*, 243:789–791.
- Goodin, D. B., Yachandra, V. K., Britt, R. D., Sauer, K., and Klein, M. P. (1984). The state of manganese in the photosynthetic apparatus. 3. Light-induced changes in X-ray absorption (K-edge) energies of manganese in photosynthetic membranes. *Biochim. Biophys. Acta*, 767:324–332.
- Grabolle, M. and Dau, H. (2005). Energetics of primary and secondary electron transfer in photosystem II membrane particles of spinach revisited on basis of recombination-fluorescence measurements. *Biochim. Biophys. Acta*, 1708(2):209–218.

- Grabolle, M. and Dau, H. (2007). Efficiency and role of loss processes in light-driven water oxidation by PSII. *Physiol. Plant.*, 131:50–63.
- Grundmeier, A. and Dau, H. (2012). Structural models of the manganese complex of photosystem II and mechanistic implications. *Biochim. Biophys. Acta*, 1817(1):88–105.
- Grundmeier, A., Loja, P., Haumann, M., and Dau, H. (2008a). The manganese complex of photosystem II: Extended-range EXAFS data and specific structural models for four S-states. In *Photosynthesis. Energy from the Sun*, volume 4, pages 405–408. Springer, Berlin/Heidelberg, Germany.
- Grundmeier, A., Repen, B., Süß, B., Tietz, T., Limberg, C., Anderlund, M., Magnuson, A., Haumann, M., and Dau, H. (2006). Photosynthetic water oxidation: The protein-bound manganese complex of photosystem II and biomimetic models studied by XAS at the Mn K-edge. *BESSY Annual Report 2006*, pages 282–284.
- Grundmeier, A., Risch, M., Sanganas, O., Gerencsér, L., Löscher, S., Zaharieva, I., Chernev, P., Pfirrmann, S., Limberg, C., Marinos, N., Driess, M., Hörnke, M., Koks, B., Kraehmer, V., Rehder, D., Anderlund, M., Magnuson, A., Haumann, M., and Dau, H. (2008b). Synthetic models of biological metal centers studied by X-ray absorption spectroscopy at V, Mn, Fe, Ni, and Zn K-edges. *BESSY Annual Report 2008*, pages 403–404.
- Gu, W., Jacquamet, L., Patil, D. S., Wang, H. X., Evans, D. J., Smith, M. C., Millar, M., Koch, S., Eichhorn, D. M., Latimer, M., and Cramer, S. P. (2003). Refinement of the nickel site structure in desulfovibrio gigas hydrogenase using range-extended exafs spectroscopy. *J. Inorg. Biochem.*, 93(1-2):41–51.
- Guskov, A., Kern, J., Gabdulkhakov, A., Broser, M., Zouni, A., and Saenger, W. (2009). Cyanobacterial photosystem II at 2.9-Å resolution and the role of quinones, lipids, channels and chloride. *Nat. Struct. Mol. Biol.*, 16(3):334–342.
- Gust, D. and Moore, T. A. (1989). Mimicking photosynthesis. *Science*, 244(4900):35–41.
- Haddy, A. (2007). EPR spectroscopy of the manganese cluster of photosystem II. *Photosynth. Res.*, 92(3):357–368.
- Haken, H. and Wolf, H. C. (1996). *Atom- und Quantenphysik*. Springer, Berlin/Heidelberg, Germany, 6th edition.
- Hammarström, L. and Hammes-Schiffer, S. (2009). Special issue on artificial photosynthesis and solar fuels. *Acc. Chem. Res.*, 42(12):1859–2029.

References

- Harris, F. (1978). On the use of windows for harmonic analysis with the discrete fourier transform. *Proceedings of the IEEE*, 66(1):51–83.
- Hasegawa, K., Ono, T., Inoue, Y., and Kusunoki, M. (1999). Spin-exchange interactions in the S₂-state manganese tetramer in photosynthetic oxygen-evolving complex deduced from g=2 multiline EPR signal. *Chem. Phys. Lett.*, 300(1-2):9–19.
- Haumann, M., Barra, M., Loja, P., Löscher, S., Krivanek, R., Grundmeier, A., Andreasson, L. E., and Dau, H. (2006). Bromide does not bind to the Mn₄Ca complex in its S₁ state in Cl⁻-depleted and Br⁻-reconstituted oxygen-evolving photosystem II: evidence from X-ray absorption spectroscopy at the Br K-edge. *Biochemistry*, 45(43):13101–13107.
- Haumann, M., Grabolle, M., Neisius, T., and Dau, H. (2002a). The first room-temperature X-ray absorption spectra of higher oxidation states of the tetramanganese complex of photosystem II. *FEBS Lett.*, 512(1-3):116–120.
- Haumann, M., Grabolle, M., Werthammer, M., Iuzzolino, L., Dittmer, J., Meyer-Klaucke, W., Neisius, T., and Dau, H. (2001). The manganese complex of Photosystem II: a structural model for the S₁, S₂, and S₃ oxidation states derived from linear dichroism EXAFS spectroscopy at 20 K and at room temperature. In *Proceedings of the 12th International Congress on Photosynthesis*, pages S10–013 1–5, Melbourne, Australia, Brisbane, Australia. CSIRO Publishing.
- Haumann, M., Grundmeier, A., Zaharieva, I., and Dau, H. (2008). Photosynthetic water oxidation at elevated dioxygen partial pressure monitored by time-resolved X-ray absorption measurements. *Proc. Natl. Acad. Sci. U. S. A.*, 105(45):17384–17389.
- Haumann, M., Müller, C., Liebisch, P., Iuzzolino, L., Dittmer, J., Grabolle, M., Neisius, T., Meyer-Klaucke, W., and Dau, H. (2005). Structural and oxidation state changes of the photosystem II manganese complex in four transitions of the water oxidation cycle (S₀ → S₁, S₁ → S₂, S₂ → S₃, and S_{3,4} → S₀) characterized by X-ray absorption spectroscopy at 20 K and room temperature. *Biochemistry*, 44(6):1894–1908.
- Haumann, M., Pospíšil, P., Grabolle, M., Müller, C., Liebisch, P., Solé, V. A., Neisius, T., Dittmer, J., Iuzzolino, L., and Dau, H. (2002b). First steps towards time-resolved BioXAS at room temperature: state transitions of the manganese complex of oxygenic photosynthesis. *J. of Synchrotron Radiat.*, 9(Pt 5):304–308.
- Herrero, C., Lassalle-Kaiser, B., Leibl, W., Rutherford, A. W., and Aukauloo, A. (2008). Artificial systems related to light driven electron transfer processes in PSII. *Coord. Chem. Rev.*, 252(3-4):456–468.

- Hillier, W. and Babcock, G. T. (2001). S-state dependent fourier transform infrared difference spectra for the photosystem II oxygen evolving complex. *Biochemistry*, 40(6):1503–1509.
- Hillier, W., Hendry, G., Burnap, R. L., and Wydrzynski, T. (2001). Substrate water exchange in photosystem II depends on the peripheral proteins. *J. Biol. Chem.*, 276(50):46917–46924.
- Hillier, W., Messinger, J., and Wydrzynski, T. (1998). Kinetic determination of the fast exchanging substrate water molecule in the S₃ state of photosystem II. *Biochemistry*, 37(48):16908–16914.
- Hillier, W. and Wydrzynski, T. (2000). The affinities for the two substrate water binding sites in the O₂ evolving complex of photosystem II vary independently during S-state turnover. *Biochemistry*, 39(15):4399–4405.
- Hillier, W. and Wydrzynski, T. (2001). Oxygen ligand exchange at metal sites—implications for the O₂ evolving mechanism of photosystem II. *Biochim. Biophys. Acta*, 1503(1-2):197–209.
- Hillier, W. and Wydrzynski, T. (2004). Substrate water interactions within the photosystem II oxygen evolving complex. *Phys. Chem. Chem. Phys.*, 6(20):4882–4889.
- Hillier, W. and Wydrzynski, T. (2008). ¹⁸O-Water exchange in photosystem II: substrate binding and intermediates of the water splitting cycle. *Coord. Chem. Rev.*, 252(3-4):306–317.
- Hoganson, C. W. and Babcock, G. T. (1997). A metalloradical mechanism for the generation of oxygen from water in photosynthesis. *Science*, 277(5334):1953–1956.
- Hoganson, C. W., Lydak-Simantiris, N., Tang, X. S., Tommos, C., Warncke, K., Babcock, G. T., Diner, B. A., McCracken, J., and Styring, S. (1995). A hydrogen-atom abstraction model for the function of Y_Z in photosynthetic oxygen-evolution. *Photosynth. Res.*, 46(1-2):177–184.
- Ioannidis, N., Nugent, J. H. A., and Petrouleas, V. (2002). Intermediates of the S₃ state of the oxygen-evolving complex of photosystem II. *Biochemistry*, 41(30):9589–9600.
- Iuzzolino, L., Dittmer, J., Dörner, W., Meyer-Klaucke, W., and Dau, H. (1998). X-ray absorption spectroscopy on layered photosystem II membrane particles suggests manganese-centered oxidation of the oxygen-evolving complex for the S₀-S₁, S₁-S₂, and S₂-S₃ transitions of the water oxidation cycle. *Biochemistry*, 37(49):17112–17119.

References

- Kamiya, N. and Shen, J. R. (2003). Crystal structure of oxygen-evolving photosystem II from thermosynechococcus vulcanus at 3.7-Å resolution. *Proc. Natl. Acad. Sci. U. S. A.*, 100(1):98–103.
- Kawakami, K., Umena, Y., Kamiya, N., and Shen, J. R. (2009). Location of chloride and its possible functions in oxygen-evolving photosystem II revealed by X-ray crystallography. *Proc. Natl. Acad. Sci. U. S. A.*, 106(21):8567–8572.
- Klein, M. P., Sauer, K., and Yachandra, V. K. (1993). Perspectives on the structure of the photosynthetic oxygen evolving manganese complex and its relation to the Kok cycle. *Photosynth. Res.*, 38(3):265–277.
- Kok, B., Forbush, B., and McGloin, M. (1970). Cooperation of charges in photosynthetic O₂ evolution – I. A linear four-step mechanism. *Photochem. and Photobiol.*, 11:457–475.
- Koningsberger, D. C. and Prins, R., editors (1988). *X-Ray Absorption: Principles, Applications, Techniques of EXAFS, SEXAFS and XANES*, volume 92 of *Chemical Analysis*. John Wiley & Sons, New York/Chichester/Brisbane/Toronto/Singapore.
- Kulik, L. V., Epel, B., Lubitz, W., and Messinger, J. (2005). ⁵⁵Mn pulse ENDOR at 34 GHz of the S₀ and S₂ states of the oxygen-evolving complex in photosystem II. *J. Am. Chem. Soc.*, 127(8):2392–2393.
- Lewis, N. S. and Nocera, D. G. (2006). Powering the planet: chemical challenges in solar energy utilization. *Proc. Natl. Acad. Sci. U. S. A. of America*, 103(43):15729–15735.
- Liang, W., Latimer, M. J., Dau, H., Roelofs, T. A., Yachandra, V. K., Sauer, K., and Klein, M. P. (1994). Correlation between structure and magnetic spin state of the manganese cluster in the oxygen-evolving complex of photosystem II in the S₂ state: determination by X-ray absorption spectroscopy. *Biochemistry*, 33(16):4923–4932.
- Loll, B., Kern, J., Saenger, W., Zouni, A., and Biesiadka, J. (2005). Towards complete cofactor arrangement in the 3.0 Å resolution structure of photosystem II. *Nature*, 438(7070):1040–1044.
- Lourakis, M. (2004). levmar: Levenberg-marquardt nonlinear least squares algorithms in C/C++. <http://www.ics.forth.gr/~lourakis/levmar/>.
- Lubitz, W., Reijerse, E. J., and Messinger, J. (2008). Solar water-splitting into H₂ and O₂: design principles of photosystem II and hydrogenases. *Energy Environ. Sci.*, 1(1):15–31.

- MacLachlan, D. J., Hallahan, B. J., Ruffle, S. V., Nugent, J. H., Evans, M. C., Strange, R. W., and Hasnain, S. S. (1992). An E.X.A.F.S. study of the manganese O₂-evolving complex in purified photosystem II membrane fractions. The S₁ and S₂ states. *Biochem. J.*, 285:569–576.
- McDermott, A. E., Yachandra, V. K., Guiles, R. D., Cole, J. L., Dexheimer, S. L., Britt, R. D., Sauer, K., and Klein, M. P. (1988). Characterization of the manganese O₂-evolving complex and the iron-quinone acceptor complex in photosystem II from a thermophilic cyanobacterium by electron paramagnetic resonance and X-ray absorption spectroscopy. *Biochemistry*, 27(11):4021–4031.
- McEvoy, J. P. and Brudvig, G. W. (2006). Water-splitting chemistry of photosystem II. *Chem. Rev.*, 106(11):4455–4483.
- McEvoy, J. P., Gascón, J. A., Batista, V. S., and Brudvig, G. W. (2005). The mechanism of photosynthetic water splitting. *Photobiol. Sci.*, 4(12):940–949.
- Meinke, C., Solé, V. A., Pospíšil, P., and Dau, H. (2000). Does the structure of the water-oxidizing photosystem II-manganese complex at room temperature differ from its low-temperature structure? A comparative X-ray absorption study. *Biochemistry*, 39(24):7033–7040.
- Messinger, J., Badger, M., and Wydrzynski, T. (1995). Detection of *one* slowly exchanging substrate water molecule in the S₃ state of photosystem II. *Proc. Natl. Acad. Sci. U. S. A.*, 92(8):3209–3213.
- Messinger, J., Schröder, W. P., and Renger, G. (1993). Structure-function relations in photosystem II. effects of temperature and chaotropic agents on the period four oscillation of flash-induced oxygen evolution. *Biochemistry*, 32(30):7658–7668.
- Miller, A. F. and Brudvig, G. W. (1991). A guide to electron paramagnetic resonance spectroscopy of photosystem II membranes. *Biochim. Biophys. Acta*, 1056(1):1–18.
- Mukerji, I., Andrews, J. C., DeRose, V. J., Latimer, M. J., Yachandra, V. K., Sauer, K., and Klein, M. P. (1994). Orientation of the oxygen-evolving manganese complex in a photosystem II membrane preparation: an X-ray absorption spectroscopy study. *Biochemistry*, 33(32):9712–9721.
- Müller, C. (2006). *Methodenentwicklung und Durchführung fortgeschrittener Röntgenabsorptionsmessungen am Mangan-Calcium-Komplex des Photosystems II*. PhD thesis, Freie Universität Berlin.
- Müller, C., Liebisch, P., Barra, M., Dau, H., and Haumann, M. (2005). The location of calcium in the manganese complex of oxygenic photosynthesis studied by X-ray absorption spectroscopy at the Ca K-edge. *Physica Scripta*, 2005(T115):847.

References

- Murray, J., Maghlaoui, K., Kargul, J., Ishida, N., Lai, T.-L., Rutherford, A., Sugiura, M., Boussac, A., and Barber, J. (2008). X-ray crystallography identifies two chloride binding sites in the oxygen evolving centre of photosystem II. *Energy Environ. Sci.*, 1:161–166.
- Mustre de Leon, J., Rehr, J. J., Zabinsky, S. I., and Albers, R. C. (1991). Ab initio curved-wave x-ray-absorption fine structure. *Phys. Rev. B*, 44(9):4146–4156.
- Newville, M. (2004). *The IFEFFIT Reference Guide*. Consortium for Advanced Radiation Sources, University of Chicago, Chicago, USA.
- Newville, M. (2008). *Fundamentals of XAFS*. Consortium for Advanced Radiation Sources, University of Chicago, Chicago, USA.
- Noguchi, T. (2008). Fourier transform infrared analysis of the photosynthetic oxygen-evolving center. *Coord. Chem. Rev.*, 252(3-4):336–346.
- Olesen, K. and Andreasson, L. E. (2003). The function of the chloride ion in photosynthetic oxygen evolution. *Biochemistry*, 42(7):2025–35.
- Ort, D. and Yocum, C. (1996). *Oxygenic Photosynthesis: The Light Reactions*, volume 10 of *Advances in photosynthesis*. Kluwer Academic Publ., Dordrecht.
- Pace, R. J., Smith, P., Bramley, R., and Stehlik, D. (1991). EPR saturation and temperature dependence studies on signals from the oxygen-evolving center of photosystem II. *Biochim. Biophys. Acta*, 1058(2):161–170.
- Pantazis, D. A., Orio, M., Petrenko, T., Zein, S., Lubitz, W., Messinger, J., and Neese, F. (2009). Structure of the oxygen-evolving complex of photosystem II: information on the S₂ state through quantum chemical calculation of its magnetic properties. *Phys. Chem. Chem. Phys.*, 11:6788–6798.
- Peloquin, J. M., Campbell, K. A., Randall, D. W., Evanchik, M. A., Pecoraro, V. L., Armstrong, W. H., and Britt, R. D. (2000). ⁵⁵Mn ENDOR of the S₂-state multiline EPR signal of photosystem II: implications on the structure of the tetranuclear Mn cluster. *J. Am. Chem. Soc.*, 122(44):10926–10942.
- Penner-Hahn, J. E. (1998). Structural characterization of the Mn site in the photosynthetic oxygen-evolving complex. In Hill, H. A. O., Sadler, P. J., and Thomson, A. J., editors, *Metal Sites in Proteins and Models Redox Centres*, volume 90 of *Structure & Bonding*, pages 1–36. Springer, Berlin/Heidelberg, Germany.
- Pospíšil, P., Haumann, M., Dittmer, J., Solé, V. A., and Dau, H. (2003). Stepwise transition of the tetra-manganese complex of photosystem II to a binuclear Mn₂(μ-O)₂ complex in response to a temperature jump: a timeresolved structural investigation employing X-ray absorption spectroscopy. *Biophys. J.*, 84:1370–1386.

- Pushkar, Y., Yano, J., Glatzel, P., Messinger, J., Lewis, A., Sauer, K., Bergmann, U., and Yachandra, V. (2007). Structure and orientation of the Mn₄Ca cluster in plant photosystem II membranes studied by polarized range-extended X-ray absorption spectroscopy. *J. Biol. Chem.*, 282(10):7198–7208.
- Rappaport, F. and Diner, B. A. (2008). Primary photochemistry and energetics leading to the oxidation of the (Mn)₄Ca cluster and to the evolution of molecular oxygen in photosystem II. *Coord. Chem. Rev.*, 252(3-4):259–272.
- Rappaport, F., Guergova-Kuras, M., Nixon, P. J., Diner, B. A., and Lavergne, J. (2002). Kinetics and pathways of charge recombination in photosystem II. *Biochemistry*, 41:8518–8527.
- Rehder, D., Schulzke, C., Dau, H., Meinke, C., Hanss, J., and Epple, M. (2000). Water and bromide in the active center of vanadate-dependent haloperoxidases. *J. Inorg. Biochem.*, 80(1-2):115–121.
- Rehr, J. J. and Albers, R. C. (2000). Theoretical approaches to x-ray absorption fine structure. *Rev. Mod. Phys.*, 72(3):621–654.
- Risch, M., Khare, V., Grundmeier, A., Sanganas, O., Gerencsér, L., Zaharieva, I., Löscher, S., Chernev, P., Haumann, M., and Dau, H. (2008). Characterization of a novel water-oxidizing cobalt catalyst by X-ray absorption spectroscopy. *BESSY Annual Report 2008*, pages 68–69.
- Robblee, J. H., Messinger, J., Cinco, R. M., McFarlane, K. L., Fernandez, C., Pizarro, S. A., Sauer, K., and Yachandra, V. K. (2002). The Mn cluster in the S₀ state of the oxygen-evolving complex of photosystem II studied by EXAFS spectroscopy: Are there three di-μ-oxo-bridged Mn₂ moieties in the tetranuclear Mn complex? *J. Am. Chem. Soc.*, 124(25):7459–7471.
- Roy, M., Lindsay, J. D., Louch, S., and Gurman, S. J. (2001). Multiple-electron excitation in X-ray absorption: a simple generic model. *J. of Synchrotron Radiat.*, 8(4):1103–1108.
- Rutherford, A. W. and Moore, T. A. (2008). Mimicking photosynthesis, but just the best bits. *Nature*, 453(7194):449.
- Rüttinger, W. and Dismukes, G. (1997). Synthetic water-oxidation catalysts for artificial photosynthetic water oxidation. *Chem. Rev.*, 97(1):1–24.
- Sanganas, O., Grundmeier, A., Risch, M., Zaharieva, I., Chernev, P., Khare, V., Weyhermüller, T., Wieghardt, K., Voevodskaya, N., Gräslund, A., Stripp, S., Happe, T., Dau, H., and Haumann, M. (2008). X-ray absorption spectroscopy investigations on binuclear metal sites in proteins and models at the Mn and Fe K-edges. *BESSY Annual Report 2008*, pages 405–406.

References

- Sauer, K., Yachandra, V. K., Britt, R. D., and Klein, M. P. (1992). The photosynthetic water oxidation complex studied by EPR and X-ray absorption spectroscopy. In Pecoraro, V. L., editor, *Manganese Redox Enzymes*, page Chapter 8. VCH, New York, N.Y.
- Sauer, K., Yano, J., and Yachandra, V. K. (2005). X-ray spectroscopy of the Mn₄Ca cluster in the water-oxidation complex of photosystem II. *Photosynth. Res.*, 85(1):73–86.
- Sauer, K., Yano, J., and Yachandra, V. K. (2008). X-ray spectroscopy of the photosynthetic oxygen-evolving complex. *Coord. Chem. Rev.*, 252(3-4):318–335.
- Sayers, D. E., Lytle, F. W., Weissbluth, M., and Pianetta, P. (1975). A short range probe for investigating metalloprotein structures: Fourier analysis of the extended x-ray absorption fine structure. *J. Chem. Phys.*, 62(6):2514–2515.
- Schiller, H. and Dau, H. (2000). Preparation protocols for high-activity photosystem II membrane particles of green algae and higher plants, pH dependence of oxygen evolution and comparison of the S₂-state multiline signal by X-band EPR spectroscopy. *J. Photochem. Photobiol. B*, 55(2-3):138–144.
- Schiller, H., Dittmer, J., Iuzzolino, L., Dörner, W., Meyer-Klaucke, W., Solé, V. A., Nolting, H., and Dau, H. (1998). Structure and orientation of the oxygen-evolving manganese complex of green algae and higher plants investigated by X-ray absorption linear dichroism spectroscopy on oriented photosystem II membrane particles. *Biochemistry*, 37(20):7340–7350.
- Siegbahn, P. E. M. (2008). A structure-consistent mechanism for dioxygen formation in photosystem II. *Chem. Eur. J.*, 14(27):8290–8302.
- Siegbahn, P. E. M. (2009). Structures and energetics for O₂ formation in photosystem II. *Acc. Chem. Res.*, 42(12):1871–1880.
- Sproviero, E. M., Gascón, J. A., McEvoy, J. P., Brudvig, G. W., and Batista, V. S. (2006). QM/MM models of the O₂-evolving complex of photosystem II. *J. Chem. Theory Comput.*, 2(4):1119–1134.
- Sproviero, E. M., Gascón, J. A., McEvoy, J. P., Brudvig, G. W., and Batista, V. S. (2007). Quantum mechanics/molecular mechanics structural models of the oxygen-evolving complex of photosystem II. *Curr. Opin. Struct. Biol.*, 17(2):173–180.
- Sproviero, E. M., Gascón, J. A., McEvoy, J. P., Brudvig, G. W., and Batista, V. S. (2008a). Computational studies of the O₂-evolving complex of photosystem II and biomimetic oxomanganese complexes. *Coord. Chem. Rev.*, 252(3-4):395–415.

- Sproviero, E. M., Gascón, J. A., McEvoy, J. P., Brudvig, G. W., and Batista, V. S. (2008b). A model of the oxygen-evolving center of photosystem II predicted by structural refinement based on EXAFS simulations. *J. Am. Chem. Soc.*, 130(21):6728–6730.
- Sproviero, E. M., Gascón, J. A., McEvoy, J. P., Brudvig, G. W., and Batista, V. S. (2008c). Quantum mechanics/molecular mechanics study of the catalytic cycle of water splitting in photosystem II. *J. Am. Chem. Soc.*, 130(11):3428–3442.
- Sproviero, E. M., McEvoy, J. P., Gascón, J. A., Brudvig, G. W., and Batista, V. S. (2008d). Computational insights into the O₂-evolving complex of photosystem II. *Photosynth. Res.*, 97(1):91–114.
- Sproviero, E. M., Shinopoulos, K., Gascón, J. A., McEvoy, J. P., Brudvig, G. W., and Batista, V. S. (2008e). QM/MM computational studies of substrate water binding to the oxygen-evolving centre of photosystem II. *Philos. Trans. R. Soc. London, Ser. B*, 363(1494):1149–1156.
- Stöhr, J. (1992). *NEXAFS Spectroscopy*, volume 25 of *Springer Series in Surface Sciences*. Springer, Berlin/Heidelberg, Germany.
- Styring, S. and Rutherford, A. W. (1987). In the oxygen-evolving complex of photosystem II the S₀ state is oxidized to the S₁ state by D⁺ (signal II_{slow}). *Biochemistry*, 26(9):2401–2405.
- Styring, S. and Rutherford, A. W. (1988). Deactivation kinetics and temperature dependence of the S-state transitions in the oxygen-evolving system of photosystem II measured by EPR spectroscopy. *Biochim. Biophys. Acta*, 933(2):378 – 387.
- Sun, L. C., Raymond, M. K., Magnuson, A., LeGourrierec, D., Tamm, M., Abrahamson, M., Kenez, P. H., Martensson, J., Stenhagen, G., Hammarström, L., Styring, S., and Akermark, B. (2000). Towards an artificial model for photosystem II: a manganese(II,II) dimer covalently linked to ruthenium(II) tris-bipyridine via a tyrosine derivative. *J. of Inorg. Bioch.*, 78(1):15–22.
- Suzuki, H., Sugiura, M., and Noguchi, T. (2005). pH dependence of the flash-induced S-state transitions in the oxygen-evolving center of photosystem II from *Thermosynechococcus elongatus* as revealed by Fourier transform infrared spectroscopy. *Biochemistry*, 44(5):1708–1718.
- Tagore, R., Chen, H., Crabtree, R. H., and Brudvig, G. W. (2006). Determination of μ -oxo exchange rates in di- μ -oxo dimanganese complexes by electrospray ionization mass spectrometry. *J. Am. Chem. Soc.*, 128(29):9457–65.

References

- Tagore, R., Chen, H., Zhang, H., Crabtree, R. H., and Brudvig, G. W. (2007). Homogeneous water oxidation by a di- μ -oxo dimanganese complex in the presence of Ce^{4+} . *Inorg. Chim. Acta*, 360(9):2983–2989.
- Tarini, M., Cignoni, P., and Montani, C. (2006). Ambient occlusion and edge cueing for enhancing real time molecular visualization. *IEEE Transactions on Visualization and Computer Graphics*, 12(5):1237–1244.
- Teo, B. K. (1986). *EXAFS: Basic Principles and Data Analysis*. Springer, Berlin/Heidelberg, Germany.
- Teo, B. K. and Joy, D. C., editors (1981). *EXAFS Spectroscopy*. Plenum Press, New York, USA.
- Teutloff, C., Pudollek, S., Kessen, S., Broser, M., Zouni, A., and Bittl, R. (2009). Electronic structure of the tyrosine D radical and the water-splitting complex from pulsed ENDOR spectroscopy on photosystem II single crystals. *Phys. Chem. Chem. Phys.*, 11(31):6715–26.
- Tommos, C. and Babcock, G. T. (1998). Oxygen production in nature: a light-driven metalloradical enzyme process. *Acc. Chem. Res.*, 31(1):18–25.
- Tommos, C., Hoganson, C. W., Di Valentin, M., Lydakis-Simantiris, N., Dorlet, P., Westphal, K., Chu, H. A., McCracken, J., and Babcock, G. T. (1998). Manganese and tyrosyl radical function in photosynthetic oxygen evolution. *Curr. Opin. in Chem. Biol.*, 2(2):244–252.
- Tukey, J. W. (1967). An introduction to the calculations of numerical spectrum analysis. In Harris, B., editor, *Spectral Analysis of Time Series*, pages 25–46, New York/London/Sydney. John Wiley & Sons.
- Umena, Y., Kawakami, K., Shen, J. R., and Kamiya, N. (2011). Crystal structure of oxygen-evolving photosystem II at a resolution of 1.9 Å. *Nature*, 473(7345):55–60.
- Vincent, J. B. and Christou, G. (1987). A molecular double-pivot mechanism for water oxidation. *Inorg. Chim. Acta*, 136(3):L41–L43.
- Voevodskaya, N., Lenzian, F., Sanganas, O., Grundmeier, A., Gräslund, A., and Haumann, M. (2009). Redox intermediates of the Mn-Fe Site in subunit R2 of *Chlamydia trachomatis* ribonucleotide reductase: an X-ray absorption and EPR study. *J. Biol. Chem.*, 284(7):4555–4566.
- Yachandra, V. K., DeRose, V. J., Latimer, M. J., Mukerji, I., Sauer, K., and Klein, M. P. (1993). Where plants make oxygen: a structural model for the photosynthetic oxygen-evolving manganese cluster. *Science*, 260(5108):675–679.

- Yachandra, V. K., Guiles, R. D., McDermott, A., Britt, R. D., Dexheimer, S. L., Sauer, K., and Klein, M. P. (1986). The state of manganese in the photosynthetic apparatus. 4. Structure of the manganese complex in photosystem II studied using EXAFS spectroscopy. The S₁ state of the O₂-evolving photosystem II complex from spinach. *Biochim. Biophys. Acta*, 850:324–332.
- Yachandra, V. K., Sauer, K., and Klein, M. P. (1996). Manganese cluster in photosynthesis: Where plants oxidize water to dioxygen. *Chem. Rev.*, 96(7):2927–2950.
- Yamanari, T., Kimura, Y., Mizusawa, N., Ishii, A., and Ono, T.-A. (2004). Mid- to low-frequency fourier transform infrared spectra of S-state cycle for photosynthetic water oxidation in *Synechocystis* sp. PCC 6803. *Biochemistry*, 43(23):7479–7490.
- Yano, J., Kern, J., Irrgang, K. D., Latimer, M. J., Bergmann, U., Glatzel, P., Pushkar, Y., Biesiadka, J., Loll, B., Sauer, K., Messinger, J., Zouni, A., and Yachandra, V. K. (2005a). X-ray damage to the Mn₄Ca complex in single crystals of photosystem II: a case study for metalloprotein crystallography. *Proc. Natl. Acad. Sci. U. S. A.*, 102(34):12047–12052.
- Yano, J., Kern, J., Sauer, K., Latimer, M. J., Pushkar, Y., Biesiadka, J., Loll, B., Saenger, W., Messinger, J., Zouni, A., and Yachandra, V. K. (2006). Where water is oxidized to dioxygen: structure of the photosynthetic Mn₄Ca cluster. *Science*, 314(5800):821–825.
- Yano, J., Pushkar, Y., Glatzel, P., Lewis, A., Sauer, K., Messinger, J., Bergmann, U., and Yachandra, V. (2005b). High-resolution Mn EXAFS of the oxygen-evolving complex in photosystem II: structural implications for the Mn₄Ca cluster. *J. Am. Chem. Soc.*, 127(43):14974–14975.
- Yocum, C. F. and Pecoraro, V. L. (1999). Recent advances in the understanding of the biological chemistry of manganese. *Curr. Opin. Chem. Biol.*, 3(2):182–187.
- Zaharieva, I., Wichmann, J. M., and Dau, H. (2011). Thermodynamic limitations of photosynthetic water oxidation at high proton concentrations. *J. Biol. Chem.*
- Zouni, A., Witt, H. T., Kern, J., Fromme, P., Krauss, N., Saenger, W., and Orth, P. (2001). Crystal structure of photosystem II from *Synechococcus elongatus* at 3.8 Å resolution. *Nature*, 409(6821):739–743.

Copyright

For all figures and tables with remark “Table/Figure from Grundmeier and Dau [2012].” or “Table/Figure adapted from Grundmeier and Dau [2012].”:

Reprinted from Grundmeier, A. and Dau, H. (2012). Structural models of the manganese complex of photosystem II and mechanistic implications. *Biochim. Biophys. Acta*, 1817(1):88–105, Copyright 2012, with permission from Elsevier.

A. Appendix

A.1. Average angle to unit cell axes for PSII crystal

In the following it is shown that due to the symmetry properties of the PSII crystal, only one dimer has to be considered when calculating the average angle $\bar{\theta}_{R,i}$ for one shell used in Eq. (4.5). As outlined below, the specific symmetry of $P2_12_12_1$ also allows generalization of the LD-EXAFS theory.

The space group of the PSII crystal is $P2_12_12_1$. With a , b , and c being the dimension of the unit cell ($a \approx 122 \text{ \AA}$, $b \approx 228 \text{ \AA}$, and $c \approx 286 \text{ \AA}$; see XRD structure 3ARC from Umena et al. [2011]) and given the position x_1 of an atom in the first PSII dimer, the coordinates x_2, x_3, x_4 of the equivalent atoms in the other three dimers can be calculated as:

$$x_2 = \begin{pmatrix} -1 & 0 & 0 \\ 0 & -1 & 0 \\ 0 & 0 & 1 \end{pmatrix} x_1 + \frac{1}{2} \begin{pmatrix} a \\ 0 \\ c \end{pmatrix} \quad (\text{A.1a})$$

$$x_3 = \begin{pmatrix} -1 & 0 & 0 \\ 0 & 1 & 0 \\ 0 & 0 & -1 \end{pmatrix} x_1 + \frac{1}{2} \begin{pmatrix} 0 \\ b \\ c \end{pmatrix} \quad (\text{A.1b})$$

$$x_4 = \begin{pmatrix} 1 & 0 & 0 \\ 0 & -1 & 0 \\ 0 & 0 & -1 \end{pmatrix} x_1 + \frac{1}{2} \begin{pmatrix} a \\ b \\ 0 \end{pmatrix} \quad (\text{A.1c})$$

The angles θ_{i1} (with $i = 1, 2, 3$) between an absorber-backscatterer binding vector $v_1 = (v_{11}, v_{12}, v_{13})^t$ and the crystal axes

$$e_1 = (1, 0, 0)^t, \quad e_2 = (0, 1, 0)^t, \quad e_3 = (0, 0, 1)^t \quad (\text{A.2})$$

are given by

$$\cos \theta_{i1} = \frac{v_1 e_i}{|v_1|} = \frac{v_{1i}}{|v_1|}. \quad (\text{A.3})$$

With this, the angles θ_{i2} , θ_{i3} , and θ_{i4} for the equivalent binding vectors (resulting from Eq. (A.1)),

$$v_2 = (-v_{11}, -v_{12}, +v_{13})^t \quad (\text{A.4a})$$

$$v_3 = (-v_{11}, +v_{12}, -v_{13})^t \quad (\text{A.4b})$$

A. Appendix

$$v_4 = (+v_{11}, -v_{12}, -v_{13})^t, \quad (\text{A.4c})$$

in the other three dimers can be written as

$$\cos \theta_{ij} = \frac{v_j e_i}{|v_j|} = \frac{v_{ji}}{|v_j|} = \frac{v_{1i}}{|v_1|} \epsilon_{ij} \quad (\text{A.5})$$

with

$$\epsilon_{ij} := \begin{cases} +1 & \text{if } i + j = 5, \\ -1 & \text{else.} \end{cases} \quad (\text{A.6})$$

The index $i = 1, 2, 3$ is again representing the crystal axis, and the index $j = 2, 3, 4$ expresses the considered dimer.

Equation (A.5) implies that the values $\cos^2 \theta_{ij}$ for all dimers j are identical. This property (in combination with $\sum_{j=1}^4 v_j = 0$) allows generalization of the LD-EXAFS theory as described in Section 1.2.4 and especially application of Eq. (1.23) to the case of $P2_12_12_1$ crystals.

Furthermore, it follows that the cosine squared of the average angle, $\bar{\theta}_i$, between one crystal axis, e_i , and all four equivalent binding vectors, v_1, v_2, v_3, v_4 , within the PSII unit cell is equal to the cosine squared of the angle θ_{ij} between e_i and v_j ($j = 2, 3, 4$):

$$\begin{aligned} \cos^2 \bar{\theta}_i &= \frac{1}{4} \left(\sum_{k=1}^4 \cos^2 \theta_{ik} \right) \\ &\stackrel{(\text{A.5})}{=} \frac{1}{4} \left(\sum_{k=1}^4 \cos^2 \theta_{ij} \right) \\ &= \cos^2 \theta_{ij} \end{aligned} \quad (\text{A.7})$$

Therefore, when calculating an EXAFS spectrum for a PSII crystal using Eq. (4.5), it is sufficient to determine the average angle $\bar{\theta}_{R,i}$ with the crystal axes for an absorber-backscatterer combination only for one of the four PSII dimers (i. e., only two angles have to be averaged, not eight).

A.2. Calculation of amplitude and phase functions using FEFF

A.2.1. General principle

For calculation of the amplitude and phase functions (in detail: $\lambda_i^{c/s}, f_i^{c/s}, \phi_i^{c/s}, \delta_i^{c/s}$) of a given absorber-backscatter vector v with FEFF the formula

$$\chi(k, \theta_{ER}) = \chi^c(k) \cos^2 \theta_{ER} + \chi^s(k) \sin^2 \theta_{ER} \quad (\text{A.8})$$

A.2. Calculation of amplitude and phase functions using FEFF

can be used. Here, the value θ_{ER} is the angle between the absorber-backscatterer and the electric-field vector, E .

Setting the E -field parallel to the vector v in FEFF (via POLARIZATION card), i. e., $\theta_{ER} = 0$, results in $\chi(k, \theta_{ER}) = \chi^c(k)$. Therefore, the $\lambda_i^c, f_i^c, \phi_i^c, \delta_i^c$ values are calculated by FEFF. Accordingly, with an E -field vector perpendicular to v ($\theta_{ER} = \pi/2$), one gets $\chi(k, \theta_{ER}) = \chi^s(k)$ and with this the $\lambda_i^s, f_i^s, \phi_i^s, \delta_i^s$ data.

A.2.2. Actual procedure

To calculate a set of phase/amplitude functions, a model of the manganese complex of PSII was used containing typical Mn-Mn, Mn-Ca, Mn-O, Mn-C, and Mn-N distances (`holgersModell1080710bPdb.xyz`). For this model, absorber-backscatterer vectors v were selected and a self-written Mathematica script (`calculate_phase_functions.nb`, see Fig. A.1 and its legend for a screenshot and brief description of the script) was utilized to automatically determine the according E -field vector for each v , write the file `feff.inp`, and start FEFF 8.4.

The parameters used within `feff.inp` (excluding the POLARIZATION card) were:

```
*          pot xsph fms path genfmt ff2chi
PRINT      0 0 0 0 0 3

SCF 6 1
DEBYE      20      410
* include MS paths with effective length up to 6 Ang
RPATH 6.00
* only single scattering paths (i.e., 2 legged paths)
NLEG 2
* use all paths (cw and pw criteria turned off)
CRITERIA 0 0

POTENTIALS
*      ipot z   label
      0  25   cMn
      1  25   Mn
      2   8    O
      3   8   mu0
      4  20   Ca
      5   6    C
      6   7    N
```

These parameters were given to the Mathematica script via a file named `header.txt`.

A.2.3. Phase/amplitude functions used

The following list shows the contents of a text file loaded by the program *EXAFS Calculations*. This file contains the names of the (for the calculations) used phase and amplitude functions files and prescribes, when to use them.

A. Appendix

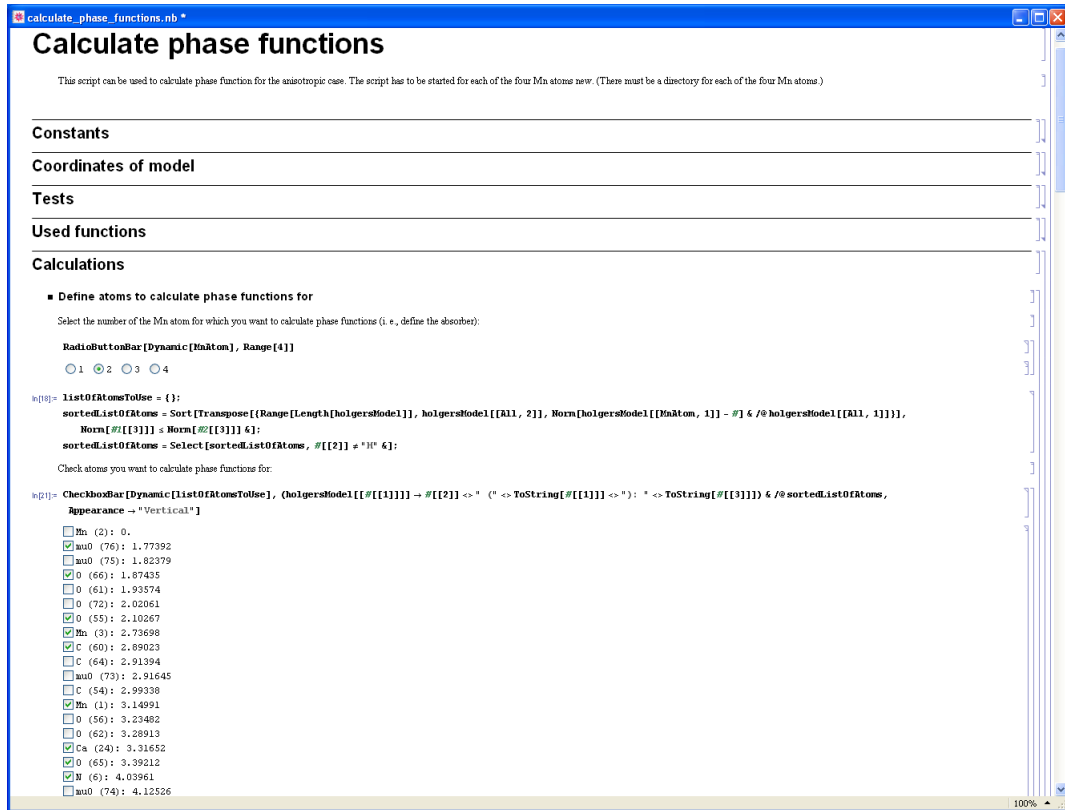


Figure A.1.:

Screenshot of the script `calculate_phase_functions.nb`. This Mathematica file calculates amplitude/phase functions (both sine and cosine part) for a given model. One of the manganese atoms has to be selected as the absorber via radio buttons. Based on this information, the according absorber-backscatter distances are displayed and the backscatteres can be chosen using check boxes. For each of defined absorber-backscatter combination defined in this way, the phase/amplitude functions are calculated with FEFF 8.4. *Remark:* A file named `header.txt` containing parameters for FEFF (see text) has to exist within the directory where the phase functions are to be stored.

A.2. Calculation of amplitude and phase functions using FEFF

Mn 0 2.72 MnMn2.70Cos.dat MnMn2.70Sin.dat
Mn 2.72 2.87 MnMn2.74Cos.dat MnMn2.74Sin.dat
Mn 2.87 3.075 MnMn3.00Cos.dat MnMn3.00Sin.dat
Mn 3.075 3.415 MnMn3.15Cos.dat MnMn3.15Sin.dat
Mn 3.415 4.025 MnMn3.68Cos.dat MnMn3.68Sin.dat
Mn 4.025 100 MnMn4.37Cos.dat MnMn4.37Sin.dat
Ca 0 3.595 MnCa3.32Cos.dat MnCa3.32Sin.dat
Ca 3.595 3.99 MnCa3.87Cos.dat MnCa3.87Sin.dat
Ca 3.99 100 MnCa4.11Cos.dat MnCa4.11Sin.dat
O 0 1.86 Mnmu01.82Cos.dat Mnmu01.82Sin.dat
O 1.86 1.91 Mnmu01.90Cos.dat Mnmu01.90Sin.dat
O 1.91 1.97 Mn01.92Cos.dat Mn01.92Sin.dat
O 1.97 2.04 Mn02.02Cos.dat Mn02.02Sin.dat
O 2.04 2.08 Mn02.06Cos.dat Mn02.06Sin.dat
O 2.08 2.39 Mn02.10Cos.dat Mn02.10Sin.dat
O 2.39 2.78 Mn02.68Cos.dat Mn02.68Sin.dat
O 2.78 3.01 Mn02.88Cos.dat Mn02.88Sin.dat
O 3.01 3.185 Mn03.14Cos.dat Mn03.14Sin.dat
O 3.185 3.26 Mn03.23Cos.dat Mn03.23Sin.dat
O 3.26 3.34 Mn03.29Cos.dat Mn03.29Sin.dat
O 3.34 3.48 Mn03.39Cos.dat Mn03.39Sin.dat
O 3.48 3.63 Mn03.57Cos.dat Mn03.57Sin.dat
O 3.63 3.78 Mn03.69Cos.dat Mn03.69Sin.dat
O 3.78 3.93 Mn03.87Cos.dat Mn03.87Sin.dat
O 3.93 4.04 Mn03.99Cos.dat Mn03.99Sin.dat
O 4.04 4.13 Mn04.09Cos.dat Mn04.09Sin.dat
O 4.13 4.24 Mn04.17Cos.dat Mn04.17Sin.dat
O 4.24 4.32 Mn04.31Cos.dat Mn04.31Sin.dat
O 4.32 4.365 Mn04.33Cos.dat Mn04.33Sin.dat
O 4.365 4.44 Mn04.40Cos.dat Mn04.40Sin.dat
O 4.44 4.58 Mn04.48Cos.dat Mn04.48Sin.dat
O 4.58 4.74 Mn04.68Cos.dat Mn04.68Sin.dat
O 4.74 4.85 Mn04.80Cos.dat Mn04.80Sin.dat
O 4.85 5.045 Mn04.90Cos.dat Mn04.90Sin.dat
O 5.045 5.26 Mn05.19Cos.dat Mn05.19Sin.dat
O 5.26 5.455 Mn05.33Cos.dat Mn05.33Sin.dat
O 5.455 5.595 Mn05.58Cos.dat Mn05.58Sin.dat
O 5.595 5.73 Mn05.61Cos.dat Mn05.61Sin.dat
O 5.73 100 Mn05.85Cos.dat Mn05.85Sin.dat
N 0 3. MnN2.19Cos.dat MnN2.19Sin.dat
N 3. 3.925 MnN3.81Cos.dat MnN3.81Sin.dat
N 3.925 4.145 MnN4.04Cos.dat MnN4.04Sin.dat
N 4.145 4.28 MnN4.25Cos.dat MnN4.25Sin.dat
N 4.28 4.34 MnN4.31Cos.dat MnN4.31Sin.dat
N 4.34 4.425 MnN4.37Cos.dat MnN4.37Sin.dat
N 4.425 4.575 MnN4.48Cos.dat MnN4.48Sin.dat
N 4.575 4.73 MnN4.67Cos.dat MnN4.67Sin.dat
N 4.73 4.82 MnN4.79Cos.dat MnN4.79Sin.dat
N 4.82 5.03 MnN4.85Cos.dat MnN4.85Sin.dat
N 5.03 5.545 MnN5.21Cos.dat MnN5.21Sin.dat

A. Appendix

```
N 5.545 100 MnN5.88Cos.dat MnN5.88Sin.dat
C 0 2.615 MnC2.54Cos.dat MnC2.54Sin.dat
C 2.615 2.8 MnC2.69Cos.dat MnC2.69Sin.dat
C 2.8 2.955 MnC2.91Cos.dat MnC2.91Sin.dat
C 2.955 3.095 MnC3.00Cos.dat MnC3.00Sin.dat
C 3.095 3.36 MnC3.19Cos.dat MnC3.19Sin.dat
C 3.36 3.57 MnC3.53Cos.dat MnC3.53Sin.dat
C 3.57 3.72 MnC3.61Cos.dat MnC3.61Sin.dat
C 3.72 4.01 MnC3.83Cos.dat MnC3.83Sin.dat
C 4.01 4.215 MnC4.19Cos.dat MnC4.19Sin.dat
C 4.215 4.395 MnC4.24Cos.dat MnC4.24Sin.dat
C 4.395 4.64 MnC4.55Cos.dat MnC4.55Sin.dat
C 4.64 4.78 MnC4.73Cos.dat MnC4.73Sin.dat
C 4.78 4.89 MnC4.83Cos.dat MnC4.83Sin.dat
C 4.89 4.99 MnC4.95Cos.dat MnC4.95Sin.dat
C 4.99 5.07 MnC5.03Cos.dat MnC5.03Sin.dat
C 5.07 5.19 MnC5.11Cos.dat MnC5.11Sin.dat
C 5.19 5.4 MnC5.27Cos.dat MnC5.27Sin.dat
C 5.4 5.65 MnC5.53Cos.dat MnC5.53Sin.dat
C 5.65 5.82 MnC5.77Cos.dat MnC5.77Sin.dat
C 5.82 5.9 MnC5.87Cos.dat MnC5.87Sin.dat
C 5.9 100 MnC5.93Cos.dat MnC5.93Sin.dat
```

The first column displays the backscatterer, the second and third one show the distance region for which the files mentioned in the fourth and fifth column should be used. Such a list can also be generated using the script `calculate_phase_functions.nb`.

A.3. Formal oxidation states derived from Mn-O bond lengths

For the Mn ions of the XRD results from Umena et al. [2011], formal oxidation states were calculated using the bond-valence method described, e. g., in Brese and O’Keeffe [1991].

The *valence* (or *oxidation state*), V , of an atom can be written as a sum of so called *bond valences*, v_i , of the bonds between this atom and all N bound atoms:¹

$$V = \sum_{i=1}^N v_i \quad (\text{A.9})$$

A bond valence, v_i , can be calculated from the according bond length R_i using two empirical parameters b and $R_{i,0}$:

$$v_i = e^{(R_{i,0}-R_i)/b} \quad (\text{A.10})$$

The parameter b is typically chosen as 0.37 \AA (also in this thesis) as derived by Brown and Altermatt [1985]. The parameter $R_{i,0}$ is called *bond-valence parameter*.

¹The terms *oxidation state* and *valence* are used equivalently in this context.

A.4. Program for calculation of EXAFS spectra

Table A.1.:

Lengths R of Mn-O bonds calculated with Eq. (A.11) in dependence of the coordination number N of the central Mn atom and the valence (or oxidation state) V . Values for bond-valence parameters R_0 from Table 2 of Brese and O’Keeffe [1991]. Table adapted from Grundmeier and Dau [2012].

N [1]	V [1]	R_0 [Å]	R [Å]
5	2	1.79	2.13
5	3	1.76	1.95
5	4	1.753	1.84
6	2	1.79	2.20
6	3	1.76	2.02
6	4	1.753	1.90

With these formulas, it is possible to calculate the expected bond lengths based on the number of ligating atoms and the oxidation state of the central atom, assuming that (i) for all bound atoms the bond length R is the same and (ii) all bound atoms are of the same kind (resulting in a bond-valence parameter R_0 independent from i):

$$\begin{aligned}
 V &= \sum_{i=1}^N e^{(R_0-R)/b} \\
 &= N e^{(R_0-R)/b} \\
 \Rightarrow R &= R_0 - b \ln \frac{V}{N}
 \end{aligned} \tag{A.11}$$

Using the values for the bond-valence parameters R_0 from Table 2 of Brese and O’Keeffe [1991] and Eq. (A.11), the results presented in Table A.1 can be calculated for Mn-O bonds. The bond-valence parameter R_0 itself depends on the valence of the central atom.

Calculating the average bond lengths for the Mn ions from the XRD data 3ARC and the values for R from Table A.1, it is possible to derive fractional oxidation states for the Mn ions using linear interpolation. The result is presented in Table 5.3. The Mn¹ ion is assumed to be five-coordinated ($N = 5$) and all other Mn ions six-coordinated ($N = 6$).

A.4. Program for calculation of EXAFS spectra

For calculation of the EXAFS spectra and optimization of the models of the Mn complex as described in Chapter 4, a self-written program, mostly programmed in C++ using Microsoft Visual Studio 2008, was used. In the following, this program—called *EXAFS Calculations*—is introduced and the main features are highlighted.

A. Appendix

Atom	x_1 [Å]	x_2 [Å]	x_3 [Å]	R_min [Å]
<input checked="" type="checkbox"/> Mn1	-0.806207	-19.9584	16.194	0
<input checked="" type="checkbox"/> Mn2	-3.24154	-20.4665	15.1375	0
<input checked="" type="checkbox"/> Mn3	-3.30909	-18.1803	16.642	0
<input checked="" type="checkbox"/> Mn4	-1.40608	-16.3	15.6951	0
<input checked="" type="checkbox"/> Ca5	-2.21649	-18.4035	13.1291	3.0562014...
<input checked="" type="checkbox"/> N6	2.30957	-20.3571	19.0905	4.2727906...
<input checked="" type="checkbox"/> N7	0.519187	-19.4816	17.5643	1.9651283...
<input checked="" type="checkbox"/> N8	0.907213	-17.1571	21.7614	6.4636702...
<input checked="" type="checkbox"/> N9	-2.66578	-26.8559	15.9178	6.4625691...
<input checked="" type="checkbox"/> N10	-4.59044	-25.4278	13.9384	5.2793815...
<input checked="" type="checkbox"/> N11	-5.15456	-22.7948	12.6556	3.9039024...
<input checked="" type="checkbox"/> N12	-3.45816	-19.4715	9.44273	5.7850976...
<input checked="" type="checkbox"/> N13	-4.6408	-12.4507	12.8734	5.7656322...
<input checked="" type="checkbox"/> N14	-2.53751	-21.6806	21.2594	5.6233139...
<input checked="" type="checkbox"/> N15	-2.77934	-21.7685	19.1242	3.9693561...
<input checked="" type="checkbox"/> N16	-8.70744	-17.4266	13.4566	6.3132416...
<input checked="" type="checkbox"/> N17	-6.85328	-17.617	12.1591	5.4804363...
<input checked="" type="checkbox"/> N18	-6.63597	-16.6338	14.2081	4.4026880...
<input checked="" type="checkbox"/> N19	1.57245	-18.268	21.4818	6.0395604...
<input checked="" type="checkbox"/> N20	3.2301	-18.0736	19.663	5.6460788...
<input checked="" type="checkbox"/> N21	2.30541	-18.9874	18.9224	4.2507843...
<input checked="" type="checkbox"/> N22	1.32608	-18.4945	18.0033	3.1564564...
<input checked="" type="checkbox"/> N23	1.20805	-20.4833	18.2663	2.9372059...
<input checked="" type="checkbox"/> N24	-0.503511	-17.1525	22.0842	6.2084770...
<input checked="" type="checkbox"/> N25	-1.28399	-17.4411	20.7978	4.6816792...
<input checked="" type="checkbox"/> N26	-1.43999	-16.246	19.873	4.1793909...

Figure A.2.:

Screenshot of the main window of the program *EXAFS Calculations* showing the atom coordinates of the initial model. The variable R_{\min} reflects the distance to the nearest manganese atom. Atoms can be (de-)selected using the checkboxes on the left-hand side of the window.

A.4.1. Description of features

The program *EXAFS Calculations* allows the calculation of EXAFS spectra for a given model of the manganese complex and optimization of the atom coordinates in regard to experimental spectra. The used equations can be found in Section 4.2 and 4.4.

On start of the program, the user is asked to select the file containing the coordinates of the model (as xyz format), the phase/amplitude functions (via a text file with a list of phase-function files; see Section A.2.3 for details), and also (optionally) a list of distance restraints to use when optimizing the model (see A.4.2).

After this, the main window of the program appears, which can be seen in Fig. A.2. In this window the list of atoms is shown. Via different tab pages also the XAS shells considered for calculations of the EXAFS spectra and the loaded restraints can be viewed (Fig. A.3). After the curve fitting is done, the results of the optimization process (both model coordinates and shells) can be viewed in separate tab pages.

One of the main features of this window is to select and de-select certain atoms and/or shells via checkboxes to allow for testing of the influence of certain atoms/shells on the EXAFS spectra. This selection can be either done manually or via some

A.4. Program for calculation of EXAFS spectra

Shell	N [1]	R [Å]	2σ² [Å²]	Angle to M [°]	Angle to a [°]	Angle to b [°]	Angle to c [°]	Phase function cos	Phase function sin
<input checked="" type="checkbox"/> Mn4-O81	0.25	1.91653...	0.002	46.2988887...	44.6532607...	63.7407725...	56.9016292...	MnO1.92Cos.dat	MnO1.92Sin.dat
<input checked="" type="checkbox"/> Mn2-O65	0.25	1.92868...	0.002	39.7291214...	51.9836595...	59.0256711...	53.3801681...	MnO1.92Cos.dat	MnO1.92Sin.dat
<input checked="" type="checkbox"/> Mn4-O78	0.25	1.94486...	0.002	50.9440656...	42.7600747...	62.0551835...	60.5763162...	MnO1.92Cos.dat	MnO1.92Sin.dat
<input checked="" type="checkbox"/> Mn4-O82	0.25	1.94726...	0.002	77.0087111...	78.6193402...	34.9336315...	57.4827244...	MnO1.92Cos.dat	MnO1.92Sin.dat
<input checked="" type="checkbox"/> Mn3-O61	0.25	1.95803...	0.002	63.8750157...	64.7376853...	51.7798976...	48.7288299...	MnO1.92Cos.dat	MnO1.92Sin.dat
<input checked="" type="checkbox"/> Mn1-N7	0.25	1.96512...	0.002	78.2800690...	42.4338978...	68.1042104...	55.7835987...	MnN2.19Cos.dat	MnN2.19Sin.dat
<input checked="" type="checkbox"/> Mn1-O69	0.25	1.97943...	0.002	58.8924871...	67.1703338...	41.4948491...	57.5160104...	MnO2.02Cos.dat	MnO2.02Sin.dat
<input checked="" type="checkbox"/> Mn1-O79	0.25	2.01233...	0.002	56.2343126...	36.0912241...	68.5545039...	62.4916289...	MnO2.02Cos.dat	MnO2.02Sin.dat
<input checked="" type="checkbox"/> Mn3-O79	0.25	2.08771...	0.002	61.1875067...	63.5843062...	42.0443811...	59.9611450...	MnO2.10Cos.dat	MnO2.10Sin.dat
<input checked="" type="checkbox"/> Mn3-O66	0.25	2.15307...	0.002	57.8465408...	35.1668422...	72.3855930...	60.6556223...	MnO2.10Cos.dat	MnO2.10Sin.dat
<input checked="" type="checkbox"/> Mn3-O77	0.25	2.28171...	0.002	40.6445390...	52.0164629...	58.3631658...	53.9630789...	MnO2.10Cos.dat	MnO2.10Sin.dat
<input checked="" type="checkbox"/> Mn1-O77	0.25	2.31883...	0.002	45.7175930...	57.0125764...	51.5352391...	55.7565182...	MnO2.10Cos.dat	MnO2.10Sin.dat
<input checked="" type="checkbox"/> Mn1-Mn2	0.5	2.70281...	0.002	85.8582693...	28.4069876...	81.1863893...	63.2318080...	MnMn2.70Cos.dat	MnMn2.70Sin.dat
<input checked="" type="checkbox"/> Mn2-Mn3	0.5	2.73766...	0.002	88.2642550...	87.9950049...	35.0708326...	55.0037703...	MnMn2.74Cos.dat	MnMn2.74Sin.dat
<input checked="" type="checkbox"/> Mn2-C45	0.25	2.77317...	0.002	57.2785900...	49.0849071...	64.7857601...	51.3795288...	MnC2.69Cos.dat	MnC2.69Sin.dat
<input checked="" type="checkbox"/> Mn1-C41	0.25	2.78873...	0.002	58.6231774...	80.2876799...	42.3246636...	49.3184312...	MnC2.69Cos.dat	MnC2.69Sin.dat
<input checked="" type="checkbox"/> Mn3-C27	0.25	2.79440...	0.002	85.9504572...	54.8196789...	57.2287039...	52.2353446...	MnC2.69Cos.dat	MnC2.69Sin.dat
<input checked="" type="checkbox"/> Mn3-Mn4	0.5	2.83788...	0.002	34.0763478...	60.6850217...	59.8251145...	44.5626093...	MnMn2.74Cos.dat	MnMn2.74Sin.dat
<input checked="" type="checkbox"/> Mn3-C37	0.25	2.85056...	0.002	50.0448479...	51.2792110...	64.0729327...	49.7456949...	MnC2.91Cos.dat	MnC2.91Sin.dat
<input checked="" type="checkbox"/> Mn4-C50	0.25	2.85707...	0.002	52.8475929...	40.7234114...	70.3325974...	56.0205612...	MnC2.91Cos.dat	MnC2.91Sin.dat
<input checked="" type="checkbox"/> Mn4-C27	0.25	2.86726...	0.002	27.2985972...	72.3352838...	53.7502782...	41.6533181...	MnC2.91Cos.dat	MnC2.91Sin.dat
<input checked="" type="checkbox"/> Mn1-C33	0.25	2.91754...	0.002	30.5729172...	66.7577616...	52.3066348...	46.6956687...	MnC2.91Cos.dat	MnC2.91Sin.dat
<input checked="" type="checkbox"/> Mn1-C23	0.25	2.93720...	0.002	63.8890379...	34.0325181...	75.3380235...	60.0559132...	MnC2.91Cos.dat	MnC2.91Sin.dat
<input checked="" type="checkbox"/> Mn1-O68	0.25	2.93764...	0.002	65.9384134...	61.2023351...	54.0496578...	49.4131461...	MnO2.88Cos.dat	MnO2.88Sin.dat
<input checked="" type="checkbox"/> Mn2-C41	0.25	2.95240...	0.002	64.8061601...	40.8459783...	55.9629961...	70.2257759...	MnC2.91Cos.dat	MnC2.91Sin.dat

Number of atoms in initial model: 86 (moveable: 86) Number of shells of initial model: 334

Figure A.3.:

Screenshot of the program showing the shells used for calculation of EXAFS spectra for the initial model. All important variables including the distances and angles are listed. Additionally, the used phase/amplitude function files are displayed. The shells can be (de-)activated using checkboxes.

toggle buttons in the toolbar of the main window. Using the icons, atoms of certain elements can be (de-)selected, and also one toggle button (with lettering “Do not use...”/“Use...”) can be used to (de-)select atoms only specifically outside a (in the text field) given radius around the Mn (compare Fig. A.2 and Fig. A.3). Spectra as shown in Figs. 5.9 and 5.10 can therefore easily be calculated. Additionally, after pressing the toggle button with the red arrow symbol, atoms can be defined which cannot be moved by the Levenberg-Marquardt (LM) algorithm *levmar* [Lourakis, 2004] by deselecting them.

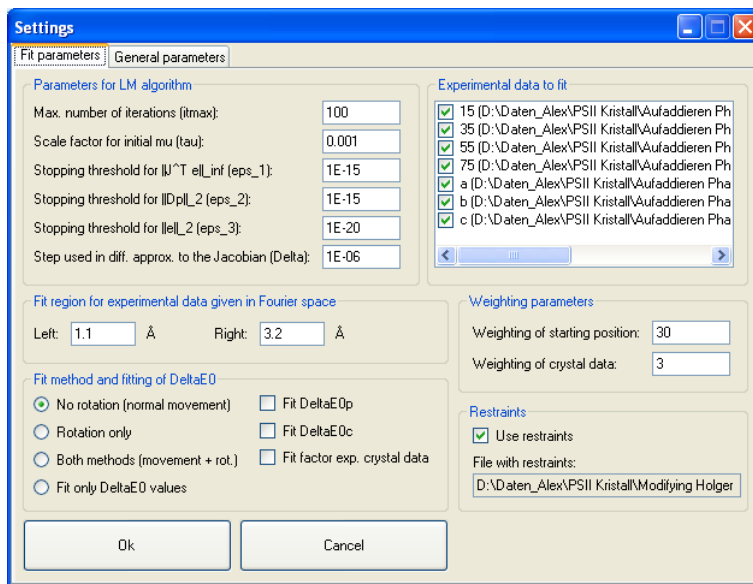
Options for general and fit parameters are accessible under the menu entry “Settings” (under “Calculate”; Figs. A.4 and A.5). In the “Fit parameters” tab, parameters for the LM algorithm can be set. Additionally, the experimental data to consider for the curve-fitting process can be (de-)selected and weighting parameters for the starting position (equals factor e in Eq. (4.8)) and the EXAFS data of crystals (factor c in Eq. (4.7)) can be defined (compare Section 4.4). This window also allows defining the fit region of the EXAFS data for PSII crystal, since in this case the curve fitting is

A. Appendix

done in Fourier space (as described in Section 4.4). Finally, the use of restraints can be (de-)activated and several fit methods—like fitting of the ΔE_0 values or additional rotation of the model—can be selected.

Figure A.4.:

Screenshot of the main options dialog with selected “Fit parameters” tab. Here, all parameters for the LM algorithm and the fit process can be set including selection of the experimental data and setting of weighting parameters for the starting position of the atoms and the crystal spectra.



The “General parameters” tab offers possibilities to change several EXAFS parameters like, e. g., S_0^2 or I_{ord} . Also the membrane normal can be defined (default is the vector calculated based on the XRD data from Loll et al. [2005]) and the number of points for interpolation of the phase/amplitude functions as well as the experimental spectra can be set. In the lower part of the window, parameters for the Fourier transform like the window function are modifiable. The “Restrains” tab offers an overview of the used distance restraints including the current and the target distance as can be seen in Fig. A.6.

EXAFS spectra calculated using the currently selected atoms and shells can be viewed by pressing the respective icon or menu entry (“Calculate” → “Show spectra. . .”). In this window it is possible to save and load certain graphs for comparison (compare Fig. A.7). Also, the distance distribution for Mn-Mn, Mn-Ca, Mn-O, Mn-C, Mn-N, and C-O distances can be displayed (“Calculate” → “Show distance distributions. . .”).

After a fit of the experimental data is completed, the results can also be graphically shown in the windows mentioned above (Fig. A.7). In the “Final model” tab, apart from the atom coordinates also the distance which the respective atom has moved during the fit process are listed (A.9). Moreover, in the “Restrains” tab now the distance for the model after the fit is automatically displayed (Fig. A.6). These feature allow for a quick evaluation of the fit quality apart from the error value, which is always displayed directly after the fit and can later be shown (“Calculate” → “Show fit results. . .”).

A.4. Program for calculation of EXAFS spectra

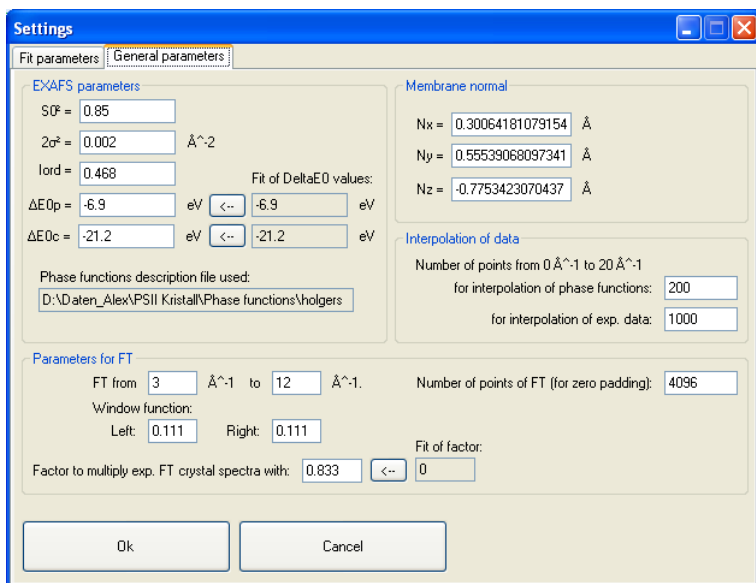


Figure A.5.:

Screenshot of the main options dialog with selected “General parameters” tab. In this tab, it is possible to define EXAFS parameters, but also configure details of the Fourier transform, and specify how many points are used for interpolation of the phase functions and the experimental data.

Using the “File” menu, the atom coordinates, the shells, and the spectra can be saved (both for the original and the fit model). Every file generated in this way contains a detailed header with all important information.

A.4.2. Format of restraints

As mentioned in the section above, restraints for the curve-fitting process can be set for distances between atom using a text file. Hereby, every restraint entry contains of two number defining the atoms involved, the target distance, and a weighting factor for calculation of the error value. The respective line in the text file has the following format:

```
numberOfAtom1 numberOfAtom2 targetDistance weightingFactor
```

Example:

```
4 3 2.697 1000
```

This line defines a restraint between atoms 4 and 3. The distance should be 2.697 Å. The used weighting factor for this restraint is 1000. The atom numbers are referring to a model without H atoms.

Alternatively, restraints for all atom pairs of selected elements and distance regions can be defined:

```
element1 element2 minDist maxDist targetDistance weightingFactor
```

A. Appendix

Atom 1	Atom 2	Target distance [Å]	Weighting factor	Distance starting model [Å]	Distance fit [Å]
Mn1	O79	1.85	40	2.0123319647337	1.90387840553...
Mn1	O76	1.8	40	1.77711090520293	1.82984344078...
Mn1	O77	2.45	100	2.3188391200273	2.47595952305...
Mn2	O79	1.8	40	1.63197981370937	1.75828668327...
Mn2	O76	1.77	40	1.76383857255401	1.79083810115...
Mn2	O80	1.77	40	1.86452811244561	1.75341289682...
Mn3	O78	1.82	40	1.81516177251505	1.77818345749...
Mn3	O77	2.3	40	2.28171705046879	2.20584959600...
Mn3	O79	1.85	40	2.08771933278878	2.05401538148...
Mn3	O80	1.82	40	1.80465354669532	1.80363439218...
Mn4	O78	1.77	40	1.94486111588977	1.87549694534...
Mn4	O77	1.8	40	1.68159309111925	1.70343385177...
N6	C21	1.37998297293843	80	1.37998297293843	1.38550212763...
N6	C22	2.37034494960122	80	2.37034494960122	2.37059366140...
N6	C23	1.38151308006837	80	1.38151308006837	1.37991842067...
N7	C21	2.29766443497065	80	2.29766443497065	2.30470509459...
N7	C22	1.34839301520328	80	1.34839301520328	1.34344624214...
N7	C23	1.40383016165382	80	1.40383016165382	1.40490830974...
N8	C19	1.3246943934995	80	1.3246943934995	1.3246943934995
N8	C24	1.44719148842715	80	1.44719148842715	1.44719148842...
N8	C25	2.41050856609326	80	2.41050856609326	2.41084199228...
N9	C38	1.46659642028746	80	1.46659642028746	1.46659642028...
N9	C39	2.42841600340633	80	2.42841600340633	2.42104660973...
N10	C38	2.42735750510715	80	2.42735750510715	2.42735750510...
N10	C39	1.33096050369648	80	1.33096050369648	1.32989723420...
N10	C42	1.47189843318077	80	1.47189843318077	1.47189843318...
N10	C43	2.47455661814395	80	2.47455661814395	2.47455661814...
N11	C43	1.38074916317194	80	1.38074916317194	1.3888468775879
N11	C44	1.50190849671343	80	1.50190849671343	1.50222366096...
N11	C45	2.40029378776849	80	2.40029378776849	2.40479199389...
N11	C46	2.42438787534091	80	2.42438787534091	2.42341301996...

Figure A.6.:

Screenshot of the “Restrains” tab of the main window after a fit is done. A list of the used restraints is given. Additionally, the respective distances for both the initial and the fit model are listed.

Example:

```
Mn O 1.0 1.5 1.4 100
```

sets restraints for all Mn-O vectors of a distance between 1.0 and 1.5 Å. The target distance is 1.4 Å. The used weighting factor for all restraints of this type is 100.

An X can be used as placeholder for element symbols in restraints, e. g.,

```
Mn X 1.0 1.5 1.4 100
```

sets restraints for all atom-atom distances where at least one Mn is involved and which are between 1.0 and 1.5 Å long.

If `targetDistance` is set to 0, the according distance in the original model is taken instead. Comments can be added after each line or as a separate line. Additionally, a number sign (#) can be used to comment out single lines in restraint files.

In the following, an example for a typical restraint file is shown:

A.4. Program for calculation of EXAFS spectra

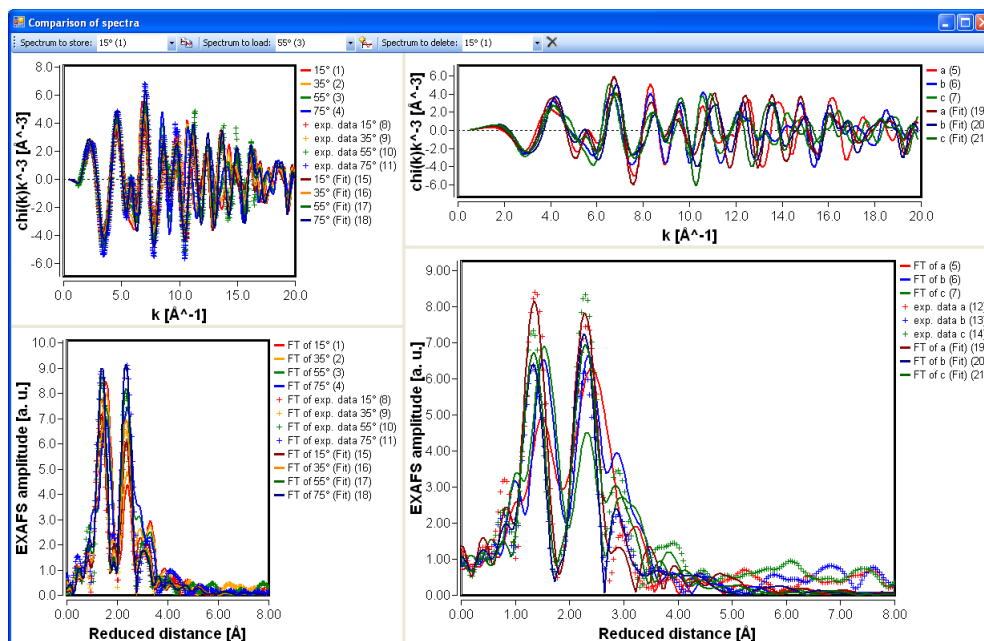


Figure A.7.:

Screenshot of the window showing the EXAFS data in k and Fourier space for both partially oriented and crystal samples. Spectra for the initial model (bright colors), the fit model (dark colors), and the experimental data (crosses) are displayed parallelly. Single spectra can be stored and later reloaded and also deleted. The size of the individual graphs is variable.

```
All atom numbers without H!
Internal (short) Mn-O distances:
1 79 1.85 40
1 76 1.80 40
1 77 2.45 100 long Mn-O distance
2 79 1.80 40
2 76 1.77 40
2 80 1.77 40
3 78 1.82 40
3 77 2.30 40
3 79 1.85 40
3 80 1.82 40
#3 90 1.80 20
4 78 1.77 40
4 77 1.80 40
Rest:
```

A. Appendix

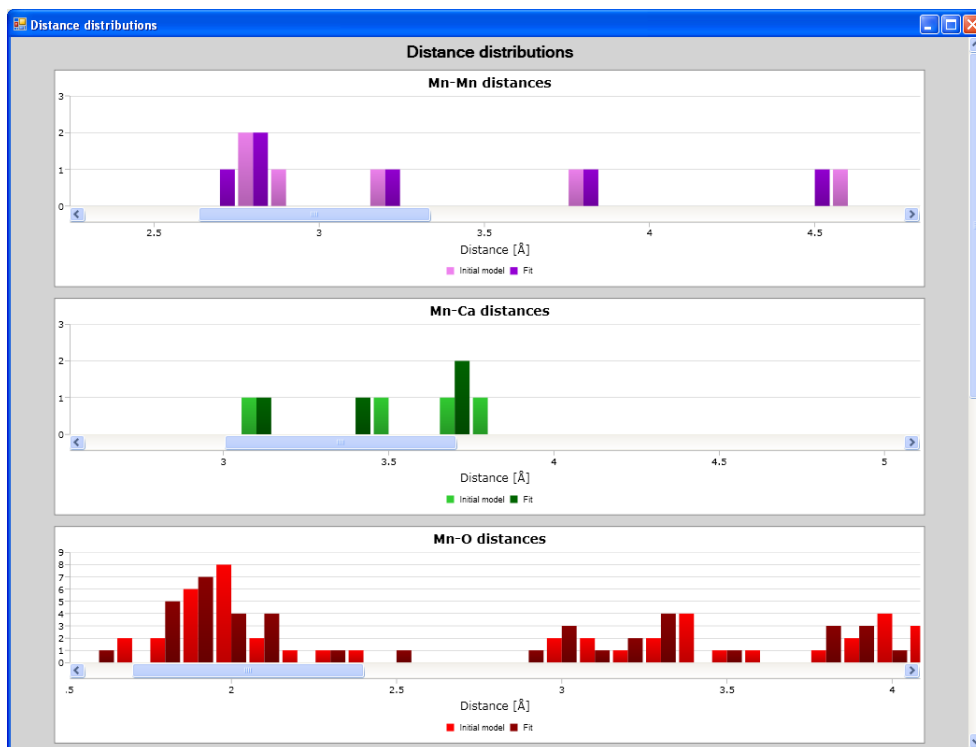


Figure A.8.:

Screenshot of window displaying the distance distribution for the Mn-Mn, Mn-Ca, Mn-O, Mn-C, Mn-N, and C-O distances of initial model (bright colors) and the fit model (dark colors).

```
C X 1.0 2.5 0 80 short C-X
N N 1.0 2.5 0 80 short N-N
```

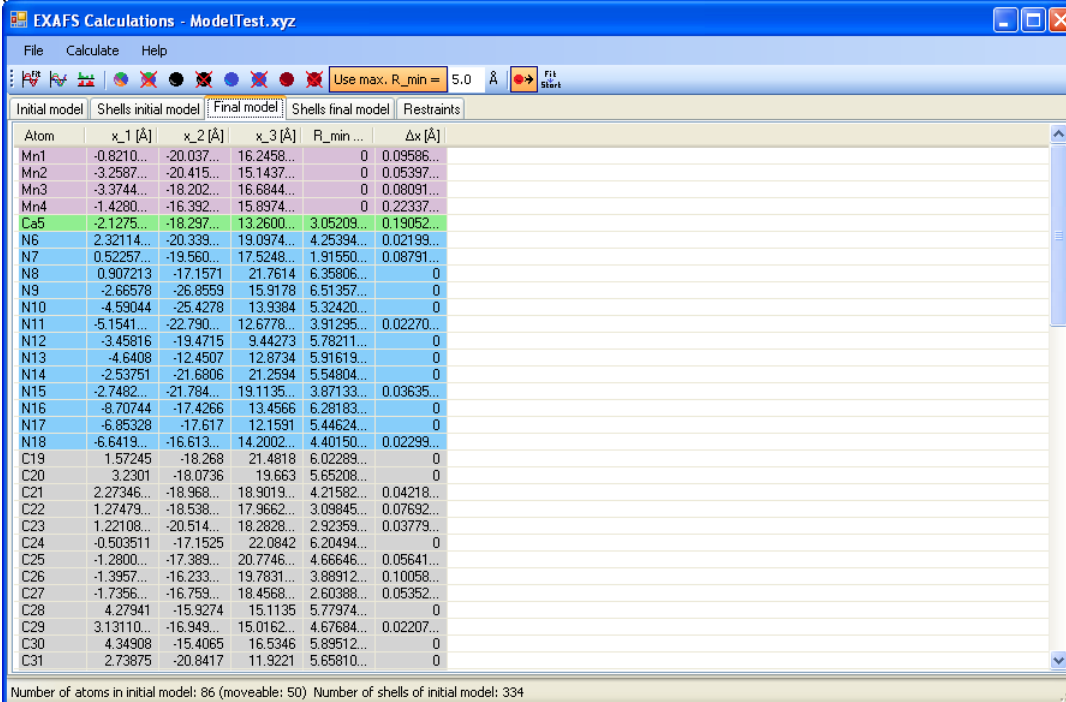
The resulting restraints for this list are shown in Fig. A.6.

A.4.3. List of used libraries

For the program, the following non-standard libraries were used:

- For implementation of the Levenberg-Marquardt algorithm:
levmar version 2.4, <http://www.ics.forth.gr/~lourakis/levmar/> [Lourakis, 2004].
- For the fast Fourier transforms:
FFTW3, <http://www.fftw.org/> [Frigo and Johnson, 2005].
- For displaying of spectra (window “Comparison of spectra”):
Mitov PlotLab .NET 4.3, <http://www.mitov.com/html/plotlab.html>.

A.5. Used molecular visualization programs



The screenshot shows the 'EXAFS Calculations - ModelTest.xyz' window. It features a menu bar (File, Calculate, Help) and a toolbar with icons for file operations and a 'Fit Start' button. Below the toolbar is a table with columns for 'Initial model', 'Shells initial model', 'Final model', 'Shells final model', and 'Restrains'. The main data table has columns: 'Atom', 'x_1 [Å]', 'x_2 [Å]', 'x_3 [Å]', 'R_min ...', and 'Δx [Å]'. The table lists atoms from Mn1 to C31. Atoms Mn1-Mn4 and Ca5 are highlighted in green. Atoms N6-C31 are highlighted in blue. The 'R_min' column shows values like 0, 0.09586, 0.05337, etc. The 'Δx' column shows values like 0, 0.02199, 0.08791, etc. At the bottom of the window, it states: 'Number of atoms in initial model: 86 (moveable: 50) Number of shells of initial model: 334'.

Atom	x ₁ [Å]	x ₂ [Å]	x ₃ [Å]	R _{min} ...	Δx [Å]
Mn1	-0.9210...	-20.037...	16.2458...	0	0.09586...
Mn2	-3.2587...	-20.415...	15.1437...	0	0.05337...
Mn3	-3.3744...	-18.202...	16.6844...	0	0.08091...
Mn4	-1.4280...	-16.392...	15.8974...	0	0.22337...
Ca5	-2.1275...	-18.297...	13.2600...	3.05209...	0.19052...
N6	2.32114...	-20.339...	19.0974...	4.25394...	0.02199...
N7	0.52257...	-19.560...	17.5248...	1.91550...	0.08791...
N8	0.907213	-17.1571	21.7614	6.36806...	0
N9	-2.66578	-26.8559	15.9178	6.51357...	0
N10	-4.59044	-25.4278	13.9384	5.32420...	0
N11	-5.1541...	-22.790...	12.6778...	3.91295...	0.02270...
N12	-3.45816	-19.4715	9.44273	5.78211...	0
N13	-4.6408	-12.4507	12.8734	5.91619...	0
N14	-2.53751	-21.6806	21.2594	5.54804...	0
N15	-2.7482...	-21.784...	19.1135...	3.87133...	0.03635...
N16	-8.70744	-17.4266	13.4566	6.29183...	0
N17	-6.85328	-17.617	12.1591	5.44624...	0
N18	-6.6419...	-16.613...	14.2002...	4.40150...	0.02299...
C19	1.57245	-18.268	21.4818	6.02289...	0
C20	3.2301	-18.0736	19.663	5.65208...	0
C21	2.27346...	-18.968...	18.9019...	4.21582...	0.04218...
C22	1.27479...	-18.538...	17.9662...	3.09845...	0.07692...
C23	1.22108...	-20.514...	18.2828...	2.92359...	0.03779...
C24	-0.503511	-17.1525	22.0842	6.20494...	0
C25	-1.2800...	-17.389...	20.7746...	4.66546...	0.05641...
C26	-1.3957...	-16.233...	19.7831...	3.88912...	0.10058...
C27	-1.7356...	-16.759...	18.4568...	2.60388...	0.05352...
C28	4.27941	-15.9274	15.1135	5.77974...	0
C29	3.13110...	-16.949...	15.0162...	4.67694...	0.02207...
C30	4.34908	-15.4065	16.5346	5.89512...	0
C31	2.73875	-20.8417	11.9221	5.65810...	0

Figure A.9.:

Screenshot of the main window with a list of the atom coordinates of the fit model. The column Δx reflects the movement of the atoms due to the optimization process. In this example, the positions of some atoms were kept constant. In these cases 0 is displayed.

- For displaying of bar diagrams (window “Distance distributions”):
Visifire 2.3.5, <http://www.visifire.com/>.

A.5. Used molecular visualization programs

The following molecular visualization programs were used in making the figures of this thesis:

- For Figs. 2.2, 2.3, 2.4, 2.5, 2.6, 2.9, 5.5, 5.11, 5.12, 5.13, 6.2: PyMOL [DeLano Scientific, LLC, 2008].
- For Figs. 1.2, 4.1: QuteMol [Tarini et al., 2006].

B. Atom coordinates of models

In the following, the coordinates for the models C-I, C-II, C-III, C-IV, D, and F are listed.

B.1. Model C-I

```
Mn -0.679583 -20.066978 15.905499
Mn -3.522658 -20.703953 15.241081
Mn -3.208783 -18.305963 16.428991
Mn -1.343768 -16.411973 15.817822
Ca -1.971405 -18.589914 13.306518
N 2.242999 -20.267311 18.761708
N 0.746505 -19.690020 17.276958
N 0.907200 -17.157000 21.761000
N -2.665700 -26.855500 15.917700
N -4.599326 -25.405598 13.942265
N -4.958252 -22.991928 11.946182
N -4.599400 -12.499200 12.932900
C 1.572500 -18.268000 21.481700
C 3.230100 -18.073200 19.663000
C 2.296711 -18.909393 18.700587
C 1.246642 -18.563476 17.750459
C 1.190349 -20.697737 17.952016
C -0.503200 -17.152400 22.083800
C -1.326936 -17.574678 20.898762
C -1.363925 -16.450052 19.881470
C -1.689621 -17.044339 18.489141
C 2.805600 -20.885700 11.817000
C 2.409287 -20.353080 13.223055
C 0.970687 -20.003912 13.717824
C -9.224800 -20.273000 17.990800
C -7.951295 -20.446575 17.083338
C -6.745484 -19.950262 17.918832
C -5.544950 -19.845951 16.992500
C -2.852388 -25.449080 15.608703
```

B. Atom coordinates of models

C -3.296334 -25.254133 14.177539
C -1.702364 -24.490778 16.137915
C -1.961315 -22.941375 15.918906
C -5.175200 -25.312100 12.592600
C -5.877116 -23.981515 12.371751
C -5.208692 -21.619153 11.789404
C -4.382235 -20.773613 12.602873
C -6.503600 -21.105600 11.232600
C -3.242100 -12.796500 12.419200
C -2.983265 -14.390242 12.246323
C -2.805604 -15.370740 13.622645
O 1.066500 -19.380800 21.455100
O -2.612649 -17.930498 18.413002
O -0.917598 -16.400206 17.697879
O 0.234146 -19.323610 12.948089
O 0.741779 -20.445258 14.879699
O -5.157744 -20.834636 16.327408
O -4.762230 -18.878925 17.135389
O -2.493780 -25.152018 13.243638
O -3.130773 -22.659257 15.591323
O -1.002840 -22.139116 16.047377
O -6.961400 -23.886800 11.855900
O -3.539109 -19.961918 12.104226
O -4.470645 -21.148740 13.799954
O -1.807549 -16.335944 13.765827
O -4.014030 -15.630785 14.220341
O -2.172398 -20.642402 14.051738
O -1.501611 -18.300549 15.664232
O -2.937954 -16.493634 16.449255
O -2.471170 -20.001353 16.530431
O -3.639848 -18.909944 14.689105
O 0.694165 -17.023316 15.021783
O -0.947472 -14.456014 15.807966
O -0.920400 -18.323300 11.170700
N -3.458200 -19.471100 9.442700
N -2.537500 -21.680200 21.259100
N -2.960977 -21.591292 19.165059
C -3.413800 -22.711900 21.006000
C -3.657756 -22.640178 19.637265
C -2.375576 -20.952042 20.145695
N -8.707300 -17.426600 13.456500
N -6.853300 -17.617000 12.159100

N -6.697487 -16.475969 14.138444
C -7.422500 -17.184100 13.265200
C 4.279300 -15.927400 15.113500
C 3.111496 -16.910282 14.986486
C 4.349000 -15.406200 16.534600
C -3.993500 -13.636100 20.034500
O -3.152428 -14.071745 19.001177
O -3.031800 -13.331500 20.950900
C -5.186600 -18.182300 21.927700
C 0.063100 -23.861400 20.130600
O 3.226000 -22.577700 19.641300
O -3.921100 -10.888700 14.398400
O -8.486100 -15.233100 15.410500

B.2. Model C-II

Mn -0.823786 -20.470438 16.012389
Mn -3.675550 -20.578976 14.889770
Mn -3.182289 -18.312505 16.360056
Mn -0.989119 -16.779087 16.092929
Ca -1.302264 -18.771472 13.303762
N 2.177854 -20.360384 19.096389
N 0.688828 -19.974158 17.530494
N 0.907200 -17.157000 21.761000
N -2.665700 -26.855500 15.917700
N -4.589782 -25.430693 13.938359
N -4.824246 -22.991769 12.125442
N -4.599400 -12.499200 12.932900
C 1.572500 -18.268000 21.481700
C 3.230100 -18.073200 19.663000
C 2.310979 -19.048184 18.815096
C 1.318708 -18.827273 17.814118
C 1.235599 -20.911690 18.293072
C -0.503200 -17.152400 22.083800
C -1.295828 -17.821716 20.978914
C -2.102096 -16.878425 20.080952
C -1.955652 -17.258810 18.608947
C 2.805600 -20.885700 11.817000
C 2.493928 -21.343841 13.289451
C 1.212995 -20.741713 13.896851
C -9.224800 -20.273000 17.990800

B. Atom coordinates of models

C -7.708000 -20.446500 17.731700
C -7.145583 -19.448724 16.694701
C -5.623035 -19.517807 16.355776
C -2.809652 -25.433965 15.583229
C -3.276021 -25.350341 14.130805
C -2.080418 -24.368601 16.391360
C -2.233115 -22.899961 15.983660
C -5.175200 -25.312100 12.592600
C -5.869815 -23.947591 12.428847
C -4.751202 -21.730645 11.415608
C -4.029382 -20.691445 12.210170
C -5.928525 -21.215166 10.632954
C -3.242100 -12.796500 12.419200
C -2.436198 -14.205506 12.573866
C -2.381184 -15.478307 13.793893
O 1.066500 -19.380800 21.455100
O -2.856300 -17.929388 18.053988
O -0.988313 -16.623305 18.079423
O 0.740535 -19.906587 13.094311
O 0.822320 -21.058999 15.076196
O -5.259523 -20.557751 15.713881
O -4.993495 -18.511297 16.831881
O -2.467218 -25.125835 13.226823
O -3.336777 -22.491608 15.521290
O -1.232653 -22.183990 16.235582
O -6.961400 -23.886800 11.855900
O -2.897274 -20.089158 12.110367
O -4.515668 -20.882683 13.351834
O -1.261250 -16.313563 14.093860
O -3.667985 -15.925698 13.755311
O -2.033441 -20.926145 13.939929
O -1.300656 -18.572234 16.038900
O -2.817798 -16.499356 16.175255
O -2.694705 -20.138188 16.391517
O -3.663637 -18.903744 14.703334
O 0.909606 -17.258524 15.433543
O -0.523406 -14.956389 16.228329
O -0.920400 -18.323300 11.170700
N -3.458200 -19.471100 9.442700
N -2.537500 -21.680200 21.259100
N -3.375037 -21.307211 19.311666
C -3.413800 -22.711900 21.006000

C -4.042600 -22.389000 19.840900
C -2.429109 -20.939302 20.161075
N -8.707300 -17.426600 13.456500
N -6.853300 -17.617000 12.159100
N -6.658981 -16.556619 14.174927
C -7.422500 -17.184100 13.265200
C 4.279300 -15.927400 15.113500
C 3.562464 -17.281137 15.094926
C 4.349000 -15.406200 16.534600
C -3.993500 -13.636100 20.034500
O -3.527646 -14.533178 19.037461
O -3.031800 -13.331500 20.950900
C -5.186600 -18.182300 21.927700
C 0.063100 -23.861400 20.130600
O 3.226000 -22.577700 19.641300
O -3.921100 -10.888700 14.398400
O -8.486100 -15.233100 15.410500

B.3. Model C-III

Mn -0.758080 -19.765569 15.687982
Mn -3.364145 -20.376224 15.161389
Mn -3.318669 -18.434223 17.053546
Mn -1.420562 -16.166942 16.381640
Ca -2.686605 -17.534274 13.547472
N 1.984971 -20.199962 18.767297
N 0.689563 -19.594734 17.069027
N -2.665700 -26.855700 15.917700
N -4.590300 -25.427800 13.938300
N -4.982538 -22.829798 12.306761
N -4.633600 -12.441900 12.881300
C 3.230100 -18.073400 19.663000
C 2.249127 -18.878221 18.602002
C 1.386206 -18.526494 17.507557
C 1.056964 -20.597622 17.853573
C -0.503300 -17.152400 22.084000
C -1.396305 -16.989966 20.871698
C -0.479709 -17.702931 19.874491
C -1.162583 -17.648865 18.596148
C 2.729700 -20.838400 11.885800
C 1.699569 -19.554886 12.068804

B. Atom coordinates of models

C 0.422672 -19.369694 13.056409
C -9.224800 -20.273200 17.990800
C -7.935100 -20.710000 17.254900
C -6.639462 -20.595446 18.104450
C -5.384662 -20.177918 17.289150
C -2.808700 -25.432900 15.588400
C -3.281400 -25.310900 14.147700
C -1.670367 -24.350146 16.048895
C -1.860259 -22.759883 15.706582
C -5.175200 -25.312100 12.592600
C -5.868500 -23.952400 12.417500
C -5.117169 -21.467705 11.832123
C -4.421507 -20.443730 12.665702
C -6.265600 -21.048000 10.967300
C -4.821600 -11.371200 13.742300
C -3.290700 -12.735500 12.352100
C -2.671853 -14.088385 12.871898
C -2.586911 -14.579329 14.302135
O -2.149365 -18.415878 18.520441
O -0.758745 -16.736456 17.807359
O -0.513485 -18.539370 12.714800
O 0.572239 -19.893543 14.201617
O -4.993700 -20.910132 16.318657
O -4.803730 -19.154864 17.775842
O -2.473100 -25.124500 13.231700
O -2.979393 -22.251233 15.455053
O -0.956909 -21.850283 15.781789
O -6.961400 -23.886800 11.856000
O -3.943329 -19.304549 12.330322
O -4.337836 -21.006539 13.781782
O -3.927800 -10.888100 14.397900
O -1.654453 -15.584079 14.398645
O -3.717430 -14.584455 15.055972
O -1.924394 -19.846989 14.235036
O -1.925721 -17.608475 15.424599
O -3.006579 -16.531392 17.156436
O -2.376812 -20.076172 16.690849
O -4.005129 -18.726918 15.404808
O 0.380912 -15.921949 15.779911
O -1.441859 -14.345921 17.026258
O -2.565000 -16.815500 11.246900
N -3.458200 -19.471300 9.442700

N -2.537500 -21.680400 21.259200
N -2.498205 -22.047101 19.136050
C -3.413800 -22.711900 21.006200
C -3.556800 -22.768200 19.655300
C -1.920486 -21.375936 20.119206
N -8.707300 -17.426600 13.456500
N -6.853300 -17.617000 12.159100
N -6.606148 -16.827199 14.282323
C -7.422500 -17.184100 13.265300
C 1.572500 -18.268000 21.481700
O 1.066600 -19.380800 21.455100
C 4.279300 -15.927400 15.113500
C 2.857167 -16.441143 14.840051
C 4.349000 -15.406300 16.534600
C -5.530000 -13.646100 20.687000
C -3.969900 -13.624200 20.010600
O -4.150723 -13.902916 18.634741
O -3.016900 -13.343900 20.944100
C -5.186600 -18.182300 21.927700
C 0.063100 -23.861600 20.130600
O 3.226000 -22.577700 19.641300
O -8.486100 -15.233100 15.410500
O -6.718000 -20.643200 21.685700

B.4. Model C-IV

Mn -0.249205 -20.188600 15.852777
Mn -2.896215 -20.768532 15.500917
Mn -2.696150 -18.491719 16.938666
Mn -1.323028 -15.996099 15.910154
Ca -1.794833 -18.606699 13.308044
N 2.076948 -20.260370 18.992764
N 0.780374 -19.763854 17.296414
N 0.907200 -17.157000 21.761200
N -2.665700 -26.855700 15.917700
N -4.590300 -25.427800 13.938300
N -4.974563 -22.895065 12.233070
N -4.588800 -12.512900 12.935200
C 1.572500 -18.268000 21.481700
C 3.230100 -18.073400 19.663000
C 2.302447 -18.948205 18.740979

B. Atom coordinates of models

C 1.471303 -18.666011 17.611486
C 1.205001 -20.746658 18.079573
C -0.503300 -17.152400 22.084000
C -1.346994 -17.322621 20.828457
C -0.596969 -16.460607 19.813229
C -1.048495 -16.876348 18.467927
C 4.113100 -21.798800 11.695300
C 2.844100 -20.866800 11.745500
C 2.716657 -20.033523 13.040273
C 1.298168 -19.868941 13.583957
C -7.865800 -20.621500 17.281400
C -6.502076 -20.352990 18.051045
C -5.140996 -20.066731 17.272721
C -2.814972 -25.427896 15.595967
C -3.283015 -25.311138 14.151235
C -1.563303 -24.515018 15.995132
C -1.608323 -22.957823 15.858593
C -5.175200 -25.312100 12.592600
C -5.868500 -23.952400 12.417500
C -5.264508 -21.518661 12.199214
C -4.295066 -20.768607 12.993663
C -6.672384 -20.997264 12.179305
C -4.802600 -11.405300 13.748300
C -3.229800 -12.796300 12.412200
C -2.993172 -14.403008 12.510493
C -2.849456 -15.335579 13.753729
O 1.066600 -19.380800 21.455100
O -1.742716 -17.930185 18.361536
O -0.664702 -16.069059 17.589497
O 0.421621 -19.249551 12.913991
O 1.138801 -20.384242 14.719873
O -4.706134 -20.994658 16.523049
O -4.501074 -19.012836 17.666310
O -2.499909 -24.966616 13.260519
O -2.785587 -22.525902 15.744680
O -0.513645 -22.263603 15.949049
O -6.961400 -23.886800 11.856000
O -3.692029 -19.808768 12.447920
O -4.159973 -21.239364 14.154922
O -3.918200 -10.892500 14.395300
O -1.864298 -16.295768 13.948406
O -3.953250 -15.432234 14.540548

O -1.566981 -20.399865 14.528869
O -0.900143 -17.825685 15.678099
O -2.837803 -16.554658 16.707569
O -1.867556 -20.253268 16.908901
O -3.597302 -19.022524 15.428057
O 0.414234 -15.421483 15.273683
O -1.880800 -14.140291 16.194687
O -0.877800 -18.374300 11.144800
N -3.458200 -19.471300 9.442700
N -2.537500 -21.680400 21.259200
N -3.006248 -21.558255 19.160884
C -3.413800 -22.711900 21.006200
C -3.587167 -22.713897 19.644558
C -2.284095 -21.030314 20.138394
N -6.853300 -17.617000 12.159100
N -6.648900 -16.615300 14.205100
C -7.422500 -17.184100 13.265300
C 3.797400 -24.704200 17.568000
C 4.279300 -15.927400 15.113500
C 2.988881 -16.745337 14.935370
C 4.349000 -15.406300 16.534600
C -4.100100 -13.559100 20.193300
O -3.681155 -13.745152 18.880956
O -3.138100 -13.347300 21.135300
C -5.186600 -18.182300 21.927700
C 0.063100 -23.861600 20.130600
O 3.226000 -22.577700 19.641300
O -1.755300 -18.996300 22.991400
O 2.954600 -11.468700 16.984700

B.5. Model D

Mn -0.550322 -20.118710 15.971362
Mn -3.105250 -20.752609 15.277529
Mn -3.160018 -18.568238 16.878110
Mn -1.093462 -16.465850 16.195416
Ca -1.879677 -18.320305 13.491719
N 2.698377 -20.289380 18.349116
N 0.857314 -19.821993 17.218915
N 0.907200 -17.157000 21.761000
N -2.665700 -26.855500 15.917700

B. Atom coordinates of models

N -4.590300 -25.427800 13.938300
N -4.913471 -22.946546 12.133817
N -4.597800 -12.487800 12.917700
C 1.572500 -18.268000 21.481700
C 3.230100 -18.073200 19.663000
C 2.412535 -19.000014 18.662201
C 1.214688 -18.738865 17.921978
C 1.742005 -20.749138 17.470368
C -0.503200 -17.152400 22.083800
C -1.389691 -17.872378 21.084982
C -1.415736 -16.718020 20.088747
C -1.476271 -17.310349 18.736035
C 2.777000 -20.876500 11.869600
C 2.596293 -20.012274 13.138837
C 1.166332 -19.904529 13.641842
C -9.224800 -20.273000 17.990800
C -7.911900 -20.682300 17.260000
C -6.548463 -20.626502 18.046075
C -5.192395 -20.342691 17.286302
C -2.809987 -25.433687 15.589450
C -3.281224 -25.300934 14.150783
C -1.610492 -24.499786 16.008496
C -1.837657 -22.947155 15.793943
C -5.175200 -25.312100 12.592600
C -5.868500 -23.952400 12.417500
C -5.020563 -21.556871 11.834369
C -4.194514 -20.752417 12.757666
C -6.320800 -20.979600 11.355800
C -4.808300 -11.394500 13.748300
C -3.242100 -12.767200 12.391700
C -2.873576 -14.196822 13.062077
C -2.534709 -15.065880 14.319187
O 1.066500 -19.380800 21.455100
O -2.431477 -18.126390 18.561189
O -0.757264 -16.597039 17.929263
O 0.378602 -19.105331 13.054500
O 0.967084 -20.404755 14.795867
O -4.788586 -21.181766 16.398248
O -4.628523 -19.243129 17.661145
O -2.469160 -25.234813 13.221174
O -3.022761 -22.690268 15.502076
O -0.789796 -22.243691 15.982824

O -6.961400 -23.886800 11.855900
O -3.475133 -19.780372 12.399818
O -4.225595 -21.321905 13.876014
O -3.922400 -10.891000 14.400600
O -1.751679 -16.240102 14.277424
O -3.462320 -15.094526 15.304223
O -1.644297 -20.411685 14.536104
O -0.810831 -18.385696 16.254583
O -2.868822 -16.820225 16.523402
O -2.279089 -20.276569 16.791959
O -4.078301 -19.164219 15.427298
O 0.711674 -16.612422 15.286247
O -0.721298 -14.524488 16.443170
O -0.960500 -18.267100 11.122700
N -3.458200 -19.471100 9.442700
N -2.537500 -21.680200 21.259100
N -2.206188 -22.280606 19.221093
C -3.413800 -22.711900 21.006000
C -3.163100 -23.120600 19.733200
C -1.889574 -21.382765 20.135400
N -8.707300 -17.426600 13.456500
N -6.853300 -17.617000 12.159100
N -6.584061 -16.960077 14.313262
C -7.422500 -17.184100 13.265200
C 4.279300 -15.927400 15.113500
C 3.267001 -17.080775 15.050092
C 4.349000 -15.406200 16.534600
C -4.028500 -13.643000 20.048900
O -3.364897 -14.024855 18.863251
O -3.057900 -13.337600 20.955800
C -5.186600 -18.182300 21.927700
C 0.063100 -23.861400 20.130600
O 3.226000 -22.577700 19.641300
O -8.486100 -15.233100 15.410500
O 2.954600 -11.468700 16.984700

B.6. Model F

Mn -0.873202 -19.990111 16.320087
Mn -3.348700 -20.286787 15.249370
Mn -3.375463 -18.112968 16.834884

B. Atom coordinates of models

Mn -1.438963 -16.328672 16.042666
Ca -2.077050 -18.231737 13.370846
N 2.112381 -20.288740 19.089708
N 0.615319 -19.766715 17.548134
N 0.907200 -17.157000 21.760800
N -2.665700 -26.855300 15.917700
N -4.590300 -25.427800 13.938300
N -4.919842 -22.947332 12.167135
N -4.640800 -12.450400 12.873400
C 1.572500 -18.268000 21.481700
C 3.230100 -18.073100 19.663000
C 2.293274 -18.979427 18.828902
C 1.338159 -18.660039 17.858530
C 1.126317 -20.760878 18.297377
C -0.503200 -17.152400 22.083800
C -1.443386 -17.690439 20.996027
C -0.642435 -17.491338 19.712587
C -1.407450 -17.531496 18.386222
C 2.738700 -20.841500 11.922100
C 2.337403 -20.250883 13.350040
C 0.862083 -19.916010 13.864665
C -9.224800 -20.272800 17.990800
C -7.944700 -20.731700 17.248400
C -7.344201 -19.519516 16.533393
C -5.834773 -19.495387 16.533322
C -2.810600 -25.434000 15.589000
C -3.280600 -25.318400 14.145300
C -1.836081 -24.376802 16.257631
C -2.076683 -22.813099 15.995265
C -5.175200 -25.312100 12.592600
C -5.868500 -23.952400 12.417500
C -5.072742 -21.602095 11.767795
C -4.257656 -20.708679 12.598903
C -6.340700 -21.076000 11.172900
C -4.821300 -11.380300 13.736100
C -3.300800 -12.752300 12.339900
C -2.853478 -14.280257 12.330339
C -2.866951 -15.176831 13.666227
O 1.066500 -19.380800 21.455100
O -2.446676 -18.245261 18.377123
O -0.879393 -16.650735 17.690734
O 0.111121 -19.301601 13.004500

O 0.714638 -20.155720 15.122711
O -5.163869 -20.328720 15.837683
O -5.358842 -18.474685 17.128253
O -2.473100 -25.124500 13.231700
O -3.144166 -22.306205 15.590825
O -1.202662 -21.931866 16.231647
O -6.961400 -23.886800 11.855900
O -3.671851 -19.696683 12.140981
O -4.172706 -21.128739 13.778812
O -3.923000 -10.902300 14.389400
O -1.892589 -16.101096 14.067973
O -4.035860 -15.254546 14.392183
O -1.750848 -20.230762 14.734561
O -1.814109 -17.922789 15.354803
O -3.169582 -16.367088 16.591187
O -2.625701 -19.868121 16.861330
O -3.921932 -18.493636 15.092536
O 0.326060 -16.599205 15.362206
O -1.420285 -14.391893 16.272183
O -1.023400 -18.269800 11.048000
N -3.458200 -19.471000 9.442700
N -2.537500 -21.680000 21.259100
N -2.578440 -21.934487 19.112982
C -3.413800 -22.711900 21.006000
C -3.556800 -22.768200 19.655300
C -2.138841 -21.163680 20.092631
N -8.707300 -17.426600 13.456500
N -6.853300 -17.617000 12.159100
N -6.691983 -16.467989 14.131917
C -7.422500 -17.184100 13.265200
C 4.279300 -15.927400 15.113500
C 3.197394 -16.981364 14.985514
C 4.349000 -15.406200 16.534600
C -5.547100 -13.649400 20.704200
C -4.054800 -13.641700 20.060700
O -3.638105 -13.769411 18.723034
O -3.078800 -13.348800 20.965900
C -5.186600 -18.182300 21.927700
C 0.063100 -23.861300 20.130600
O 3.226000 -22.577700 19.641300
O -8.486100 -15.233100 15.410500

Authored and co-authored publications

The author of this thesis contributed to the following articles:

Peer-reviewed articles

- Grundmeier, A. and Dau, H. (2012). Structural models of the manganese complex of photosystem II and mechanistic implications. *Biochim. Biophys. Acta*, 1817(1):88–105
- Voevodskaya, N., Lenzian, F., Sanganas, O., Grundmeier, A., Gräslund, A., and Haumann, M. (2009). Redox intermediates of the Mn-Fe Site in subunit R2 of Chlamydia trachomatis ribonucleotide reductase: an X-ray absorption and EPR study. *J. Biol. Chem.*, 284(7):4555–4566
- Dau, H., Grundmeier, A., Loja, P., and Haumann, M. (2008). On the structure of the manganese complex of photosystem II: extended-range EXAFS data and specific atomic-resolution models for four S-states. *Philos. Trans. R. Soc. London, Ser. B*, 363(1494):1237–1243
- Haumann, M., Grundmeier, A., Zaharieva, I., and Dau, H. (2008). Photosynthetic water oxidation at elevated dioxygen partial pressure monitored by time-resolved X-ray absorption measurements. *Proc. Natl. Acad. Sci. U. S. A.*, 105(45):17384–17389
- Barra, M., Haumann, M., Loja, P., Krivanek, R., Grundmeier, A., and Dau, H. (2006). Intermediates in assembly by photoactivation after thermally accelerated disassembly of the manganese complex of photosynthetic water oxidation. *Biochemistry*, 45(48):14523–14532
- Haumann, M., Barra, M., Loja, P., Löscher, S., Krivanek, R., Grundmeier, A., Andreasson, L. E., and Dau, H. (2006). Bromide does not bind to the Mn₄Ca complex in its S₁ state in Cl⁻-depleted and Br⁻-reconstituted oxygen-evolving photosystem II: evidence from X-ray absorption spectroscopy at the Br K-edge. *Biochemistry*, 45(43):13101–13107

Other articles

- Grundmeier, A., Loja, P., Haumann, M., and Dau, H. (2008a). The manganese complex of photosystem II: Extended-range EXAFS data and specific structural models for four S-states. In *Photosynthesis. Energy from the Sun*, volume 4, pages 405–408. Springer, Berlin/Heidelberg, Germany
- Grundmeier, A., Risch, M., Sanganas, O., Gerencsér, L., Löscher, S., Zaharieva, I., Chernev, P., Pfirrmann, S., Limberg, C., Marinos, N., Driess, M., Hörnke, M., Koksich, B., Kraehmer, V., Rehder, D., Anderlund, M., Magnuson, A., Haumann, M., and Dau, H. (2008b). Synthetic models of biological metal centers studied by X-ray absorption spectroscopy at V, Mn, Fe, Ni, and Zn K-edges. *BESSY Annual Report 2008*, pages 403–404
- Risch, M., Khare, V., Grundmeier, A., Sanganas, O., Gerencsér, L., Zaharieva, I., Löscher, S., Chernev, P., Haumann, M., and Dau, H. (2008). Characterization of a novel water-oxidizing cobalt catalyst by X-ray absorption spectroscopy. *BESSY Annual Report 2008*, pages 68–69
- Sanganas, O., Grundmeier, A., Risch, M., Zaharieva, I., Chernev, P., Khare, V., Weyhermüller, T., Wieghardt, K., Voevodskaya, N., Gräslund, A., Stripp, S., Happe, T., Dau, H., and Haumann, M. (2008). X-ray absorption spectroscopy investigations on binuclear metal sites in proteins and models at the Mn and Fe K-edges. *BESSY Annual Report 2008*, pages 405–406
- Grundmeier, A., Repen, B., Süß, B., Tietz, T., Limberg, C., Anderlund, M., Magnuson, A., Haumann, M., and Dau, H. (2006). Photosynthetic water oxidation: The protein-bound manganese complex of photosystem II and biomimetic models studied by XAS at the Mn K-edge. *BESSY Annual Report 2006*, pages 282–284

Abstract

The manganese complex (Mn complex) bound to the protein complex photosystem II (PSII) is responsible for water oxidation and O₂ formation in photosynthesis. Due to its important role, the structure of the Mn complex is of very high interest.

In this thesis, extended-range EXAFS spectra measured for PSII membrane particles are presented which allow for significantly higher distance resolution in contrast to standard EXAFS at the Mn-edge.

Further, recently in literature published models of the Mn complex are discussed in regard to these data as well as in literature published EXAFS spectra and XRD results. The EXAFS data from literature taken into account were measured

- (i) on partially oriented PSII membrane particles under different angles between the electric-field vector of the X-ray beam and the sample normal and
- (ii) on PSII crystals for all three axes of the unit cell.

For the structural models, EXAFS spectra are calculated and compared to these experimental results.

Based on the experimental EXAFS data and starting from an XRD structure of PSII, for the first time models of the Mn complex are developed which are in agreement with EXAFS measurements on both partially oriented PSII samples and PSII crystals.

Kurzfassung

Der Mangankomplex des Photosystem II (PSII) ist in der Photosynthese verantwortlich für die Oxidation von Wasser und Bildung von molekularem Sauerstoff. Auf Grund dieser wichtigen Funktion ist die Aufklärung der Struktur des Mangankomplexes von herausragender Bedeutung.

In dieser Arbeit werden sogenannte „Extended-range“-EXAFS-Spektren von PSII-Membranpartikeln präsentiert. Diese Daten ermöglichen im Vergleich zu Standard-EXAFS-Spektren an der Mn-Kante eine deutliche höhere Distanzauflösung.

Des Weiteren werden einige in den letzten Jahren in der Literatur veröffentlichte Modelle des Mangankomplexes im Hinblick auf diese Daten als auch weiterer in der Literatur veröffentlichter EXAFS-Spektren analysiert. Hierzu wurden EXAFS-Spektren aus der Literatur verwendet, die

- (i) an partiell-orientierten PSII-Membranpartikeln unter verschiedenen Winkeln zwischen dem Vektor des elektrischen Feldes des Röntgenstrahls und der Probennormalen sowie
- (ii) an PSII-Kristallen für alle drei Achsen der Einheitszelle

gemessen wurden. Für alle betrachteten Modelle wurden EXAFS-Spektren simuliert und mit diesen experimentellen Resultaten verglichen.

Basierend auf den experimentellen EXAFS-Daten und ausgehend von Ergebnissen der Röntgenstrukturanalyse des PSII werden erstmalig Modelle des Mangankomplexes entwickelt, die in Übereinstimmung mit den EXAFS-Messungen sowohl an partiell orientierten PSII-Proben als auch PSII-Kristallen sind.

Danksagung

An erster Stelle möchte ich mich bei Herrn Prof. Dr. Holger Dau für die intensive Betreuung bedanken. Er hat es mir ermöglicht, auf den spannenden Gebieten der Biophysik und Röntgenabsorptionsspektroskopie zu arbeiten. Durch seine freundliche Unterstützung und jederzeitige Hilfe wurde diese Arbeit erst möglich.

Herrn Prof. Dr. Wolfgang Kuch möchte ich mich dafür danken, dass er sich als Zweitgutachter zur Verfügung stellt. Des Weiteren danke ich Herrn Prof. Dr. Felix von Oppen für die Übernahme des Vorsitzes der Promotionskommission sowie Dr. Ivelina Zaharieva und Kathrin Lange, dass sie sich als Mitglieder der Promotionskommission zur Verfügung gestellt haben.

Herrn Dr. Michael Haumann gilt mein Dank für die kompetente Hilfe bei den Synchrotronmessungen und auch dafür, dass er mir ermöglicht hat, mich an weiteren Projekten zu beteiligen und somit mein (bio-)physikalisches Wissen zu verbreitern.

Ich bedanke mich des Weiteren bei Dr. Peter Liebisch und Dr. Claudia Müller für die Einweisungen in die theoretischen bzw. praktischen Aspekte der Forschung am Photosystem II während meiner Anfangszeit in der Arbeitsgruppe.

Paola Loja gehört mein herzlicher Dank für ihre geduldige Einführung in das Gebiet der Röntgenspektroskopie. Für die gemeinsam durchgeführten Extended-Range-EXAFS-Messungen inklusive der Datenauswertungen bin ich ihr zu großem Dank verpflichtet. Des Weiteren möchte ich mich auch bei Dr. Ivelina Zaharieva, Dr. László Gerencsér und Oliver Sanganas für ihre Beteiligung und Hilfe bei weiteren Extended-Range-EXAFS-Messungen bedanken. Monika Fünning war für die wie immer ausgezeichneten PSII-Proben zuständig. Hierfür und für die angenehme Zusammenarbeit im Rahmen der Probenpräparationen gilt auch ihr mein Dank.

Bei André Klauß, Björn Süß und Joachim Buchta möchte ich mich für die angenehme gemeinsame Zeit in unserem Büro bedanken. Auch Oliver Sanganas, Paola Loja und Dr. Marcos Barra gilt mein Dank für angenehme miteinander verbrachte Jahre im alten Zimmer. Dr. Simone Löscher danke ich für die gemeinsame Bürozeit zur Beginn der Promotion, aber auch für fachliche Unterstützung und die gemeinsamen Synchrotronruns. Bei Marion Bardow bedanke ich mich für ihre immer freundliche Hilfe in diversen Angelegenheiten.

Mein besonderer Dank gilt schließlich noch einmal Dr. Ivelina Zaharieva, Marcel Risch, André Klauß, Joachim Buchta und natürlich auch Herrn Prof. Dr. Holger Dau für intensives Korrekturlesen und dass sie mir in der Schlussphase dieser Arbeit mit Rat und Tat zur Seite gestanden haben.

Danksagung

Allen jetzigen und ehemaligen Mitgliedern der Arbeitsgruppe Dau gilt mein herzlicher Dank für die angenehme Arbeitsatmosphäre. Es war eine tolle Zeit!

Herrn Prof. Dr. Robert Bittl und seiner Arbeitsgruppe danke ich dafür, dass sie mir EPR-Messungen an PSII-Proben ermöglicht haben. Insbesondere bedanke ich mich in diesem Zusammenhang bei Susanne Pudollek für die kompetente fachliche Unterstützung.

Herrn Dr. Wolfram Meyer-Klaucke danke ich für die Hilfe bei der Durchführung der EXAFS-Messungen am DESY.

Schließlich möchte ich mich bei meinen Eltern und meinem Bruder Philipp dafür bedanken, dass sie mich während der gesamten Promotionszeit unterstützt und, falls notwendig, aufgemuntert haben. Ohne sie hätte ich diese Arbeit nicht abschließen können.

Hiermit versichere ich, die vorliegende Dissertation eigenständig und ausschließlich unter Verwendung der angegebenen Hilfsmittel angefertigt zu haben. Die vorliegende Arbeit ist in dieser oder ähnlicher Form nicht schon einmal in einem Promotionsverfahren angenommen oder als ungenügend begutachtet worden.

Berlin, 30.09.2011